

Copyright is owned by the Author of the thesis. Permission is given for a copy to be downloaded by an individual for the purpose of research and private study only. The thesis may not be reproduced elsewhere without the permission of the Author.

Edge Functionalisation of Graphene Nanoribbons with a Boron Dipyrin Complex

A thesis presented in partial fulfilment of the requirements for the
degree of

Doctor of Philosophy

in

Nanoscience

at Massey University, Manawatū,

New Zealand.

Ashley Jacquelyne Way

2017

Abstract

Chemical modification can be used to tune the properties of graphene and graphene nanoribbons, making them promising candidates for carbon-based electronics. The control of edge chemistry provides a route to controlling the properties of graphene nanoribbons, and their self-assembly into larger structures. Mechanically fractured graphene nanoribbons are assumed to contain oxygen functionalities, which enable chemical modification at the nanoribbon edge.

The development of graphene nanoribbon edge chemistry is difficult using traditional techniques due to limitations on the characterisation of graphene materials. Through the use of a chromophore with well-defined chemistry, the reactivity of the edges has been investigated. Small aromatic systems were used to understand the reactivity of the boron dipyrin Cl-BODIPY, and with the aid of spectroscopic and computational methods, the substitution mechanism and properties of the compounds have been investigated.

The synthetic procedure was then applied to graphene nanoribbons. Results from infrared and Raman spectroscopy studies show that edge-functionalisation of graphene nanoribbons with BODIPY was successful, and no modifications to the basal plane have been observed.

Contributions

All work presented in this thesis was completed by Ashley Way

Except:

- All infrared spectroscopy data was acquired by Ewan Fisher
- NMR spectra utilising the 700 MHz NMR spectrometer were performed by Dr. Pat Edwards
- Mass Spectrometry measurements were performed by David Lun
- Emission lifetime calculations were performed by Geoffry Laufersky at Victoria University, Wellington, using data acquired by Ashley Way
- Raman spectra background removal was performed by Josiah Cleland
- X-ray crystallographic data was acquired by Prof. Shane Telfer and David Perl

Acknowledgements

I would like to thank my supervisor Associate Professor Mark Waterland for his guidance throughout this PhD. Thank you for your guidance on computational methods and assistance with Raman measurements.

I also thank my co-supervisors Professors Shane Telfer and Simon Hall for their assistance when needed. I would like to acknowledge Joran Taylor for her assistance and expertise in the microtomy techniques used to prepare the graphene nanoribbons used in this work. I also thank David Lun for his assistance and guidance in the lab, and Dr. Pat Edwards for his assistance with NMR measurements.

I thank Ewan Fisher for acquiring IR spectra, Josiah Cleland for assistance with Raman spectra background removal, and the rest of the Waterland research group for discussions of Raman and optimisation of techniques.

I thank Geoffry Laufersky for calculations of lifetimes from time resolved emission measurements performed at Victoria University, Wellington.

I would like to acknowledge the financial support from Massey University for a Doctoral scholarship, and the Institute of Fundamental Sciences for additional funding. I also thank the New Zealand Institute of Chemistry for assisting with conference funding throughout my studies.

Finally, I thank my family and friends, for their encouragement and support throughout my studies, especially the last 3 and a half years.

Contents

Abstract.....	i
Contributions.....	ii
Acknowledgements.....	iii
Figures.....	ix
Tables.....	xiv
Abbreviations.....	xv
Chapter 1. Introduction.....	1
1.1 Materials.....	2
1.1.1 Graphene.....	2
1.1.2 The chemistry of graphene.....	5
1.1.3 Graphene nanoribbons.....	6
1.1.4 Light-harvesting molecules.....	8
1.1.5 Potential applications.....	10
1.2 Characterisation of Materials.....	10
1.2.1 Raman spectroscopy of graphitic materials.....	10
1.2.2 Infrared spectroscopy of graphene.....	13
1.2.3 Computational studies of graphitic compounds.....	14
1.3 Theory of interaction between dipyrin and graphene.....	14
1.4 Stability of aromatic compounds.....	19

Chapter 2. Synthetic methods.....	23
2.1 Synthesis of dipyrin compounds.....	23
2.1.1 Thioketone dipyrin	23
2.1.2 Ketone dipyrin	24
2.1.3 Cl-BODIPY.....	24
2.2 Functionalisation of small-analogue compounds.....	25
2.2.1 Phenol/BODIPY	25
2.2.2 MeO/BODIPY.....	26
2.2.3 Aniline/BODIPY	27
2.2.4 1-naphthylamine/BODIPY.....	29
2.2.5 2-naphthylamine/BODIPY.....	30
2.2.6 1-naphthol/2xBODIPY	31
2.2.7 2-naphthol/BODIPY	32
2.2.8 2-naphthol/2xBODIPY	33
2.2.9 1-aminoanthracene/BODIPY.....	34
2.2.10 2-aminoanthracene/BODIPY.....	34
2.2.11 9-aminophenanthrene/BODIPY.....	35
2.2.12 9-hydroxyphenanthrene/BODIPY.....	35
2.2.13 2-hydroxytriphenylene/BODIPY.....	36
2.2.14 1-hydroxypyrene/BODIPY	37
2.2.15 HBC(t-Bu) ₅ OH/BODIPY	38

2.2.16	HPB(t-Bu)5OH/BODIPY	39
2.2.17	Benzoic acid/BODIPY	40
2.3	Functionalisation of graphene nanoribbons	40
2.3.1	Calculation of nanoribbon quantity	40
2.3.2	General reaction for BODIPY-functionalisation of graphene nanoribbons	42
2.3.3	Purification of BODIPY-functionalised graphene nanoribbons	43
2.4	Crystallography	43
2.4.1	1-naphthylamine/BODIPY	45
2.4.2	1-naphthol/2xBODIPY	45
2.4.3	2-naphthol/2xBODIPY	46
Chapter 3.	Computational studies of graphene nanoribbons	47
3.1	Graphene analogue computational studies	48
3.1.1	Description of analogues	49
3.1.2	Results and discussion	55
3.1.3	Analysis of models	58
3.2	Graphene nanoribbon studies	60
3.2.1	Graphene nanoribbon structures	60
3.2.2	Discussion of results	61
3.3	Functionalisation studies	64

3.4	Reaction mechanism study	70
3.4.1	Calculation of pKa values	72
3.4.2	Thermodynamics.....	76
Chapter 4.	Spectroscopy of dipyrins	87
4.1	Quantitative absorption studies.....	88
4.1.1	TD-DFT studies of excitations	90
4.1.2	Solvent dependent excitations	91
4.1.3	Effect of double-substitution on spectra	96
4.1.4	Exciton coupling in multi-chromophore systems.....	101
4.2	Quantitative emission studies.....	104
4.2.1	Determination of Quantum Yields	104
4.2.2	3-Dimensional emission plots	107
4.3	Time-resolved emission	110
4.4	Infrared spectroscopy	116
4.5	Raman spectroscopy.....	124
Chapter 5.	Dipyrin-functionalised graphene nanoribbons	127
5.1	Infrared spectroscopy	129
5.2	Raman spectroscopy.....	131

Chapter 6. Summary and Perspectives.....	135
Bibliography.....	139
Appendices	147
Appendix A: NMR Spectra.....	147
Appendix B: Conversion of Raman spectra units	164

Figures

Figure 1.1 - Graphene sheet.....	2
Figure 1.2 - Number of publications with title containing keywords “graphene” (grey) and “nanoribbon” (gold) since 2004	3
Figure 1.3 - Number of graphene publications by field: chemistry (blue) and physics (purple).....	4
Figure 1.4 - Demonstration of zig-zag (blue) and armchair (orange) edges of graphene	4
Figure 1.5 - Potential edge structure combinations of graphene nanostructures (orange: armchair; blue: zig-zag)	6
Figure 1.6 - a) Accumulation of graphene nanoblocks during mechanical fracturing; b) Transfer of graphene nanoblocks	7
Figure 1.7 - Nucleophilic displacement in meso-halogenated BODIPY dyes	9
Figure 1.8 - Raman modes of graphene	11
Figure 1.9 - Jablonski diagram showing photophysical processes.....	15
Figure 1.10 - Illustration of Franck-Condon factors for large and small vibrational mode displacements	16
Figure 1.11 - Franck-Condon principle for a radiative transition (absorption)	18
Figure 1.12 - Kekulé (a) and Clar (b) representations of naphthalene	20
Figure 1.13 - Clar structures of: a) anthracene; and b) phenanthrene.....	21
Figure 2.1 - GNR edge "unit cell".....	42
Figure 2.2 – Crystal structure of 1-naphthylamine/BODIPY.....	45
Figure 2.3 – Crystal structure of 1-naphthol/2xBODIPY	45
Figure 2.4 – Crystal structure of 2-naphthol/2xBODIPY	46

Figure 3.1 - Comparison between PBE and B3LYP functionals for frequency calculation for the transition state structure of phenol/BODIPY.....	48
Figure 3.2 - Zig-zag edged structures: a) anthracene; b) pentacene; c) heptacene; and d) nonacene	49
Figure 3.3 - Armchair edged structures: a) phenanthrene; b) picene; c) dibenzopicene; and d) dinaphthopicene.....	50
Figure 3.4 - Ring structures: a) pyrene; b) coronene; c) ovalene; d) hexa-peri-benzocoronene; and e) TBDBPP-ovalene	51
Figure 3.5 - Calculated Raman spectra of zig-zag structures	52
Figure 3.6 - Calculated Raman spectra of armchair structures.....	53
Figure 3.7 - Calculated Raman spectra of ring structures	54
Figure 3.8 - Relative D mode intensity in calculated zig-zag Raman spectra	55
Figure 3.9 - Relative R mode intensity in calculated armchair Raman spectra	56
Figure 3.10 - Vibrational modes of ovalene (left) and hexa-peri-benzocoronene (right).....	59
Figure 3.11 - Comparison of Raman bond parameters for graphene fragments using Hückel and DFT methods; good agreement is observed between low and high levels of theory	60
Figure 3.12 - Skeletal structures of a) armchair and b) zig-zag edged nanoribbon analogues.....	61
Figure 3.13 - Calculated IR spectra for armchair and zig-zag nanoribbon analogues (individual points plotted)	62
Figure 3.14 - Calculated IR spectra for armchair and zig-zag nanoribbon analogues (artificially widened)	63
Figure 3.15 - Calculated and experimental IR spectra for graphene nanoribbons .	63

Figure 3.16 - Crystal structures for basis set optimisation; left: 1-naphthylamine/BODIPY; right: 2-naphthol/2xBODIPY	65
Figure 3.17 - Optimised geometries of 1-naphthylamine/BODIPY	67
Figure 3.18 - Optimised geometries of 2-naphthol/2xBODIPY	69
Figure 3.22 - Molecular orbital diagrams for 1-naphthylamine (left) and 2-naphthylamine (right)	78
Figure 3.23 - Density of states for 2-naphthol with overlaid molecular orbitals	80
Figure 3.24 - Density of states for 2-naphthylamine with overlaid molecular orbitals	80
Figure 3.25 - HOMO for -O-BODIPY compounds with HOMO-LUMO gap stated	82
Figure 3.26 - LUMO for -O-BODIPY compounds	83
Figure 4.1 - Solvatochromism of Cl-BODIPY	87
Figure 4.2 - Beer-Lambert plot for 2-aminoanthracene/BODIPY in toluene	88
Figure 4.3 - Normalised absorption spectra of 1-naphthol/2xBODIPY	92
Figure 4.4 - TD-DFT excitation spectra of 1-naphthol/2xBODIPY; Modes with oscillator strength > 0.1 have been assigned to molecular orbital transitions..	94
Figure 4.5 - Occupied orbitals: 1-naphthol/2xBODIPY	95
Figure 4.6 - Virtual orbitals: 1-naphthol/2xBODIPY	95
Figure 4.7 - Absorption spectra of 2-naphthol/1x and 2xBODIPY	98
Figure 4.8 - TD-DFT excitation spectra of 2-naphthol/1x and 2xBODIPY; Modes with oscillator strength > 0.1 have been assigned to molecular orbital transitions..	98
Figure 4.9 - Occupied (blue and red) and virtual (orange and teal) orbitals: 2-naphthol/1xBODIPY	99
Figure 4.10- Occupied (blue and red) and virtual (orange and teal) orbitals: 2-naphthol/2xBODIPY	99

Figure 4.11 - Absorption spectra of 2-naphthol/2xBODIPY in acetonitrile at different concentrations.....	100
Figure 4.12 - Transition dipole for BODIPY	101
Figure 4.13 - Geometrical parameters used to define the orientation of two transition dipole moments	102
Figure 4.14 - Determination of geometrical parameters for 1-naphthol/2xBODIPY (top) and 2-naphthol/2xBODIPY (bottom) with α and α' (left) and β (right). BODIPY planes (long axis = dipole) are shown for clarity	103
Figure 4.15 - E_T^N scale for selected solvents	107
Figure 4.16 - 3D (left) and contour (right) plots of Cl-BODIPY in: ethyl acetate (top); acetonitrile (centre); and toluene (bottom)	108
Figure 4.17 - 3D (left) and contour (right) plots of Cl-BODIPY in: chloroform (top); chlorobenzene (centre); and isopropyl alcohol (bottom).....	109
Figure 4.18 - Excitation data for Cl-BODIPY in three solvents; Data for $\lambda_{ex} = 500$ nm has been scaled to match λ_{em} at approximately 525 nm.....	111
Figure 4.19 - $\ln k_{nr}$ vs E_{em} for all compounds	114
Figure 4.20 - $\ln k_{nr}$ vs E_{em} for hydroxyl containing compounds; Data has been separated between mono- (1x) and d- (2x) substituted analogues	115
Figure 4.21 - Comparison between calculated and experimental IR spectra of 1-hydroxypyrene.....	117
Figure 4.22 - Comparison between calculated and experimental IR spectra of 1-hydroxypyrene/BODIPY.....	117
Figure 4.23 - Experimental IR spectra of 1-hydroxypyrene and 1-hydroxypyrene/BODIPY.....	119

Figure 4.24 - Calculated IR spectra of 1-hydroxypyrene and 1-hydroxypyrene/BODIPY.....	119
Figure 4.25 - Calculated IR spectra of HBC(t-Bu)5OH and HBC(t-Bu)5OH/BODIPY.....	120
Figure 4.26 - Vibrational modes - BODIPY functionalisation;.....	121
Figure 4.27 - Calculated IR spectrum for 1-hydroxypyrene/BODIPY with assigned vibrational modes.....	123
Figure 4.28 - Calculated IR spectrum for HBC(t-Bu)5OH/BODIPY with assigned vibrational modes.....	124

Tables

Table 2.1 - Crystallography data	44
Table 3.1 - Bonding energies for 1-naphthylamine	67
Table 3.2 - Bonding energies for 2-naphthol/2xBODIPY	68
Table 3.3 - Comparison of experimental and calculated pKa values	73
Table 3.4 - Comparison of experimental and calculated pKa values in water	75
Table 3.5 - Comparison of experimental and calculated pKa values in dichloroethane	75
Table 3.6 - Calculated pKa values for analogues.....	75
Table 3.7 - Thermodynamic information for functionalisation studies.....	77
Table 4.1 – Summary of molar absorptivity coefficients ($\text{mol}^{-1}\text{Lcm}^{-1}$) for Cl-BODIPY and its small-analogue products. Standard errors (rounded to 1 significant figure) are included in brackets	90
Table 4.2 - Geometrical parameters for exciton coupling.....	104
Table 4.3 - Relative quantum yields. * indicates reference standard used is Coumarin 6H; all others calculated with Coumarin 334 as standard	106
Table 4.4 - Lifetimes in ethyl acetate.....	112
Table 4.5 - Lifetimes in acetonitrile	112
Table 4.6 - Lifetimes in toluene	112

Abbreviations

General

GNR	Graphene nanoribbon
HOPG	Highly-oriented pyrolytic graphite
kT	Energy equal to 4.11×10^{-21} J at 298 K

Molecular orbitals

HOMO	Highest occupied molecular orbital
LUMO	Lowest unoccupied molecular orbital

Computational terms

STO	Slater-type orbital	
GTO	Gaussian-type orbital	
B3LYP	Becke, 3-parameter, Lee-Yang-Parr	(functional)
PBE	Perdew-Burke-Ernzerhof	(functional)
MO6	Minnesota-06	(functional)
MO6-2X	Minnesota-06, Hartree-Fock exchange	(functional)
DZP	Double-zeta, 1 polarisation (STO)	(basis set)

Notation for computational terms

(functional)/(basis set) Example: B3LYP/DZP

Notation for analogue compounds

analogue/BODIPY

Example: phenol/BODIPY

Solvents

DCM

Dichloromethane

IPA

Isopropyl alcohol / propan-2-ol

DCE

1,2-dichloroethane

EtOAc

Ethyl acetate

MeCN

Acetonitrile

Chapter 1. Introduction

Graphene is a material of great interest for many applications including electronic devices due to its chemical and physical stability and excellent electronic transport properties. Chemical modifications can be utilised to tune graphene properties towards desired applications. Modifications to the basal plane of graphene introduces defects to the graphene lattice, whilst edge-modifications maintain the lattice structure, and add bulk to the edges of graphene.

Graphene nanoribbons are long, thin graphene structures which exhibit different chemical, electronic, and optical properties dependent on their edge structures and widths.¹⁻³ Production of nanoribbons with controllable size and edge structure is advantageous for potential applications. Typical nanoribbon production techniques produce ribbons which have a degree of oxidation to both the edges and basal plane.⁴⁻⁵ Mechanical fracturing enables the production of batches of nanoribbons with consistent edge structure whilst avoiding chemical process which may induce oxidation.⁶ This allows spectroscopic studies to be performed to determine the edge structures. Computational chemical studies performed on small ribbon-like fragments provide a method to determine edge structure and edge termination through comparison with experimental data.

The edge-functionalisation of graphene nanoribbons with a well-understood chromophore is of use for further understanding graphene nanoribbons. By functionalising ribbons at the edges, the basal plane and properties of the graphene itself remain unaltered, whilst the addition of a chromophore allows the edge chemistry of the mechanically fractured ribbons to be probed.

Boron dipyrrens (BODIPYs) are a commonly utilised family of chromophores which have been functionalised with small aromatic structures. Through the expansion of literature methods to obtain a new group of BODIPY functionalised small molecule compounds, and the use of computational chemistry, the chemistry and spectroscopy of BODIPY can be further understood. The use of small molecule systems allows the utilisation of characterisation techniques not available for large structures such as graphene nanoribbons.

The expansion of synthetic methods to graphene nanoribbons allows for the production and characterisation of graphene nanoribbons functionalised at the edges with BODIPY.

1.1 Materials

1.1.1 Graphene

Graphene consists of a single layer of carbon atoms in a hexagonal arrangement, as shown in Figure 1.1. Graphene was first isolated in 2004⁷, and since this time a significant body of knowledge has been acquired on the material, in terms of both its properties, synthesis, and potential applications.^{1,8-14}

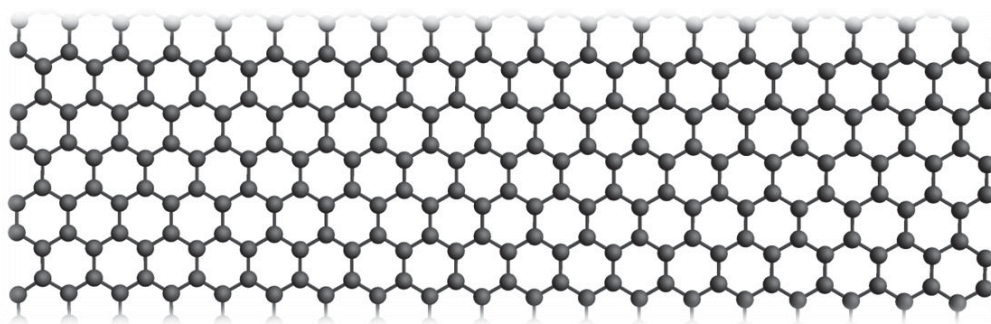


Figure 1.1 - Graphene sheet

Graphene has many properties which make it desirable, including its high thermal conductivity,¹⁵⁻¹⁶ and excellent electronic properties,^{1, 17-18} however, it is difficult to produce in both high quality and large quantities.^{10, 19-20}

The numbers of publications including graphene in the title have increased exponentially since 2004, as shown in Figure 1.2, with studies of graphene nanoribbons being a small proportion of these. Further analysing total publications by field, it can be seen from Figure 1.3 that although initially the larger proportion of studies involving graphene focussed on physics, there has been a larger interest in the chemistry of graphene in recent years.

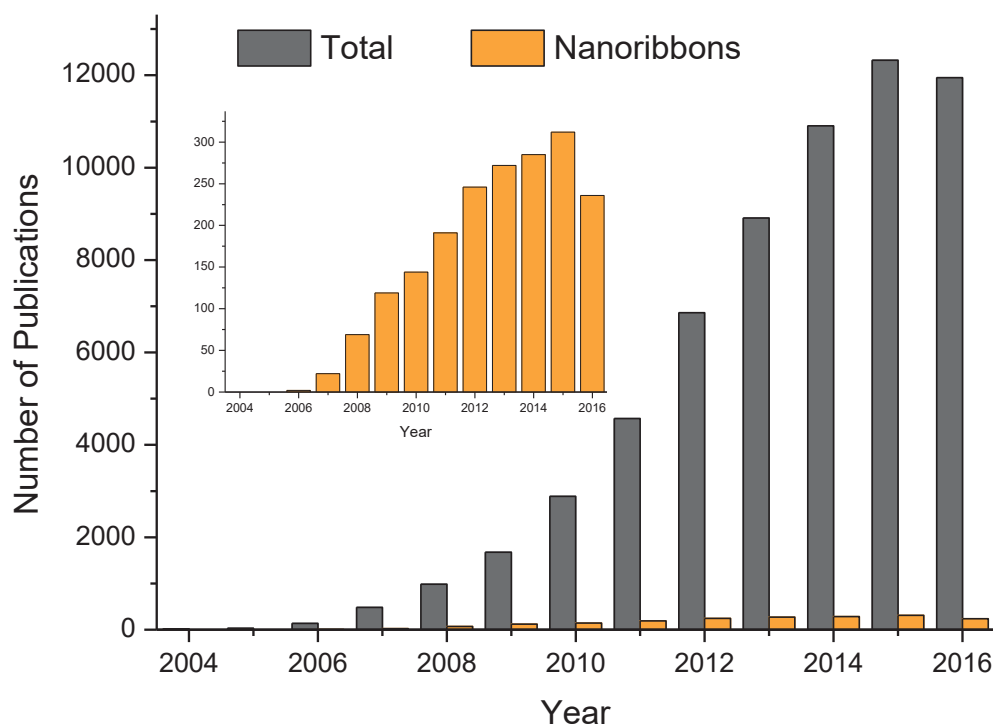


Figure 1.2 - Number of publications with title containing keywords “graphene” (grey) and “nanoribbon” (gold) since 2004 (source: Web of Science, 19/01/2017)

Functionalisation of graphene is performed on either the edge atoms or the basal plane, i.e. within the graphene plane. Basal plane functionalisation causes

disturbances in the electronic structure of graphene through distortion of the plane, whereas edge-functionalisation maintains the basal plane structure.

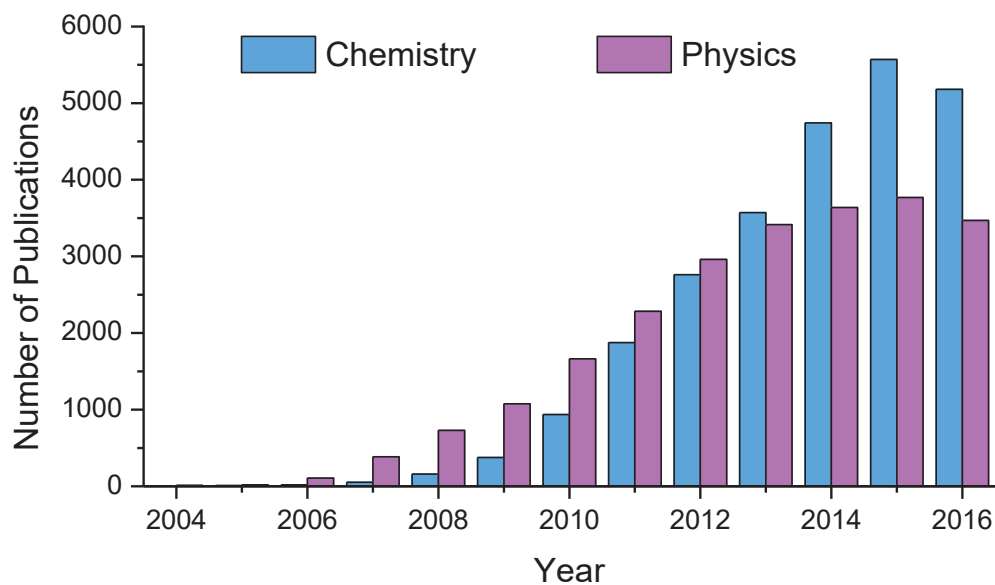


Figure 1.3 - Number of graphene publications by field: chemistry (blue) and physics (purple)
(source: Web of Science, 19/01/2017)

The edge-functionalisation of graphene is dependent on, and effected by, edge structure. The zig-zag and armchair directions of the edge structure, shown in Figure 1.4, are equivalent to x and y in a square lattice. The edge structure of graphene also effects properties and features in Raman spectra.

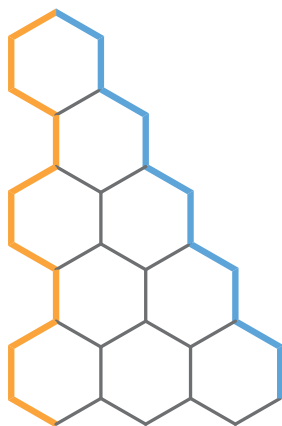


Figure 1.4 - Demonstration of zig-zag (blue) and armchair (orange) edges of graphene

The different Raman modes of graphene, and analysis of these, are described in more detail in 1.2.1.

Through calculation of density of states of graphene with specific edge structures, information can be obtained about the band structure and other properties. Kawasaki *et al*⁹ studied the density of states and spin density of graphene fragments, and found that spin polarisation occurred between opposite zig-zag edges of graphene, but not armchair edges, indicating a significant difference between zig-zag and armchair graphene edges.

1.1.2 The chemistry of graphene

The covalent functionalisation of graphene by chromophores shows promise in applications including nanoelectronics. Through the attachment of organic molecules, the extended aromatic structure of graphene is effected, enabling electronic properties to be controlled.²¹⁻²³ Functional groups can be introduced to graphene via edge or, more commonly, basal plane modification.²⁴⁻²⁶

Organic functionalisation is often performed through the formation of covalent bonds between either a free radical or dienophile and C=C bonds of graphene, or between organic functional groups and oxygen groups on graphene oxide.^{21, 27-29} A large number of free radicals and dienophiles have been utilised in such functionalisation, including diazonium salts,^{4, 30} nitrophenyls,²² benzoyl peroxide,³¹ azomethine ylide, and nitrenes. Covalent attachment to graphene oxide often involves the use of chromophores³²⁻³⁴ or polymers.^{27, 35-37} The functionalisation of graphene oxides with oligothiophene by Zhang *et al*³² showed strong interaction between graphene oxide and oligothiophene, with almost complete fluorescence quenching occurring in the functionalised compound compared with pure

oligothiophene. Additionally, covalent functionalisation has also been demonstrated to improve the dispersibility of graphene in organic solvents, as demonstrated by Zhang *et al*³³ with porphyrin functionalisation of graphene.

1.1.3 Graphene nanoribbons

Long and thin sheets of graphene are referred to as graphene nanoribbons (GNRs). These typically have widths of tens to a few hundred nanometers.⁵⁻⁶ Commonly used methods of producing graphene nanoribbons include chemical vapour deposition (CVD),³⁸ growth from solid carbon sources,³⁹ the opening, or unzipping, of carbon nanotubes,^{4, 40-43} electrochemical exfoliation,^{10, 20, 44-45} bottom-up synthesis via thermal polymerisation^{9, 46-47}, and mechanical fracturing.⁶ Each production method has advantages and disadvantages.

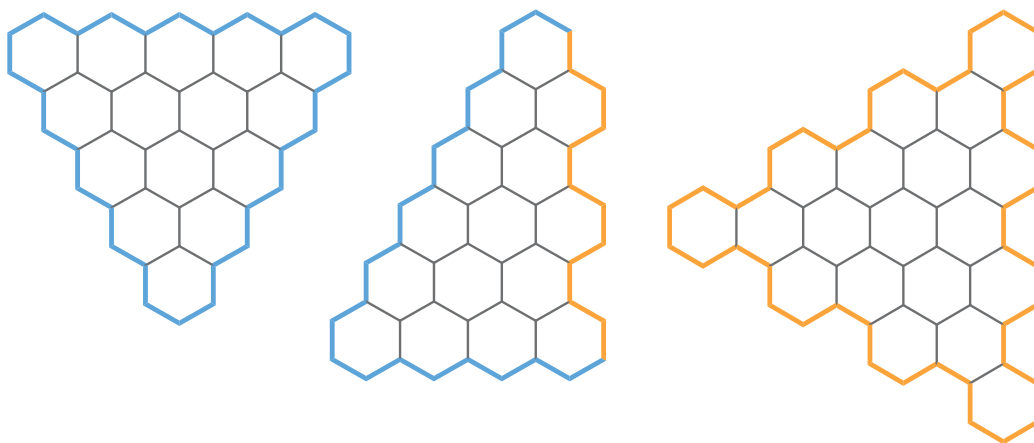


Figure 1.5 - Potential edge structure combinations of graphene nanostructures (orange: armchair; blue: zig-zag)

As with larger graphene sheets, the edge structure of the ribbon plays a significant role in the determination of the overall properties of the nanoribbon. Potential edge structure combinations for triangular graphene nanostructures are shown in Figure 1.5. These same edge-structure combinations are possible for

nanoribbons also. Purely armchair, purely zig-zag, and combination edged nanoribbons will all have different properties.

(a) Graphene nanoribbon production

Graphene nanoribbon production via mechanical fracturing provides the potential to have control over GNR edge structure.

In this method, adapted from that of Berry *et al*,⁶ a block of highly oriented pyrolytic graphene (HOPG) is mounted on a microtome using resin. A diamond knife is then used to cut the HOPG into nano-sized blocks, which gather like pencil shavings at the knife edge (Figure 1.6(a)). After many cuts, these long stacks are then transferred carefully (Figure 1.6(b)) to a vial containing desired solvent, and are exfoliated into graphene nanoribbons via sonication.

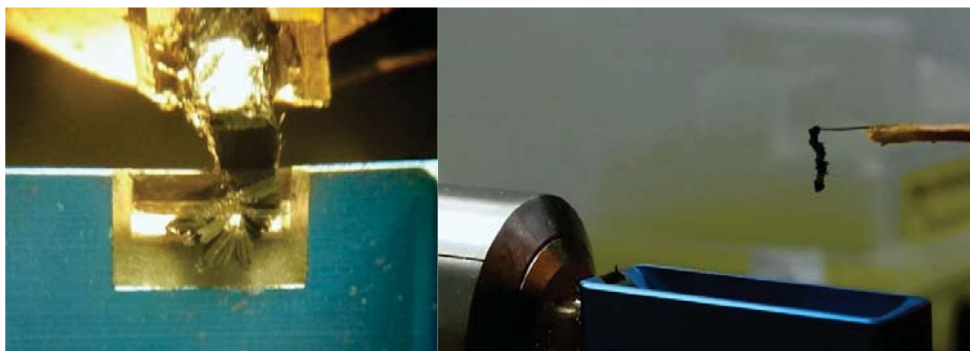


Figure 1.6 - a) Accumulation of graphene nanoblocks during mechanical fracturing; b) Transfer of graphene nanoblocks

An advantage of this method over more-typical synthetic methods is the chemical purity of the nanoribbons. By using only the HOPG and the solvent which subsequent modifications will be performed in, no chemical impurities are present in the exfoliated nanoribbon solutions.

1.1.4 Light-harvesting molecules

The production of functional, graphene-based solar cell materials requires a method which can be utilised to transfer charge carriers into the graphene. Photoresponsive, light-harvesting molecules, such as dipyrrens, show promise in this application.

Dipyrrens were first reported in 1937 by Fischer and Orth.⁴⁸ Since this time, dipyrrens have shown promise as efficient light-harvesting compounds for use in solar cells.⁴⁹⁻⁵⁰ Modified, dipyrren-BF₂ (BODIPY) complexes have excellent emission and fluorescence properties,⁵¹⁻⁵⁵ and have versatile chemical synthesis.^{52, 56-57}

(a) Previous studies of Meso-Substituted BODIPY analogues

Due to the prohibitive computational cost of performing ab initio quantum chemical calculations on graphene on nanometre length scales, small molecule analogues of graphene are used to model the interaction between dipyrren and graphene. To model interactions with functional groups on graphene edges, analogues involving -O- and -NH- bridges to carbon ring structures are of particular interest, with the -O- on ring structures being analogous to an oxidised graphene edge. The synthesis of such novel substituted BODIPY analogues has been reported using a limited number of methods.^{49, 55, 58-59} Although functionalisation of BODIPY is possible at different positions within the molecule, those functionalisations occurring at the *meso*, or 8-, position will be focussed on for this study. Whilst these compounds are referred to in various ways in literature, they will herein be referred to as *meso*-substituted BODIPY analogues.

Goud *et al*⁵⁸ reported the synthesis of such structures through the reaction of a thioketone with aniline and isopropyl triflate. Due to the mild nature of reaction

conditions, this method theoretically enables the introduction of a greater number of groups.

The group of Dehaen *et al*⁴⁹ reported a larger range of *meso*-substituted analogues. In their approach, *meso*-halogenated BODIPY dyes are synthesised. Substituted analogues are then obtained via nucleophilic displacement of halogen, as shown in Figure 1.7.

The syntheses are efficient, generally high yielding, and should be adaptable to nucleophiles with larger structures. More recent reports of substituted analogues by this group have utilised the same synthetic methods.⁵⁹

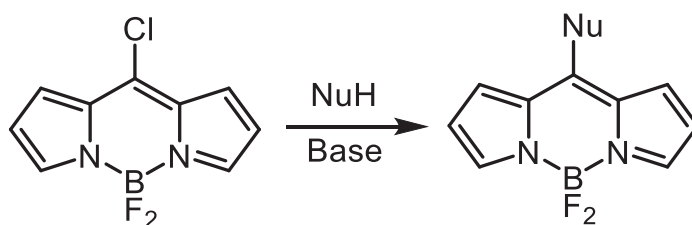


Figure 1.7 - Nucleophilic displacement in *meso*-halogenated BODIPY dyes (adapted from reference 49)

Peña-Cabrera *et al* reacted 8-methylthio-BODIPY with R-OH structures to form BODIPY-OR substituted compounds.⁵⁵ Their method differs from that of Dehaen *et al* by the conversion of thioketone dipyrryn to 8-methylthio BODIPY, as opposed to the conversion to 8-halogenated BODIPY. The differences in these methods lead to differing yields and reaction times, and also require different reaction conditions for the nucleophilic substitution step. Whilst the Dehaen method is performed at room temperature, the Peña-Cabrera method requires the reaction to be performed at 55°C.

(b) DFT studies of Meso-Substituted BODIPY analogues

Boens *et al*⁵⁹ reported quantum chemical calculations on substituted analogues. These calculations were performed, at the B3LYP/6-31G(d,p) level, to determine the effect of the *meso*-substituent on the optical properties of the compounds in terms of their frontier orbitals. Through changing the size of the substituent, whilst maintaining the same functional group it was found that the HOMO-LUMO gap was effected by changes in torsion and bonding/substitution angle. Similarly, when comparing substituents of similar size with different functional groups, it was found that while the HOMO is relatively unaltered by changing the functional group, the LUMO is very sensitive to *meso*-substitution. The changes observed for the change in HOMO-LUMO gap corresponded to observed shifts in absorption maxima. These findings agree with those observed by other groups.⁵⁴⁻⁵⁵

1.1.5 Potential applications

Functionalised graphene materials have shown potential for use in a wide range of applications, including photodetectors, sensors, nanoelectronics, biotechnology, semiconductors, memory devices, solar cells, and more.^{12, 21, 23, 60} The ability to selectively functionalise graphene allows control over structure, and provides methods to exploit the potential of graphene.

1.2 Characterisation of Materials

1.2.1 Raman spectroscopy of graphitic materials

Raman spectroscopy is a very useful tool for the determination of graphene structure.^{5, 61-68} Specific features in the Raman spectrum of any graphitic material allows for characterisation of the structure. As an example, the appearance of a

shear mode at approximately 40 cm^{-1} in a Raman spectrum indicates more than one graphitic layer is present.

(a) Raman modes of Graphene

The significant Raman modes of graphene are shown in Figure 1.8 and described in more detail in the following sections.

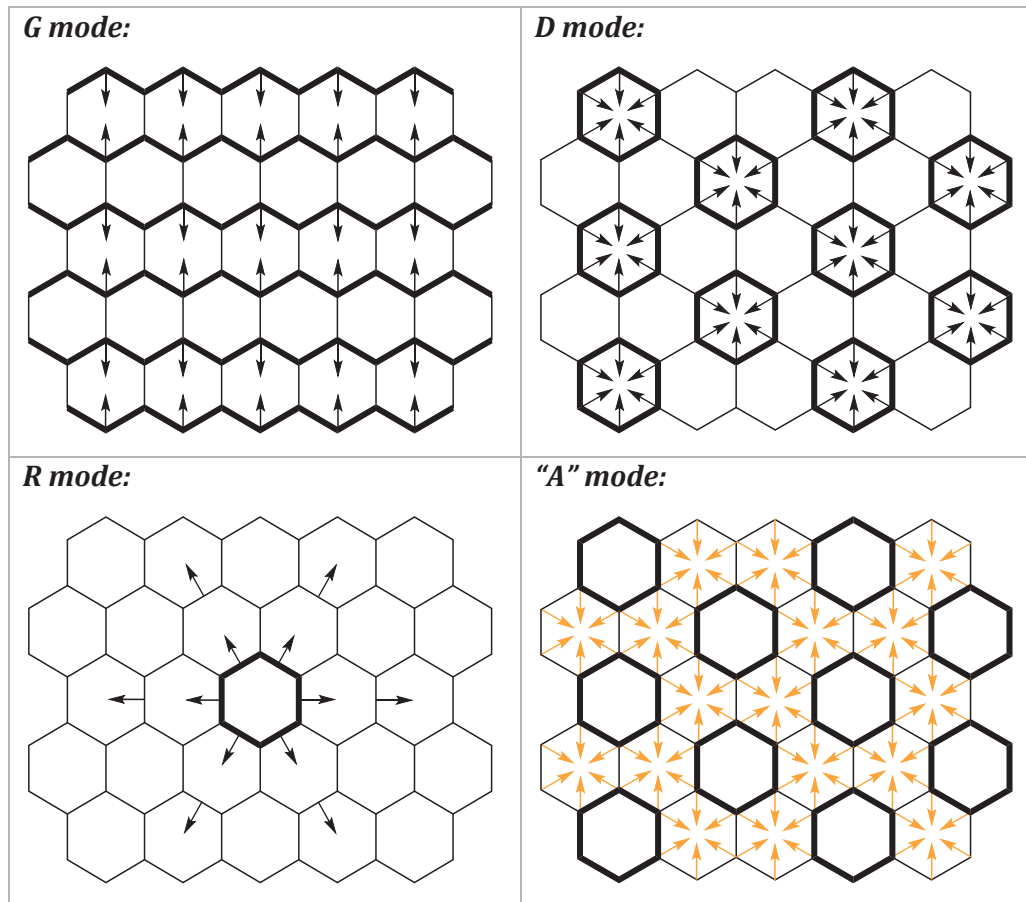


Figure 1.8 - Raman modes of graphene

(i) The G mode

The G mode is a doubly degenerate phonon mode which indicates the presence of sp^2 carbon networks. This mode is characterised by movement along the zig-zag edges in graphene. The position of the G mode can be effected by the induction of

extra charges due to functional groups at the edges.⁵ As such, this mode is a key factor in monitoring the functionalisation of graphene.

(ii) The D mode

The D mode is a disorder induced mode occurring around 1330 cm^{-1} .^{5, 69-70} The D mode is described by a stretching of ring bonds, as shown in Figure 1.8, where the bold lines indicate the stretching rings. D mode intensity decreases as zig-zag edge structure becomes more prominent in graphene, due to rings being unable to uniformly expand due to the bridging nature of the zig-zag edge. Because of this, the D mode can be used to determine the edge structure of graphitic materials.

(iii) The R mode

The R mode is a breathing mode, analogous to the radial breathing mode of carbon nanotubes, whereupon breathing occurs in the direction of the ring bonds (i.e. along the armchair direction).⁷¹ This is shown in Figure 1.8. It is of importance to note that this movement does not occur towards the atoms, or along the zig-zag direction, causing a difference between the Raman spectra of zig-zag and armchair edged structures.

(iv) The "A" mode

The mode that will herein be referred to as the "A" mode is a disorder induced mode very similar to the D mode, however, in this case, the rings which stretch are those that do not stretch in the D mode (refer to Figure 1.8). This mode appears in computationally calculated Raman spectra, and is generally in close proximity to the D mode. It is likely that in experimental spectra, the "A" mode is included in the D band intensity due to this close proximity.

(v) The G' mode

This is an overtone of the D band which is also disorder induced, due to two phonons, of opposite momentum, in the highest optical branch near **K**.⁶³ This peak changes in position with excitation energy due to a double resonance process, linking the phonon wave vectors to the electronic band structure.⁷²

(b) Analysis using Raman spectroscopy

The Raman scattering intensity ratio I_D/I_G is used to determine the defect quantity in graphitic materials.⁶² Whilst in bulk graphitic materials this ratio is used to determine the purity of the material, in graphene it gives an indication of the proportion of zig-zag and armchair structure.

As the number of layers of graphene increase, there is a shift in the position of the G' band (at approximately 2700 cm^{-1}).^{5,63,67} This can be useful when determining the number of layers in a material, however, a generally simpler method involves calculating the intensity ratio between the G' and G modes. In addition to this, the appearance of a shear mode at approximately 40 cm^{-1} indicates the presence of multiple graphitic layers.

1.2.2 Infrared spectroscopy of graphene

Pristine graphene has a near-featureless infrared absorption spectrum.³⁷ Changes to the structure of graphene, via adsorption or functionalisation, causes features to appear in infrared (IR) spectra.¹⁸ As with Raman spectra, graphene nanoribbons will have different IR spectra depending on their dimensions and edge-types. Functionalisation will also cause differences in the IR spectra,⁷³⁻⁷⁴ with peaks corresponding to functional groups appearing in addition to changes in peaks corresponding with changes to the edge structure. These changes are analogous to

the changes appearing in the Raman D mode due to the amount of disorder in the structure.

1.2.3 Computational studies of graphitic compounds

Computational studies are often performed to provide further understanding about graphitic materials. In particular, computational studies can provide information about the effect of edge structure on properties, and Raman spectra, of graphene.^{1-2, 61, 63, 75-77} Additionally, information on the spin polarisation and density of states of the structures can be obtained, as reported by Kawasaki *et al.*⁹

1.3 Theory of interaction between dipyrin and graphene

Information and understanding of the interaction between dipyrins and graphene is required to determine the suitability of these compounds for potential solar energy applications.

The simplest model and approach is to assume a singlet (π - π^*) state for the dipyrin, and a continuum of states for graphene, a problem which is well-known in quantum mechanics. This is a Fano resonance,⁷⁸⁻⁸⁰ and can be thought of as an interference between the transitions into the continuum and discrete state. In addition to this, the effect of vibrational modes on coupling between dipyrin and graphene states must also be understood.

Figure 1.9 through Figure 1.11 are used to describe the interaction between systems with discrete quantum states, including spin effects, and the effect of vibrational motion. Figure 1.9 shows the basic photophysical processes which can occur between the quantum states.

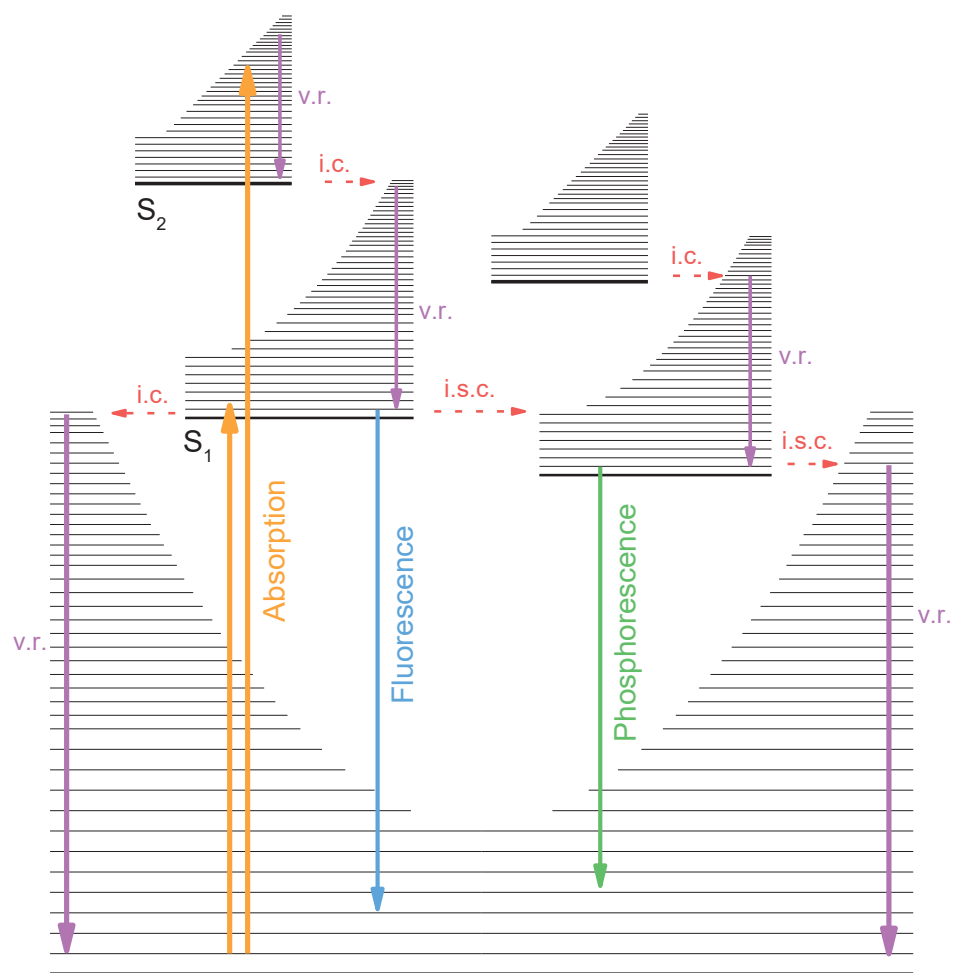


Figure 1.9 - Jablonski diagram showing photophysical processes (adapted from Ref. 60)

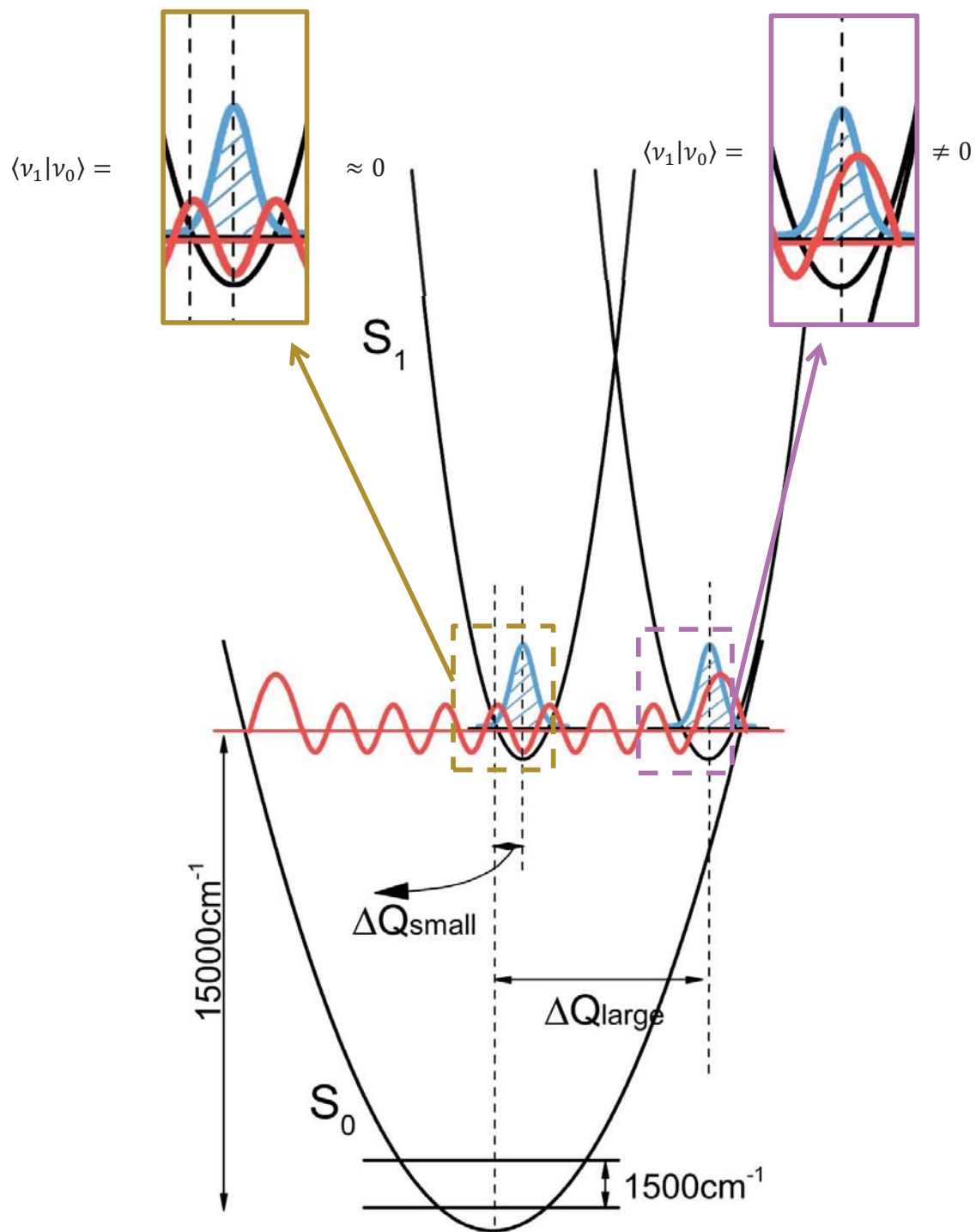


Figure 1.10 - Illustration of Franck-Condon factors for large and small vibrational mode displacements (ΔQ)

Figure 1.10 illustrates the total energy for a system having a single vibrational mode and two electronic states. Transitions between the states are governed by the Fermi Golden Rule (Equation (1-1), where V indicates coupling and ρ is a density of states term) and the Born-Oppenheimer approximation. This leads to the concept of Franck-Condon (FC) factors, also known as overlap integrals, which are illustrated in the figure. The relative positions of states S_0 and S_1 determine the magnitude of this overlap integral.

$$T_{i \rightarrow f} = \frac{2\pi}{\hbar} |\langle f | V | i \rangle|^2 \rho \quad (1-1)$$

Where, from the Born-Oppenheimer approximation: $|i\rangle = |v_g\rangle|g\rangle$ and $\langle f| = \langle e|\langle v_e|$ given that, for Figure 1.10: $i = S_0$ and $f = S_1$; $g = 0$ and $e = 1$.

Following on, and using notation where v_g and v_e represent vibrational wavefunctions, whilst g and e represent electronic wavefunctions, for radiative transitions, $V = e\vec{r}$. From this, the Fermi Golden Rule can be restated in the form of Equations (1-2) and (1-3).

$$T_{i \rightarrow f} = \frac{2\pi}{\hbar} |\langle e | \langle v_e | e\vec{r} | v_g \rangle | g \rangle|^2 \quad (1-2)$$

$$T_{i \rightarrow f} = \frac{2\pi}{\hbar} |\langle e | e\vec{r} | g \rangle \langle v_e | v_g \rangle|^2 \quad (1-3)$$

Where $\langle e | e\vec{r} | g \rangle$ represents the transition dipole moment (μ) and $\langle v_e | v_g \rangle$ represents the Franck-Condon factor (FC). Therefore, the Fermi Golden Rule can be restated finally as (1-4):

$$T_{i \rightarrow f} = \frac{2\pi\mu^2}{\hbar} (\text{FC})^2 \quad (1-4)$$

The magnitude of the Franck-Condon factor can be related to the structural rigidity of the molecules (dipyrrin) or substrate (graphene).

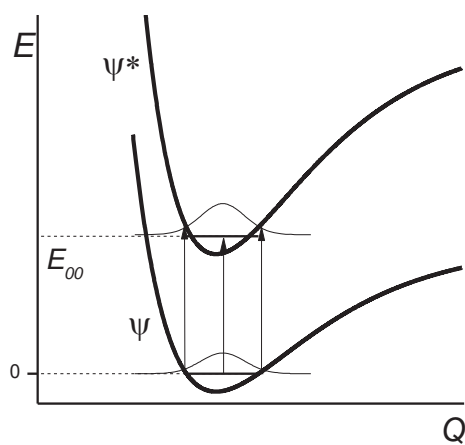
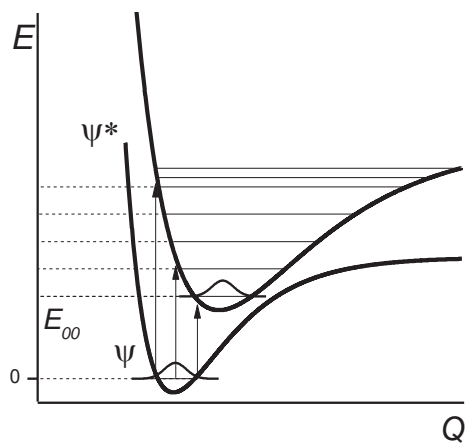
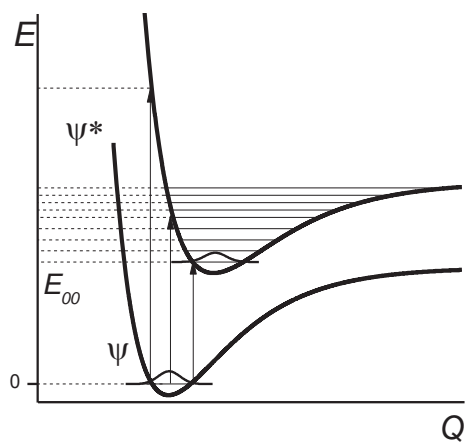


Figure 1.11 - Franck-Condon principle for a radiative transition (absorption). In this case, the FC factor involves vibrational wavefunctions from electronic states with different energies. Horizontal lines indicate transitions that will have significant intensity due to large FC factors (adapted from Ref. 60)

Small displacements, as in the case of rigid structures, lead to small values of ΔQ , whereas large displacements, for flexible structures, lead to large values of ΔQ , as demonstrated by Figure 1.10.

The Franck-Condon principle (Figure 1.11) requires transitions between quantum states to conserve nuclei momentum. This leads to nuclei needing to be stationary during a transition, irrespective of whether the transition is radiative. The assumption of a system with a single vibrational mode and two electronic states is reasonable for the dipyrin component of these structures, graphene has a continuum of electronic states, leading to the introduction of a density of states into the system. This means the value of ρ in the Fermi Golden Rule expression is no longer equal to 1, leading to a situation where Figure 1.10 would consist of an infinite number of S_1 states. Consequently, there is a very high probability there will be an S_1 state that gives a large FC factor with S_0 allowing rapid nonradiative passage back to the ground state.

Time-resolved spectroscopy methods, such as absorption, fluorescence, and Raman, are used to determine rates of transitions experimentally. The time scale of the measurement is determined by the lifetime of the quantum states. The radiative lifetime of BODIPYs are generally on the order of a few nanoseconds,⁵⁹ which is fairly long for an organic chromophore.

1.4 Stability of aromatic compounds

The well-known Hückel $4n + 2$ rule describes the stability of benzene compared to cyclobutadiene, however it is strictly only valid for monocyclic conjugated systems. As such, many attempts were made to extend this to polycyclic systems.⁸¹ Based on the work of Robinson, the Clar π -sextet rule states that the Kekulé

resonance structure with the largest number of benzene-like moieties (aromatic sextets) is the most important for the characterisation of properties.⁸¹⁻⁸² These sextets symbolise six π -electrons in a system, and are separated from adjacent rings by C-C single bonds. They are represented by a circle inside the hexagonal six-membered ring, and symbolise the mobility of the π -electrons. An example of the Kekulé and Clar structures of naphthalene are shown in Figure 1.12. The two orange Clar structures represent two resonance structures for naphthalene, however, as the sextet can migrate from one ring to another, the Clar structure shown in black gives a more accurate representation of the true structure of naphthalene. Whilst the two double bonds do not need to be explicitly stated, they are included here.

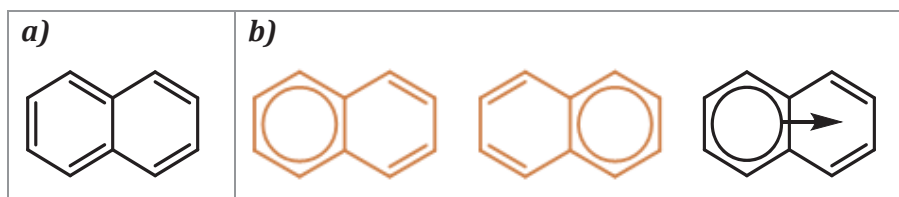


Figure 1.12 - Kekulé (a) and Clar (b) representations of naphthalene

Naphthalene is not as stable as benzene, and anthracene is more reactive still.⁸³ This trend continues throughout this series, and indicates that a single sextet does not provide stability for structures with more than one 6-membered ring. From this, Clar proposed that the inherent sextet in benzene explains its stability, and that the benzenoid rings, and thus aromatic sextets, in a structure, will have higher stability than the aromatic rings.⁸² This is supported by the relative stabilities of anthracene and phenanthrene (Clar structures shown in Figure 1.13), which share the same number of rings and atoms, but with phenanthrene being significantly more stable than anthracene. The higher stability of phenanthrene is explained in the Clar description by it having two aromatic sextets, as opposed to anthracene having a single aromatic sextet.

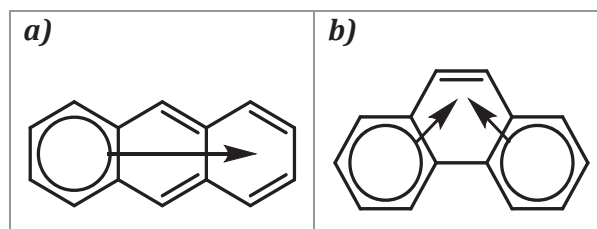


Figure 1.13 - Clar structures of: a) anthracene; and b) phenanthrene

Clar structures can be prepared for aromatic structures of any size, and are often used to describe graphene nanoribbon fragments used in density functional theory (DFT) calculations, with Clar theory used to interpret electronic properties and stability of nanoribbons.¹ Herein, chemical structures will be presented using Clar structures. This enables simple comparisons of relative stability to be made, and clearly shows the benzenoid character of aromatic compounds presented.

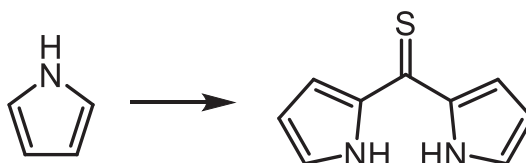
Chapter 2. Synthetic methods

This chapter describes the synthesis of dipyrryn compounds and the BODIPY-functionalisation of both small aromatic analogue compounds and graphene nanoribbons. Of the compounds whose synthesis is described in 2.2, only phenol/BODIPY and aniline/BODIPY have been previously described in the literature. Chemicals were used as received from Sigma-Aldrich, and solvents were dried over molecular sieves prior to use.

2.1 Synthesis of dipyrryn compounds

The typical procedures for dipyrryn synthesis (outlined below) were scaled as required.

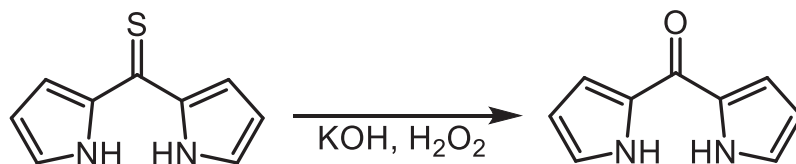
2.1.1 Thioketone dipyrryn



In accordance with literature,⁵⁸ thiophosgene (1.5 mL, 0.020 mol) was dissolved in toluene (anhydrous, 7.5 mL) on ice in a round-bottom flask with stirring. A solution of pyrrole (3.0240 g, 0.045 mol) in THF (anhydrous, 7.5 mL) was added dropwise to the thiophosgene mixture. The reaction mixture was stirred for 5 minutes on ice, then for a further 30 minutes at room temperature. The solvent was then removed *in vacuo*. The near-solvent-free compound was dissolved in DCM and passed through a silica-gel plug to remove impurities. The solvent was removed *in vacuo*, and the red solid material dried overnight under high vacuum, yielding 1.3152 g (7.46 mmol, 37.5 %).

^1H NMR (400 MHz, CDCl_3): δ 9.77 (br s, 2H), 7.21 (td, $J = 2.70$ Hz, 1.30 Hz, 2H), 7.05 (dd, $J = 2.45$ Hz, 1.30 Hz, 2H), 6.41 (dt, $J = 3.93$ Hz, 2.54 Hz, 2H) ppm

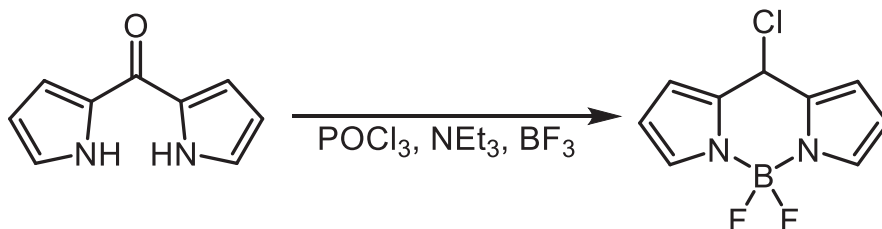
2.1.2 Ketone dipyrin



Thioketone dipyrin (1.3152 g, 7.46 mmol) and KOH (1.6959 g, 0.030 mol) were dissolved in MeOH (15 mL) with stirring on ice. H_2O_2 (30% aq., 5.5 mL) was added dropwise, and the mixture then refluxed for 10 minutes. Additional H_2O_2 was added dropwise down the condenser to the red-coloured solution, the colour was observed to turn completely yellow. 20 mL H_2O was added and the mixture then cooled on ice. The precipitated product was then filtered and dried overnight under high vacuum, producing 0.5188 g (3.24 mmol, 43.4 %) of light brown powder.

^1H NMR (400 MHz, CDCl_3): δ 9.69 (br s, 2H), 7.16 (s, 2H), 7.08 (s, 2H), 6.35 (d, $J = 3.67$ Hz, 2H) ppm

2.1.3 Cl-BODIPY



Ketone dipyrin (4.1521 g, 0.026 mol) was dissolved in minimal 1,2-dichloroethane (DCE) (anhydrous, 20 mL) in an oven-dried 50 mL double-necked round-bottom flask, and placed under Ar atmosphere. POCl_3 (4.5 mL, 0.048 mol) was injected into the mixture, and the mixture refluxed for 3 hours. After cooling on ice, NEt_3 (35 mL, 0.251 mol) was added slowly. BF_3 diethyl etherate (35 mL, 0.279 mol)

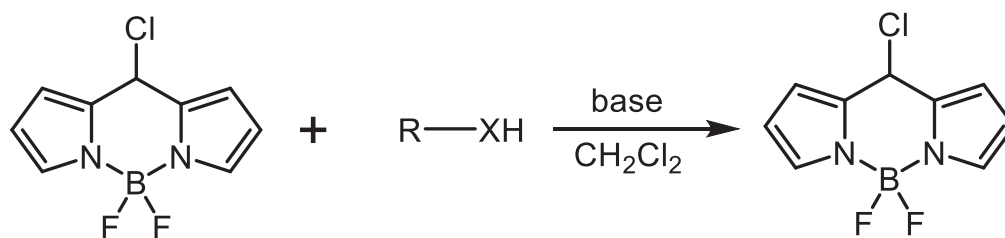
was then injected into the mixture, which was then stirred for 2 hours at room temperature. The mixture was then poured out into Et₂O (300 mL) and washed with H₂O. The ether layer was dried over MgSO₄, filtered, and solvent removed. The product was then purified on a silica plug (silica, DCM:petroleum ether, 1:1 moving to 2:1). After solvent was removed, the product was dried under high vacuum overnight, giving 3.0391 g (0.013 mol, 51.8 %) of bright red crystalline product.

¹H NMR (700 MHz, CDCl₃): δ 7.88 (s, 2H), 7.40 (d, *J* = 4.38 Hz, 2H), 6.58 (d, *J* = 4.19 Hz, 2H) ppm

¹³C NMR (175 MHz, CDCl₃): δ 145.1, 141.2, 134.0, 129.3, 119.1 ppm

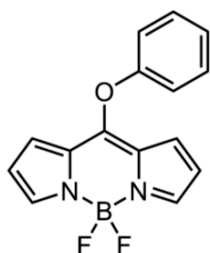
2.2 Functionalisation of small-analogue compounds

The functionalisation of small-analogue compounds with BODIPY follows the general synthetic method:



Where X is generally O or NH, and R is aromatic.

2.2.1 Phenol/BODIPY

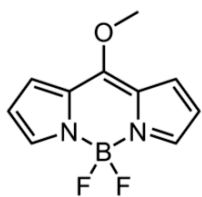


The phenol/BODIPY compound was synthesised according to the procedure of Dehaen *et al.*⁴⁹ Phenol (28.3 mg, 0.301 mmol) and K₂CO₃ (60.3mg, 0.436 mmol) were added to Cl-BODIPY (53.6 mg, 0.236 mmol) in DCM (anhydrous, 3 mL) and the mixture stirred for two hours under Ar atmosphere. The mixture was poured out into Et₂O (25 mL), washed with saturated Na₂CO₃ solution (25 mL, aq.),

and the solvent removed from the organic layer *in vacuo*. The product was then purified using a silica plug (silica, DCM/Petroleum ether, 1:1, v/v). Once dry, 0.0625 g (0.220 mmol, 92.9 %) of yellow product was obtained, although minimal impurities were present.

¹H NMR (400 MHz, CDCl₃): δ 7.74 (s, 2H), 7.50 (t, *J* = 7.44, 2H), 7.39 (t, *J* = 7.75, 1H), 7.27 (d, *J* = 1.31 Hz, 1H), 7.25 (d, *J* = 0.95 Hz, 1H), 6.68 (d, *J* = 4.10 Hz, 2H), 6.40 (d, *J* = 4.28 Hz, 2H) ppm

2.2.2 MeO/BODIPY



This compound was made during an attempt to synthesise phenol/BODIPY on a larger scale than previously using NEt₃ as base in place of K₂CO₃. The synthetic route follows, with an explanation of product formation.

(a) Synthetic method

Phenol (37.1 mg, 0.394 mmol) and NEt₃ (120 μL, 0.860 mmol) were added to Cl-BODIPY (90.4 mg, 0.399 mmol) in DCM (anhydrous, 4 mL) with stirring, and the mixture stirred for an hour under Ar atmosphere, until the reaction was determined to be complete by TLC. The mixture was extracted into Et₂O (25 mL), washed with saturated Na₂CO₃ solution (25 mL, aq.), and the solvent removed from the organic phase *in vacuo* until near dryness. MeOH (approx. 2 mL) was added to the near dry material and the solvent then partially removed *in vacuo*, during which a white vapour formed in conjunction with the formation of a purple crystalline precipitate. The mixture was then left to stand overnight at room temperature in a sealed vessel. The crystalline material was then filtered, washed with cyclohexane, and dried under high vacuum, yielding 0.0361 g (0.163 mmol, 41.2 %) of purple product.

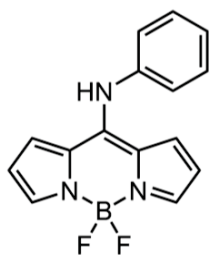
^1H NMR (400 MHz, CDCl_3): δ 7.75 (s, 2H), 7.38 (d, $J = 4.16$ Hz, 2H), 6.54 (d, $J = 4.25$ Hz, 2H), 4.50 (s, 3H) ppm

(b) Discussion of product

The ^1H NMR of the product from (a) does not agree with that of the desired product of phenol/BODIPY. The NMR does indicate, however, the presence of BODIPY and a $-\text{OCH}_3$ group. As such, it was decided to consult the literature for a MeO/BODIPY structure for comparison. The MeO/BODIPY structure found has been reported previously,^{49, 55} and the reported ^1H NMR of this agrees with the product from this reaction.

During this reaction, the product of phenol/BODIPY was formed, however, during the purification process, upon addition of MeOH, the phenol structure was replaced by MeO.

2.2.3 Aniline/BODIPY



As with the phenol/BODIPY compound, the aniline/BODIPY compound was synthesised to confirm the success of the literature method prior to its adaptation for larger aminated aromatic carbon compounds. Unlike the phenol synthesis which required an additional base, the literature method for aniline/BODIPY uses excess aniline as the base. Whilst this method was found to work for aniline as in (a) below, as the number of C-rings increases in these aminated compounds, they become more expensive, therefore the use of additional base was also investigated. Due to the successful use of additional base in (b), all novel syntheses involving aminated aromatic carbon compounds utilise the additional base as opposed to relying solely on the compound acting as the base.

(a) Literature procedure

The aniline/BODIPY compound was synthesised according to the procedure of Dehaen et al.⁴⁹ Aniline (30.5 mg, 0.327 mmol) was added to Cl-BODIPY (23.9 mg, 0.106 mmol) in DCM (anhydrous, 1 mL), and the mixture stirred under Ar atmosphere for 2 hours, until the reaction was determined to be complete by TLC. The product was purified using the method for phenol/BODIPY (2.2.1).

Initial ¹H NMR showed significant impurities, so the compound was purified using silica gel chromatography, in accordance with literature⁵⁵ (silica, EtOAc/Hex, 1:4, v/v). After removal of solvent, 0.0179g (0.063 mmol, 59.9 %) of yellow crystalline solid product was obtained with some impurities.

¹H NMR (400 MHz, CDCl₃): δ 7.91 (s, 1H), 7.60 (s, 2H), 7.53 (m, 3H), 7.42 (d, *J* = 2.17, 1H), 7.39 (d, *J* = 1.96 Hz, 1H), 6.51 (d, *J* = 3.86 Hz, 2H), 6.33 (dd, *J* = 3.20 Hz, *J* = 2.18, 2H) ppm

(b) Modified procedure

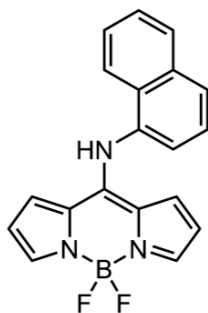
This procedure has been repeated using 2 equivalents of NEt₃ as base instead of excess aniline in order to minimise usage of aminated compounds. This method was successful in forming the desired product in 50% yield.

¹H NMR (700 MHz, CDCl₃): δ 8.00 (s, 1H), 7.58 (s, 2H), 7.52 (m, 3H), 7.38 (dd, *J* = 8.04 Hz, 1.72 Hz, 2H), 6.51 (d, *J* = 2.79 Hz), 6.32 (dd, *J* = 3.73 Hz, 1.85 Hz, 2H) ppm

¹³C NMR (175 MHz, CDCl₃): δ 147.7, 137.5, 135.4, 130.5, 129.5, 126.9, 124.0, 120.4, 114.6 ppm

ESI-MS: Calculated for $C_{15}H_{12}N_3BF_2 = 283.1087$; Measured = 264.1098
(Agrees with calculated for $C_{15}H_{12}N_3BF = 264.1103$)

2.2.4 1-naphthylamine/BODIPY



This reaction was performed using K_2CO_3 as base in one synthesis, and NEt_3 in the other. The reaction utilising K_2CO_3 as base did not result in the desired product. The successful reaction is described here.

1-naphthylamine (74.2 mg, 0.518 mmol) and NEt_3 (150 μ L, 1.075 mmol) were added to Cl-BODIPY (113.2 mg, 0.500 mmol) in DCM (anhydrous, 5 mL), and the mixture stirred under Ar atmosphere at room temperature for 22 $\frac{1}{2}$ hours until complete by TLC.

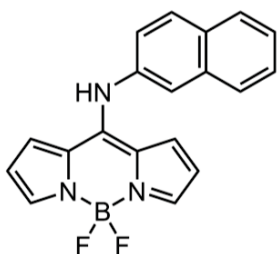
To purify the product, a recrystallization in cyclohexane was attempted, as this would be potentially simpler than column chromatography. Some product would not dissolve so the solution was decanted off, and the insoluble product left to dry. No material precipitated out of the solution over a weekend, therefore it was assumed there was no desired product present. 1H NMR was performed on the insoluble material, but did not contain the expected three doublets from BODIPY, however the integrals agreed with the product potentially being formed. X-ray crystallographic results are described in 2.4.1. The product was obtained in high purity with 87% yield.

1H NMR (700 MHz, $CDCl_3$): δ 11.53 (s, 1H), 9.46 (s, 1H), 8.00 (m, 1H), 7.95 (d, 2H, $J = 7.27$ Hz), 7.56 (s, 1H), 7.55 (m, 2H), 7.54 (s, 2H), 7.48 (m, 1H), 6.53 (s, 1H), 6.22 (s, 2H) ppm

^{13}C NMR (175 MHz, CDCl_3): δ 148.9, 134.8, 134.6, 134.2, 129.8, 129.6, 128.6, 127.8, 127.3, 126.0, 125.5, 124.0, 122.4, 114.4 ppm

ESI-MS: Calculated for $\text{C}_{19}\text{H}_{14}\text{N}_3\text{BF}_2$ = 333.1243; Measured = 314.1252
(Agrees with calculated for $\text{C}_{19}\text{H}_{14}\text{N}_3\text{BF}$ = 314.1259)

2.2.5 2-naphthylamine/BODIPY



Cl-BODIPY (117.1 mg, 0.517 mmol) was dissolved in DCM (anhydrous, 5 mL). To this, 2-naphthylamine (75.4 mg, 0.527 mmol) and distilled NEt_3 (150 μL , 1.075 mmol) were added, and the mixture stirred under Ar atmosphere for 3 hours until reaction complete by TLC. After unsuccessful attempt at purification by recrystallization in cyclohexane, product was purified using column chromatography (silica, EtOAc/Hex, 1:4, v/v). ^1H NMR showed impurities were still present. Further purification was attempted by recrystallization in cyclohexane, however, a large amount of insoluble material remained. ^1H NMR was performed on both the supernatant and insoluble material, and showed the insoluble material was the desired product in high purity as a yellow/brown crystalline solid, in 72% yield (0.1241 g, 0.373 mmol).

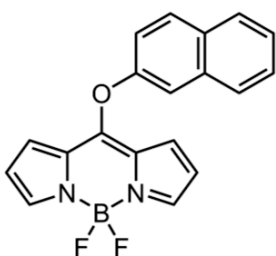
^1H NMR (700 MHz, CDCl_3): δ 8.09 (s, 1H), 7.98 (d, J = 8.72 Hz, 1H), 7.94 (d, J = 7.95 Hz, 1H), 7.88 (s, 1H), 7.86 (d, J = 7.68 Hz, 1H), 7.61 (m, 4H), 7.56 (dd, J = 8.49 Hz, 2.17 Hz, 1H), 6.56 (d, J = 2.73 Hz, 2H), 6.31 (dd, J = 3.94 Hz, 2.02 Hz, 2H) ppm

^{13}C NMR (175 MHz, CDCl_3): δ 147.5, 135.7, 134.8, 133.7, 133.0, 130.6, 128.1, 128.2, 127.6, 127.4, 125.2, 124.2, 124.1, 120.6, 114.7, 26.9 ppm

127.4, 127.1, 126.2, 126.1, 125.9, 124.4, 124.2, 123.7, 123.5, 123.3, 121.8, 119.7, 118.8, 118.4, 112.4, 107.6 ppm

ESI-MS: Calculated for $C_{28}H_{18}ON_4B_2F_4 = 524.1597$; Measured = 505.1610
(Agrees with calculated for $C_{28}H_{18}ON_4B_2F_3 = 505.1613$)

2.2.7 2-naphthol/BODIPY



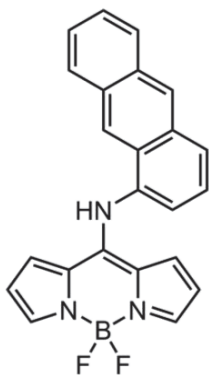
Cl-BODIPY (112.2 mg, 0.496 mmol) was dissolved in DCM (anhydrous, 5 mL). 2-naphthol (71.9 mg, 0.499 mmol) and distilled NEt₃ (145 μ L, 1.040 mmol) were added, and the reaction mixture stirred under Ar atmosphere at room temperature for 2 hours until complete by TLC. The product was purified using column chromatography (silica, EtOAc/Hex, 1:4, v/v) and characterised using ¹H NMR, which showed impurities in product. The product was then further purified by recrystallization in cyclohexane. The product was filtered and dried overnight under high vacuum. The product was obtained in a yield of 0.1297g (0.388 mmol, 77.8 %) of bright orange crystals.

¹H NMR (700 MHz, CDCl₃): δ 7.97 (d, $J = 8.90$ Hz, 1H), 7.93 (m, 1H), 7.85 (m, 1H), 7.76 (s, 2H), 7.72 (d, $J = 2.48$ Hz, 1H), 7.58 (m, 2H), 7.37 (dd, $J = 8.93$ Hz, 2.57 Hz, 1H), 6.72 (d, $J = 4.32$ Hz, 2H), 6.38 (d, $J = 4.11$ Hz, 2H) ppm

¹³C NMR (175 MHz, CDCl₃): δ 159.3, 153.3, 140.9, 133.8, 131.7, 130.8, 128.1, 127.9, 127.5, 127.0, 126.6, 126.3, 119.2, 116.9, 116.9 ppm

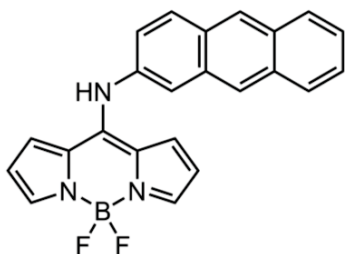
ESI-MS: Calculated for $C_{19}H_{13}ON_2BF_2 = 334.1084$; Measured = 315.1096
(Agrees with calculated for $C_{19}H_{13}ON_2BF = 315.1099$)

2.2.9 1-aminoanthracene/BODIPY



Cl-BODIPY (67.4 mg, 0.298 mmol) was dissolved in DCM (anhydrous, 3 mL). 1-aminoanthracene (56.9 mg, 0.294 mmol) and *N,N*-Diisopropylethylamine (110 μ L, 0.631 mmol) were added, and the mixture stirred at room temperature under Ar atmosphere until TLC indicated no unreacted starting materials were present. The product was then purified using column chromatography (alumina, CHCl_3 /Hexane, 2:1, v/v) and characterised using ^1H NMR spectroscopic analysis, which showed impurities in product. The product was then further purified by recrystallization in cyclohexane. Oily product was present But was too impure to determine whether the desired product was obtained.

2.2.10 2-aminoanthracene/BODIPY



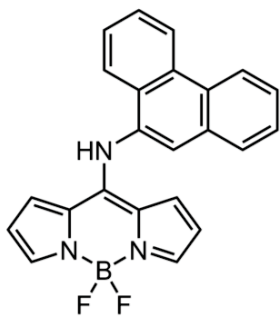
Cl-BODIPY (67.7 mg, 0.299 mmol) was dissolved in DCM (anhydrous, 3 mL). 2-aminoanthracene (56.7 mg, 0.293 mmol) and *N,N*-Diisopropylethylamine (110 μ L, 0.631 mmol) were added, and the mixture stirred at room temperature under Ar atmosphere until TLC indicated no unreacted starting materials were present. The product was then purified using column chromatography (silica, DCM/Hexane, 4:1, v/v) and characterised using ^1H NMR. Initial NMR sample was observed to decompose and form precipitated product in CDCl_3 therefore obtained NMR in Acetonitrile- d_3 . 0.0201 g (0.052 mmol, 17.9 %) of product was afforded by these conditions with high purity.

^1H NMR (700 MHz, CD_3CN): δ 9.56 (s, 1H), 8.63 (s, 1H), 8.57 (s, 1H), 8.22 (d, $J = 8.36$ Hz, 1H), 8.16 (s, 1H), 8.10 (m, 2H), 7.57 (m, 2H), 7.51 (m, 3H), 6.74 (s, 2H), 6.33 (s, 2H) ppm

^{13}C NMR (175 MHz, CDCl_3): δ 147.7, 134.5, 133.7, 132.1, 131.9, 131.0, 130.3, 127.9, 127.8, 126.6, 126.4, 126.0, 124.9, 124.0, 123.9, 120.7, 113.9 ppm

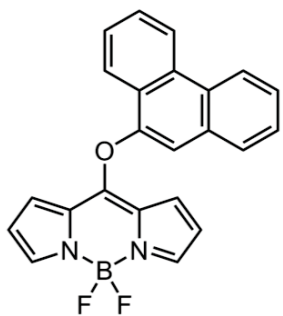
ESI-MS: Calculated for $\text{C}_{23}\text{H}_{16}\text{N}_3\text{BF}_2 = 383.1390$; Measured = 383.1400

2.2.11 9-aminophenanthrene/BODIPY



Cl-BODIPY (68.2 mg, 0.301 mmol) was dissolved in DCM (anhydrous, 3 mL). 9-aminophenanthrene (58.6 mg, 0.303 mmol) and *N,N*-Diisopropylethylamine (110 μL , 0.631 mmol) were added, and the mixture stirred at room temperature under Ar atmosphere until TLC indicated no unreacted starting materials were present. The product was then purified using column chromatography (alumina, $\text{CHCl}_3/\text{Hexane}$, 2:1, v/v) and characterised using ^1H NMR, which showed impurities in product. These impurities were not able to be removed through further column chromatography or recrystallization methods. The yield of this impure product was not calculated.

2.2.12 9-hydroxyphenanthrene/BODIPY



Cl-BODIPY (67.6 mg, 0.299 mmol) was dissolved in DCM (anhydrous, 3 mL). 9-hydroxyphenanthrene (58.8 mg, 0.302 mmol) and *N,N*-Diisopropylethylamine (110 μL , 0.631 mmol) were added, and the mixture stirred at room temperature under Ar atmosphere until TLC indicated no unreacted starting materials were present. The product was then purified using

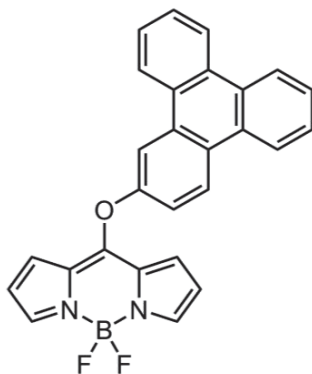
column chromatography (alumina, CHCl₃/Hexane, 2:1, v/v) affording 0.0265 g (0.069 mmol, 23.1 %) of product with minor impurities.

¹H NMR (700 MHz, CDCl₃): δ 8.75 (d, *J* = 8.36 Hz, 1H), 8.67 (d, *J* = 8.18 Hz, 1H), 8.44 (dd, *J* = 8.46 Hz, 1.20 Hz, 1H), 8.01 (s, 2H), 7.81 (m, 1H), 7.72 (m, 1H), 7.55 (m, 2H), 7.46 (m, 1H), 6.78 (d, *J* = 4.27 Hz, 2H), 6.48 (d, *J* = 4.07 Hz, 2H), 5.90 (s, 1H) ppm

¹³C NMR (175 MHz, CDCl₃): δ 147.5, 145.6, 141.0, 136.2, 132.4, 132.0, 131.3, 128.6, 127.5, 127.1, 126.2, 125.7, 124.9, 124.7, 123.6, 122.7, 122.5, 119.4, 109.0, ppm

ESI-MS: Calculated for C₂₃H₁₆ON₂BF₂ = 385.1215; Measured = 385.1318

2.2.13 2-hydroxytriphenylene/BODIPY



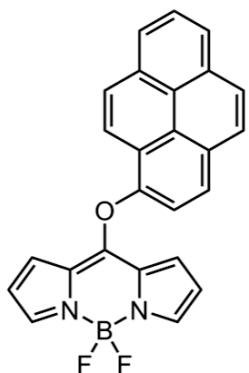
Cl-BODIPY (75.0 mg, 0.331 mmol) was dissolved in DCM (anhydrous, 5 mL). 2-hydroxytriphenylene (81.3 mg, 0.333 mmol) and NEt₃ (100 μL, 717 mmol) were added, and the mixture stirred at room temperature under Ar atmosphere. After 20 minutes a yellow precipitate had formed, and TLC confirmed no unreacted Cl-BODIPY was present. The precipitate was filtered, washed with cold DCM, and dried overnight under high vacuum, which afforded 0.0535g (0.123 mmol, 37.2 %) of yellow product in high purity.

¹H NMR (700 MHz, CDCl₃): δ 8.77 (d, *J* = 8.79 Hz, 1H), 8.70 (m, 2H), 8.64 (m, 1H), 8.52 (d, *J* = 8.20 Hz, 1H), 8.51 (d, *J* = 2.64 Hz, 1H), 7.77 (s, 2H), 7.73 (m, 3H), 7.68 (m, 1H), 7.54 (dd, *J* = 8.82 Hz, 2.47 Hz, 1H), 6.77 (d, *J* = 4.02 Hz, 2H), 6.38 (dd, *J* = 3.98 Hz, 1.40 Hz, 2H) ppm

^{13}C NMR (175 MHz, CDCl_3): δ 159.4, 154.7, 140.9, 131.9, 130.3, 129.9, 128.9, 128.7, 128.5, 128.4, 127.9, 127.7, 127.7, 126.9, 126.3, 126.0, 123.7, 123.6, 123.5, 123.5, 119.3, 117.0, 114.2 ppm

ESI-MS: Calculated for $\text{C}_{27}\text{H}_{17}\text{ON}_2\text{BF}_2$ = 434.1396; Measured = 415.1412
(Agrees with calculated for $\text{C}_{27}\text{H}_{17}\text{ON}_2\text{BF}$ = 415.1412)

2.2.14 1-hydroxypyrene/BODIPY



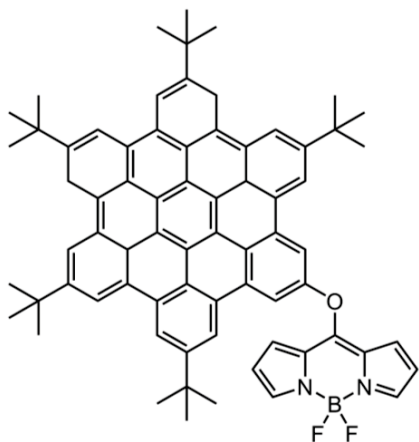
Cl-BODIPY (66.5 mg, 0.293 mmol) was dissolved in DCM (anhydrous, 3 mL). 1-hydroxypyrene (64.5 mg, 0.296 mmol) and *N,N*-Diisopropylethylamine (110 μL , 0.631 mmol) were added, and the mixture stirred at room temperature under Ar atmosphere until TLC indicated no unreacted starting materials were present. The product was purified using a silica plug (silica, DCM/Hexane, 2:1, v/v), affording 0.0938 g (0.229 mmol, 77.9 %) of yellow product in high purity.

^1H NMR (700 MHz, CDCl_3): δ 8.29 (d, J = 7.48 Hz, 1H), 8.24 (dd, J = 9.78 Hz, 7.77 Hz, 2H), 8.20 (d, J = 9.21 Hz, 1H), 8.16 (m, 3H), 8.10 (m, 1H), 7.87 (d, J = 7.91 Hz, 1H), 7.75 (s, 2H), 6.51 (d, J = 4.28 Hz, 2H), 6.31 (dd, J = 4.27 Hz, 1.42 Hz, 2H) ppm

^{13}C NMR (175 MHz, CDCl_3): δ 160.3, 148.6, 140.8, 131.2, 131.1, 130.1, 129.4, 128.1, 127.0, 126.7, 126.2, 126.1, 126.0, 125.8, 125.6, 124.5, 122.4, 119.5, 117.8, 116.9 ppm

ESI-MS: Calculated for $\text{C}_{25}\text{H}_{15}\text{ON}_2\text{BF}_2$ = 408.1240; Measured = 408.1232

2.2.15 HBC(*t*-Bu)₅OH/BODIPY



Cl-BODIPY (5.1 mg, 0.023 mmol) was dissolved in DCM (anhydrous, 0.5 mL). HBC(*t*-Bu)₅OH (18.3 mg, 0.022 mmol) dissolved in 0.5 mL DCM, and *N,N*-Diisopropylethylamine (10 μ L, 0.057 mmol) were added, and the mixture stirred at room temperature under Ar atmosphere until

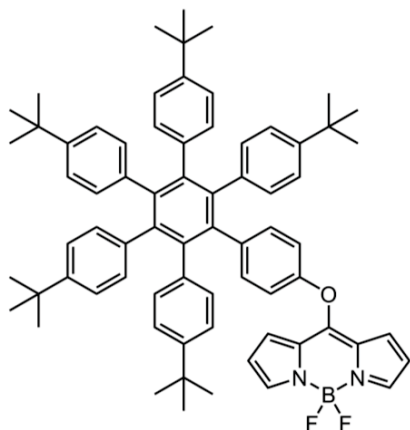
TLC indicated no unreacted starting materials were present, at which time the solvent was removed *in vacuo* affording 0.0224 g (0.022 mmol, 99.7%) of final product. Minor impurities were found to be present that originated from starting material.

¹H NMR (700 MHz, CDCl₃): δ 9.32 (m, 6H), 9.27 (s, 2H), 9.04 (s, 2H), 8.95 (s, 2H), 7.81 (s, 2H), 6.83 (d, $J = 3.73$ Hz, 2H), 6.37 (dd, $J = 4.42$ Hz, 2.22 Hz, 2H), 1.85 (s, 9H), 1.84 (s, 18H), 1.78 (s, 18H) ppm

¹³C NMR (175 MHz, CDCl₃): δ 160.4, 153.6, 149.6, 149.5, 149.4, 140.6, 133.7, 130.6, 130.5, 130.2, 129.1, 129.1, 128.2, 126.7, 126.5, 125.3, 124.7, 124.0, 123.8, 123.6, 120.8, 120.4, 120.1, 119.5, 119.2, 119.1, 119.0, 116.9, 115.7, 112.9, 35.8, 35.8, 32.0, 18.7, 17.4, 12.0 ppm

ESI-MS: Calculated for C₇₁H₆₃ON₂BF₂ +H= 1009.5074; Measured = 1009.5074

2.2.16 HPB(*t*-Bu)₅OH/BODIPY



Cl-BODIPY (16.2 mg, 0.072 mmol) was dissolved in dry DCM (anhydrous, 2 mL). HPB(*t*-Bu)₅OH (59.3 mg, 0.071 mmol) and *N,N*-Diisopropylethylamine (30 μ L, 0.172 mmol) were added, and the mixture stirred at room temperature under Ar atmosphere until TLC indicated no unreacted starting materials were

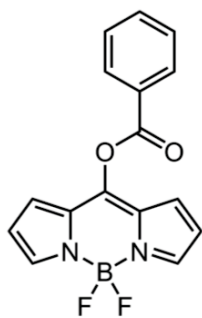
present. The product was purified using column chromatography (silica, CHCl₃/Hexane, 2:1, v/v), affording 0.0665g (0.065 mmol, 91.3 %) of the yellow product in high yield.

¹H NMR (700 MHz, CDCl₃): δ 7.68 (s, 2H), 7.01 (m, 2H), 6.91 (m, 4H), 6.81 (m, 6H), 6.75 (m, 6H), 6.69 (m, 2H), 6.65 (m, 4H), 6.55 (d, J = 4.27 Hz, 2H), 6.37 (dd, J = 4.16 Hz, 1.75 Hz, 2H), 1.13 (s, 18H), 1.10 (s, 18H), 1.10 (s, 9H) ppm

¹³C NMR (175 MHz, CDCl₃): δ 159.7, 152.9, 148.1, 147.6, 147.6, 141.1, 141.0, 140.5, 140.2, 140.1, 137.8, 137.7, 137.6, 133.7, 131.2, 131.0, 130.9, 126.5, 126.2, 123.5, 123.2, 123.1, 118.2, 116.5, 34.2, 34.1, 31.2, 31.2 ppm

ESI-MS: Calculated for C₇₁H₇₅ON₂BF₂ = 1021.1758; Measured = 1059.5604 (Agrees with calculated for C₇₁H₇₅ON₂BF+K = 1059.5572)

2.2.17 Benzoic acid/BODIPY



Cl-BODIPY (74.7 mg, 0.330 mmol) was dissolved in dry DCM (anhydrous, 3 mL). Benzoic acid (40.3 mg, 0.330 mmol) and *N,N*-Diisopropylethylamine (140 μ L, 0.803 mmol) were added, and the mixture stirred at room temperature under Ar atmosphere until TLC indicated no unreacted starting materials were present. TLC indicated two products formed. The crude material was purified with silica-gel chromatography (silica, CHCl₃/Hexane, 1:1, v/v). The two products formed were found to be mono- (0.0431 g, 0.138 mmol, 41.9 %) and di-BODIPY (0.0090g, 0.018 mmol, 5.4%) substituted. The mono-substituted product was further analysed and used in spectroscopic studies.

¹H NMR (700 MHz, CDCl₃): δ 8.16 (m, 2H), 7.88 (s, 2H), 7.68 (m, 1H), 7.53 (m, 2H), 7.41 (d, J = 4.18 Hz, 2H), 6.58 (d, J = 4.18 Hz, 2H) ppm

¹³C NMR (175 MHz, CDCl₃): δ 159.9, 142.6, 138.7, 132.1, 131.6, 128.1, 126.8, 126.4, 116.6, 116.6 ppm

ESI-MS: Calculated for C₁₆H₁₁O₂N₂BF₂ = 312.0876; Measured = 293.0888 (Agrees with calculated for C₁₆H₁₁O₂N₂BF = 293.0892)

2.3 Functionalisation of graphene nanoribbons

Functionalisation of graphene nanoribbons is achieved using a method based on those described for small-analogue compounds (2.2).

2.3.1 Calculation of nanoribbon quantity

In order to determine reaction conditions, the approximate number of reacting carbon atoms needs to be calculated, based on the amount of nanoribbons present.

The quantity of nanoribbons present can be determined via two methods; by finding the mass of GNRs in a pre-weighed flask following cutting, or by calculating the total mass of nanoribbon sheets cut into the vial from block measurements and microtome parameters.

The number of carbon atoms in a single ribbon can be found using equation (2-1), where $\rho(C_{lattice})$ is the density of carbon atoms in a graphene sheet (39 C/nm²), and A_{ribbon} is the area of the nanoribbon in nm², determined from average ribbon properties (in this study, an average nanoribbon size of 100 nm width and 5000 nm length was used).

$$\#C = \rho(C_{lattice}) \times A_{ribbon} \quad (2-1)$$

The mass of a single nanoribbon can then be determined using equation (2-2), where $M_r(C)$ is the molar mass of carbon, and N_A is the Avogadro constant.

$$m_{single} = \frac{\#C \times M_r(C)}{N_A} \quad (2-2)$$

Once the mass of nanoribbons to be used in the reaction ($m_{ribbons}$) has been determined, the number of nanoribbons can be determined using equation (2-3).

$$n_{ribbons} = \frac{m_{ribbons}}{m_{single}} \quad (2-3)$$

As only some edge atoms are expected to react with the Cl-BODIPY, the number of reacting carbons per nanoribbon must then be determined. To do this, an edge “unit cell” has been created which contains 4 edge atoms, but only 2 reacting atoms. The total number of edge unit cells ($n_{unit\ cells}$), and thus reacting edge atoms ($\#C_{reacting}$), for a single average ribbon can then be found using (2-4), where w_{ribbon} and l_{ribbon} are the width and length of the average ribbon respectively.

$$n_{unit\ cells} = 2 \left(\frac{w_{ribbon}}{0.42\ \text{nm}} \right) + 2 \left(\frac{l_{ribbon}}{0.42\ \text{nm}} \right) \quad (2-4)$$

$$\#C_{reacting} = n_{unit\ cells} \times 2$$

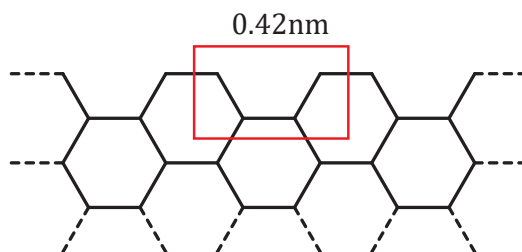


Figure 2.1 - GNR edge "unit cell"

The total number of reacting carbon atoms for the reaction can then be determined using (2-5).

$$r_{reacting} = \#C_{reacting} \times n_{ribbons} \quad (2-5)$$

The number of reacting edge atoms is equal to $n_{Cl-BODIPY}$ required for the reaction.

2.3.2 General reaction for BODIPY-functionalisation of graphene nanoribbons

Note: The quantity of Cl-BODIPY in the reaction mixture is found following the procedure described in 2.3.1.

As cut GNRs are suspended in dry DCM (1 mL) via sonication overnight at low power. To this, Cl-BODIPY and *N,N*-Diisopropylethylamine (30 μ L per 0.1 mmol Cl-BODIPY) are added, and the reaction mixture flushed with Ar. The reaction mixture is then sonicated for 24 hours, after which time, the reaction mixture is purified.

2.3.3 Purification of BODIPY-functionalised graphene nanoribbons

Purification of BODIPY-functionalised graphene nanoribbons, herein referred to as BODIPY-GNRs, is performed using multiple centrifugation cycles. All centrifugation steps are performed at 10,000 rpm for 10 minutes.

The reaction mixture is evenly divided into 1 mL Eppendorf tubes, and centrifuged to form a pellet of BODIPY-GNRs. The supernatant is carefully removed and set aside for absorption spectroscopy. Differences in the absorption spectrum of the supernatant compared to that of Cl-BODIPY indicate whether the reaction was successful.

1 mL dry DCM is added to the tubes containing BODIPY-GNR pellets, and the tubes are sonicated for 2-3 minutes to re-suspend the GNRs. Following resuspension, the solutions are transferred to clean Eppendorf tubes, prior to another centrifugation cycle. The process of resuspension followed by centrifugation is repeated until 2 cycles have been performed where no colour can be observed in the removed supernatant.

To confirm purification is complete, absorption spectroscopy is performed on removed supernatant, and a baseline of dry DCM used. Purification is complete when there is no detectable deviation from baseline in the absorption spectrum of the supernatant.

2.4 Crystallography

This section provides the results of crystallographic studies performed on structures unable to be characterised via NMR techniques. X-ray crystallographic information is provided in Table 2.1.

Table 2.1 - Crystallography data

	1-naphthylamine/BODIPY	1-naphthol/2xBODIPY	2-naphthol/2xBODIPY
Formula	C ₂₂ H ₂₂ B C _{10.50} F ₂ N _{3.50}	C ₂₈ H ₁₈ B ₂ F ₄ N ₄ O	C _{23.2} H _{15.2} B _{1.6} Cl _{2.4} F _{3.2} N _{3.2} O _{0.8}
Formula weight	401.96	524.08	514.76
Temperature (K)	293	293	183
Wavelength (Å)	1.54187	1.54187	1.54187
Crystal system	Triclinic	Monoclinic	Monoclinic
Space group	P-1	C2/c	P21/n
Unit cell lengths (Å)	a = 12.0218(3) b = 13.0172(3) c = 14.9049(11)	a = 26.9142(10) b = 7.4623(3) c = 26.5007(19)	a = 18.0447(5) b = 8.4885(2) c = 20.2930(14)
Unit cell angles (°)	α = 115.371(8) β = 97.560(7) γ = 100.355(7)	α = 90.0 β = 110.247(8) γ = 90.0	α = 90.0 β = 112.295(8) γ = 90.0
Unit cell volume (Å ³)	2015.3(2)	4993.6(5)	2876.0(3)
Z	4	8	5
D _{calc} (g cm ⁻³)	1.325	1.394	1.486
μ (mm ⁻¹)	1.341	0.897	3.395
F(000)	840	2144	1304
Reflns coll./unique	7408 / 4905	1717 / 1329	5408 / 4046
Data range	6.76° < θ < 72.0°	6.60° < θ < 42.1°	6.54° < θ < 72.1°
Index ranges	-14 ≤ h ≤ 14, -16 ≤ k ≤ 16, -18 ≤ l ≤ 16	-23 ≤ h ≤ 18, -6 ≤ k ≤ 6, -18 ≤ l ≤ 23	-19 ≤ h ≤ 22, -6 ≤ k ≤ 10, -24 ≤ l ≤ 24

2.4.1 1-naphthylamine/BODIPY

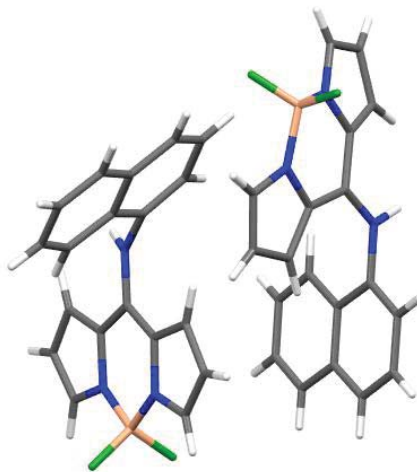


Figure 2.2 – Crystal structure of 1-naphthylamine/BODIPY

X-ray crystallographic measurements were performed on the insoluble material formed by the reaction (2.2.4) to determine the structure of the product formed. From Figure 2.2 it is evident the desired product has in fact formed.

2.4.2 1-naphthol/2xBODIPY

The 2:1 BODIPY:1-naphthol ratio indicated by the ^1H NMR spectrum was confirmed by X-ray crystallography, as can be seen in Figure 2.3.

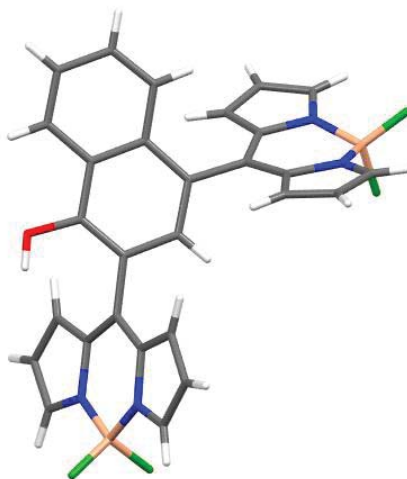


Figure 2.3 - Crystal structure of 1-naphthol/2xBODIPY

This phenomenon has not been reported in literature methods involving functionalisation with Cl-BODIPY, however, reactions between Cl-BODIPY and 1- or 2-naphthol have not been previously demonstrated in literature. It is possible the reactivity or resonance structures of naphthols may provide some answers.

The formation of C-C bonds between the analogue and BODIPY requires further investigation, as there are many possibilities for the mechanism of this reaction (this is discussed further in 3.4).

2.4.3 2-naphthol/2xBODIPY

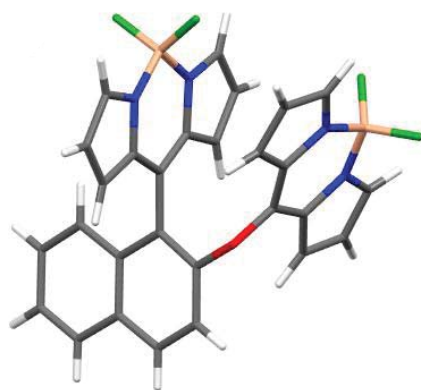


Figure 2.4 - Crystal structure of 2-naphthol/2xBODIPY

NMR spectroscopic analysis showed 2 BODIPY compounds present for each 2-naphthol compound. This was confirmed by X-ray crystallography, where two BODIPY molecules are attached to a single 2-naphthol molecule, as shown in Figure 2.4. As for the double substitution case observed for 1-naphthol, the formation of this product requires further investigation.

Chapter 3. Computational studies of graphene nanoribbons

Due to their large size, the analysis of graphene nanoribbons using traditional experimental methods is limited. The use of computational methods enable a more detailed investigation of GNR properties to be performed, which can then be related to experimental data to form a more complete picture of graphene nanoribbon properties and behaviours.

Due to their large size, graphene nanoribbons are unable to be studied computationally at a high level due to the time required for the calculation. Small analogue structures can be used to discover trends in carbon materials, with the results of these being extrapolated to give understanding of graphene.

Trends in Raman spectra caused by increasing the number of carbon rings in a structure have been investigated. The use of analogue structures can also provide information on trends associated with edge structure, i.e. armchair vs. zig-zag. Additionally, effects of internal structure on the Raman spectra can also be investigated through the study of larger, non-linear, analogues.

All computational studies have been performed using Amsterdam Density Functional (ADF) software, versions 2013.01 through 2016.02. ADF uses Slater-type orbital (STO) basis sets when performing calculations, as opposed to the more commonly used Gaussian-type orbitals (GTOs). Each basis set type has its own advantages and disadvantages,⁸⁴⁻⁸⁶ and most importantly its own notation. As such, all basis sets will be explicitly described.

3.1 Graphene analogue computational studies

All geometry optimisations of graphene analogue structures have been performed with a B3LYP (Becke, 3-parameter, Lee-Yang-Parr) hybrid functional and a DZP (double-zeta, 1 polarisation function) basis set. All frequency calculations were performed with a PBE (Perdew-Burke-Ernzerhof) functional and DZP basis set. This change of functional is due to ADF not supporting the hybrid B3LYP functional for use with analytical frequency calculations, meaning a numerical integration method would have been required, which is approximately 3 to 5 times slower than analytical frequency methods.⁸⁷

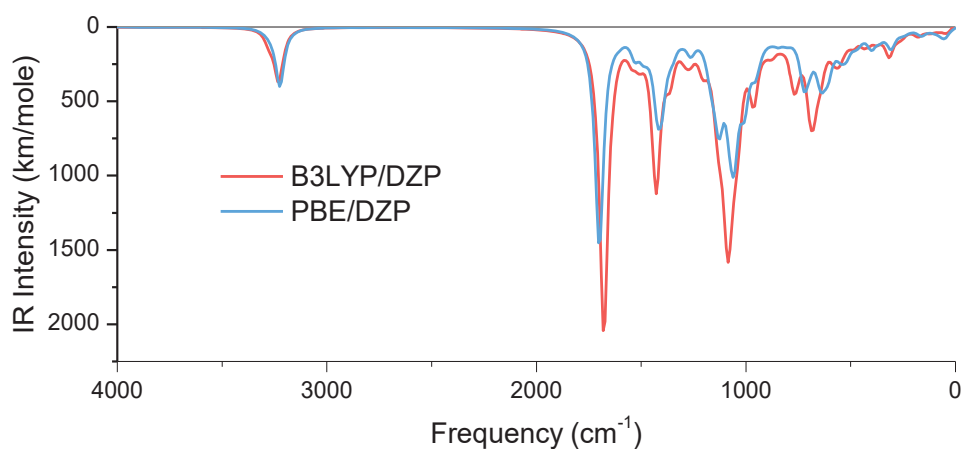


Figure 3.1 - Comparison between PBE and B3LYP functionals for frequency calculation for the transition state structure of phenol/BODIPY

The use of a simpler functional may lead to less accuracy in frequency calculations. Test calculations were performed using each functional, which were then compared, as shown in Figure 3.1. There are small differences in the intensities of bands, however, overall, the positions and number of peaks is consistent. In this specific example, the analytical PBE calculation took 6 hours and 8 minutes to perform, while the numerical B3LYP calculation took 82 hours and 43 minutes to perform. Due to the close agreement, and the significant computational time

difference, it was decided to use the analytical PBE method for frequency calculations. And although some accuracy may be lost with the use of PBE, using a single functional and basis set for all compounds makes direct comparisons across the range of compounds possible. The choice of functional and basis set is effectively determined by the largest structure in the series, as this will have the largest time cost.

3.1.1 Description of analogues

(a) Zig-zag edged structures

The four zig-zag edged linear structures studied were anthracene, pentacene, heptacene, and nonacene, the structures of which are shown in **Figure 3.2**.

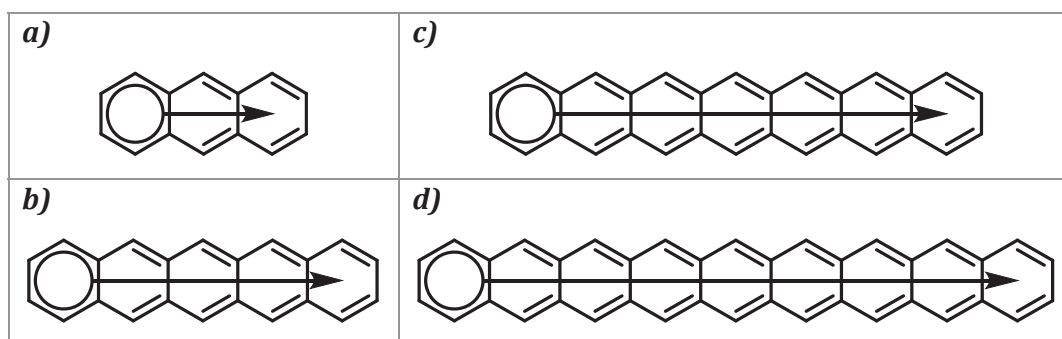


Figure 3.2 - Zig-zag edged structures: a) anthracene; b) pentacene; c) heptacene; and d) nonacene

As the number of carbon rings increase, it is expected that their properties should become more graphene-like. As such, through modelling the Raman spectra of these materials, it is expected that the D mode will become less intense as the length of the fragment increases, due to the prominence of the zig-zag edge preventing the rings expanding.

(b) Armchair edged structures

The armchair edged linear structures studied were phenanthrene, picene, dibenzopicene, and dinaphthopicene. The structures of these compounds are shown in Figure 3.3. Comparing these structures with those zig-zag edged structures studied, a complementary armchair edged structure with the same number of carbon rings and atoms is studied also. This enables direct comparison of the effect of edge structure for a given number of carbon rings. For armchair structures, no significant changes in D mode intensity are expected, due to the rings being able to expand freely in these structures.

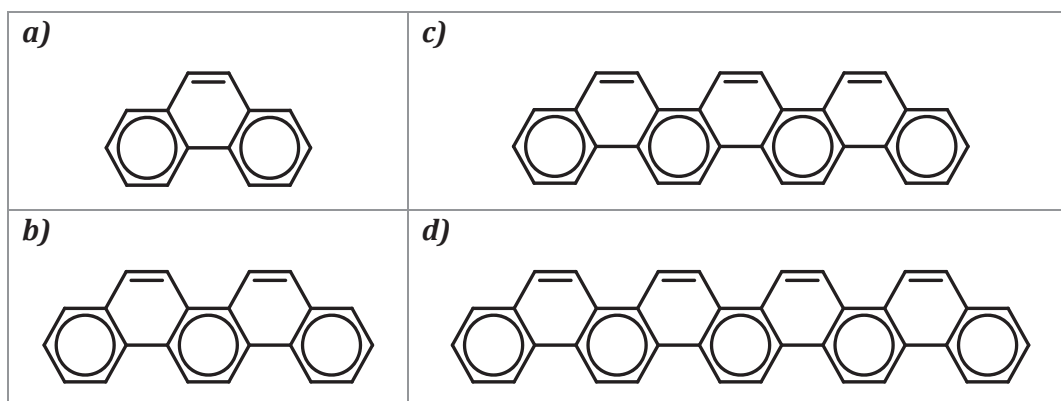


Figure 3.3 - Armchair edged structures: a) phenanthrene; b) picene; c) dibenzopicene; and d) dinaphthopicene

(c) Ring structures

Ring structures were studied in order to characterise the behaviour of breathing modes, such as the R mode described in (i). The ring structures studied were pyrene, coronene, ovalene, hexa-peri-benzocoronene, and tribenzo[jk,mn,pq]dibenzo[5,6:7,8]pentapheno[2,1,14,13,12-stuvabcd]ovalene, which will herein be referred to as TBDBPP-ovalene (Figure 3.4).

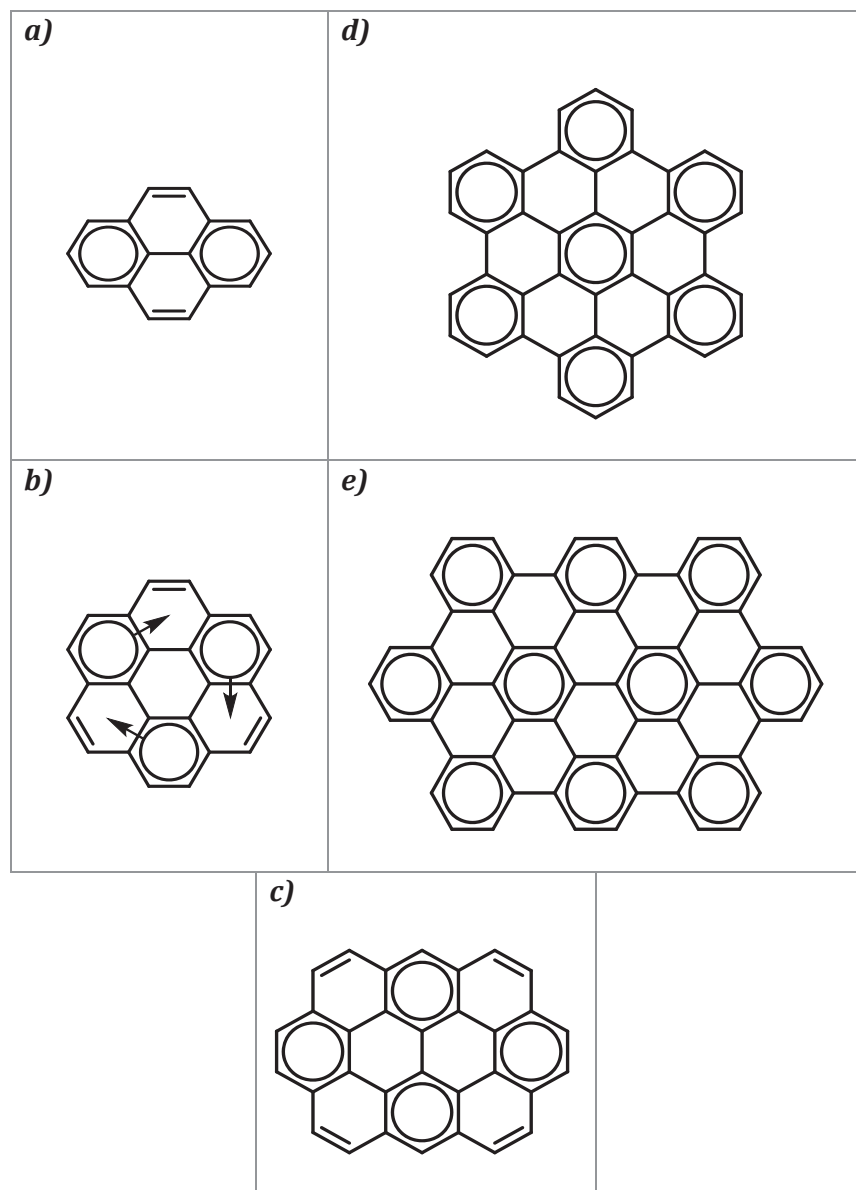


Figure 3.4 - Ring structures: a) pyrene; b) coronene; c) ovalene; d) hexa-*peri*-benzocoronene; and e) TBDBPP-ovalene

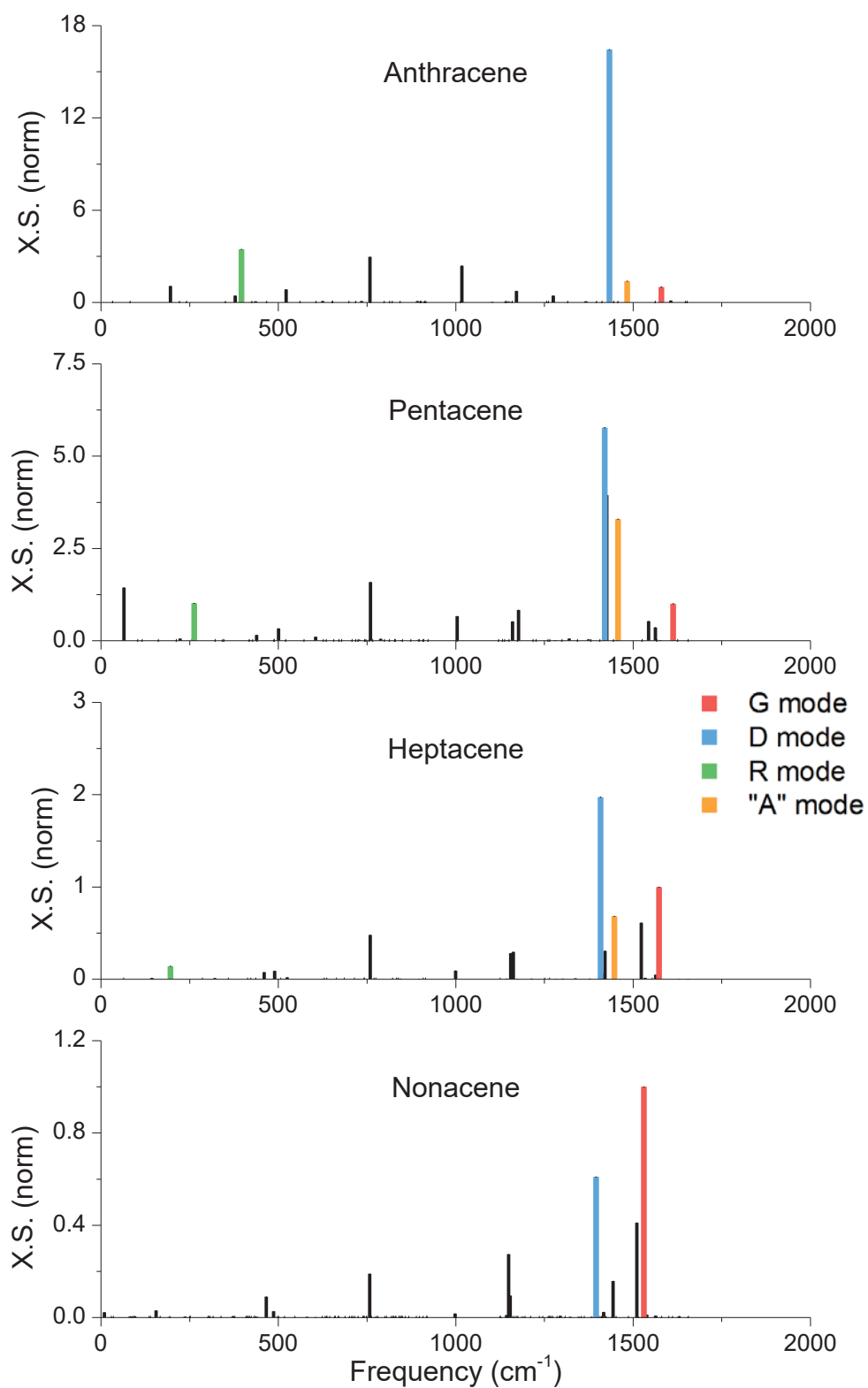


Figure 3.5 - Calculated Raman spectra of zig-zag structures

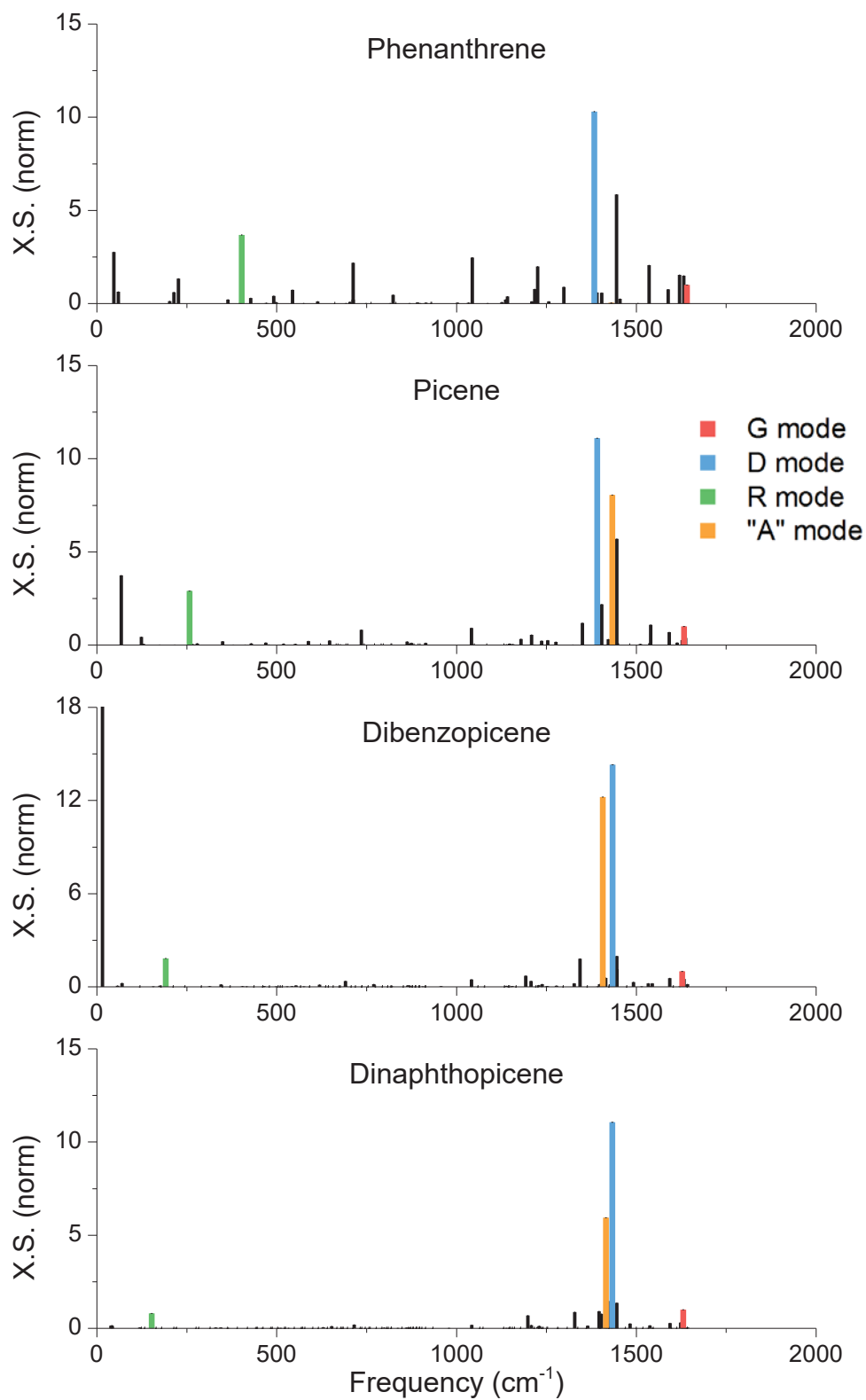


Figure 3.6 - Calculated Raman spectra of armchair structures

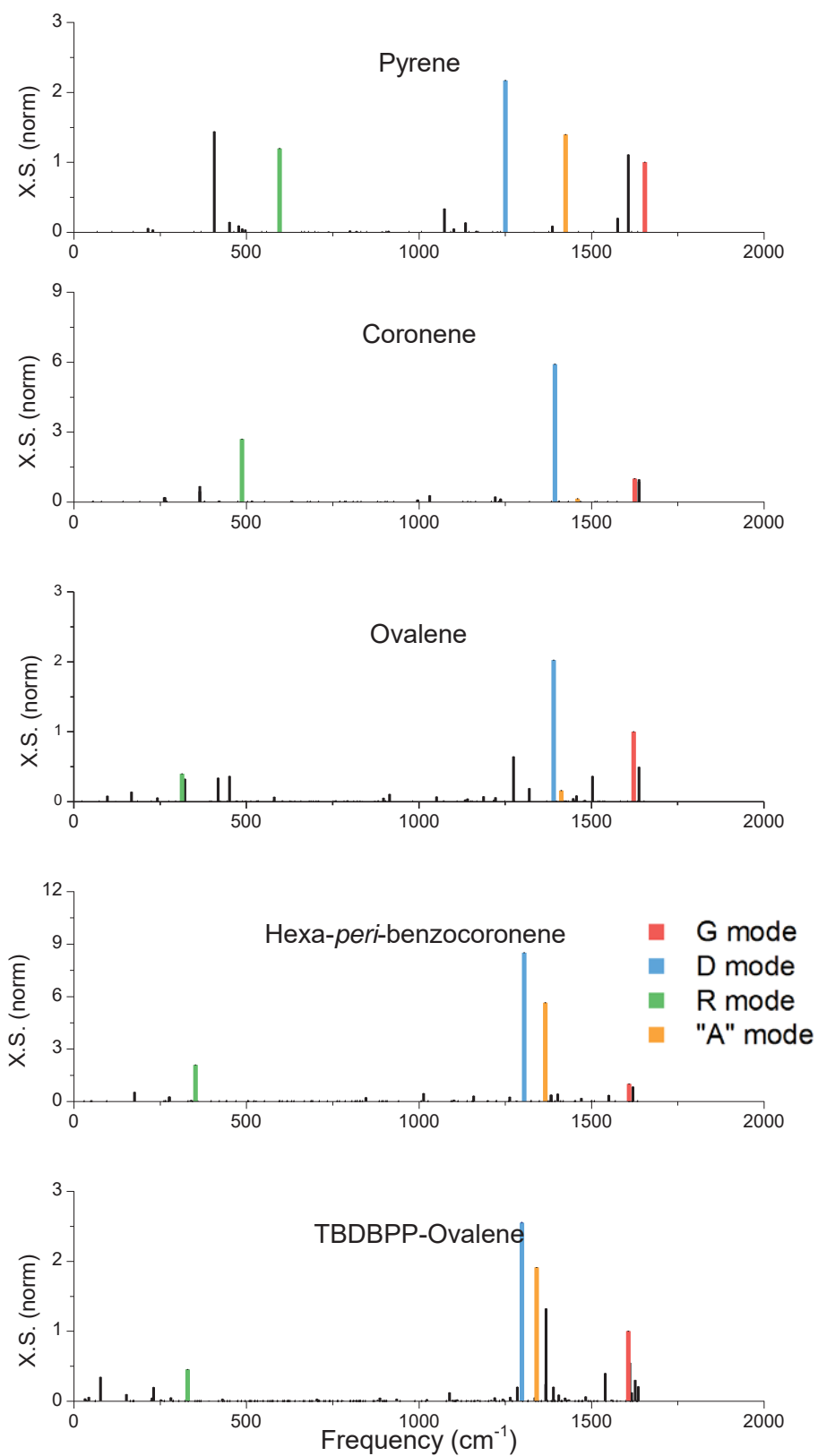


Figure 3.7 - Calculated Raman spectra of ring structures

3.1.2 Results and discussion

Geometry optimised structures are used in the calculation of vibrational frequencies and Raman spectra. Calculated Raman spectra are shown in Figure 3.5 to Figure 3.7.

Raman modes associated with the parent graphene structure (see 1.2.1(a)) have been assigned using a combined analysis of calculated atomic displacements and mode frequencies. The spectra have also been normalised so the G mode has a normalised differential cross-section equal to 1. Raman intensities have been converted from Raman activities to differential cross-sections (see Appendix B).

(a) *Zig-zag edged structures*

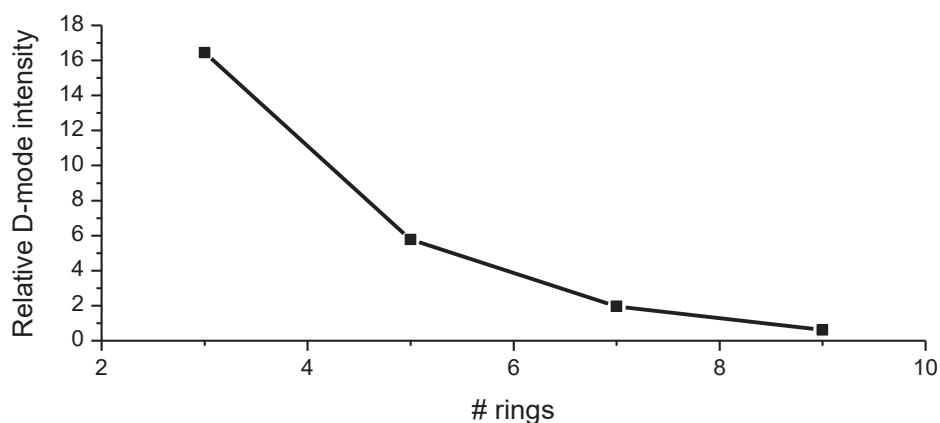


Figure 3.8 - Relative D mode intensity in calculated zig-zag Raman spectra

Figure 3.5 shows the intensity of the D mode in the zig-zag structure decreases significantly with increasing number of rings. This is further evident when this data is plotted, as shown in Figure 3.8. The decrease in D mode intensity (i.e. cross-section) is analogous to the decrease of D mode intensity in graphitic materials with zig-zag edge structure. The sharpness of this decrease to near-zero intensity with 9 rings indicates that small-scale models of graphene nanoribbons consisting of

greater than 9 rings along a single edge should effectively model this effect on D mode intensity. In terms of computational cost, this is advantageous.

(b) Armchair edged structures

As with the zig-zag data, armchair spectra shown in Figure 3.6 have been normalised to have a G mode differential cross-section equal to 1. Generally, it is evident that D mode cross-section does not change significantly with respect to the normalised G mode cross-section. This is as expected for modelling graphitic materials; as armchair edge-structure does not effect the D mode. A property which does change in intensity with respect to the G mode with increasing number of rings, however, is the relative R mode intensity (Figure 3.9). As chain length increases, this mode becomes dominated by the intensity of the D and G modes, and tends linearly to zero.

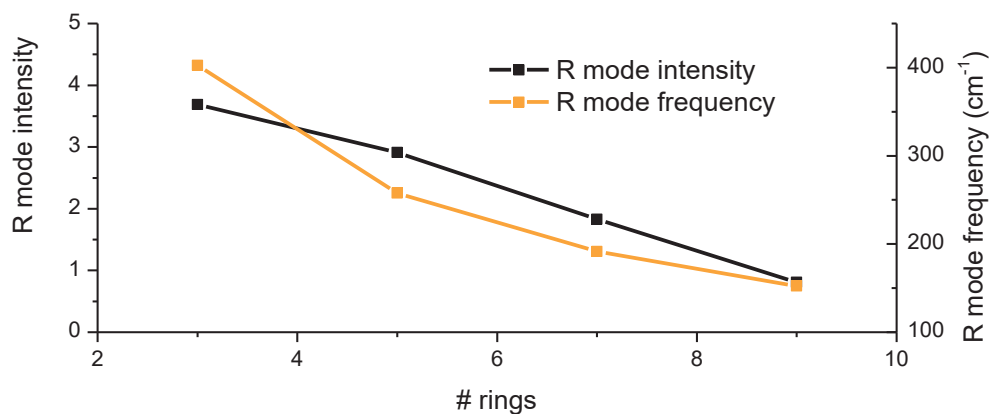


Figure 3.9 - Relative R mode intensity in calculated armchair Raman spectra

(c) Ring structures

Calculated Raman spectra for ring structures are shown in Figure 3.7. Pyrene, coronene, and ovalene spectra should be indicative of structures with zig-zag edges,

while those of hexa-*peri*-benzocoronene and TBDBPP-ovalene should be indicative of those with armchair edges.

For the zig-zag edged structures, the normalised D mode cross-section decreases significantly from coronene to ovalene, which is expected due to an increasing amount of zig-zag character. So although these structures are wider than the linear zig zag analogues they follow a similar trend. Additionally, there is a decrease in normalised cross-section and frequency of the R mode in these two ring structures.

These comparisons between coronene and ovalene cannot be extended easily to include pyrene, however, as its normalised D mode cross-section is small compared to that of coronene, and similar to that of ovalene. This may be due to pyrene not containing a central ring structure, and as such having a higher ratio of edge atoms to centre atoms, causing it to have a more graphene-like spectrum that its small size would suggest.

The armchair edged ring structures show a larger decrease in D mode intensity with increasing size than expected. This is due to hexa-*peri*-benzocoronene having two G-like modes of similar frequency and intensity which would more likely sum together, whereas in this case only one of these modes has been assigned as a G mode.

(i) Vibrational modes of ovalene and hexa-*peri*-benzocoronene

Comparing the vibrational modes of ovalene, a zig-zag edged analogue, with armchair edged hexa-*peri*-benzocoronene demonstrates the differences between the armchair and zig-zag edges of graphene structures.

Looking at the R modes for both structures, it is evident from Figure 3.10 that the rings in hexa-*peri*-benzocoronene are freely breathing symmetrically, radiating from the central ring. In contrast, the displacement vectors for ovalene demonstrate asymmetric motion which appears to be restricted due to the zig-zag edges, with the stretching only occurring towards armchair regions of the edges.

The D and A modes for both ovalene and hexa-*peri*-benzocoronene are similar, showing isolated rings stretching in the D modes, and the other rings stretching in the A mode.

The G mode is, as expected, more defined and more intense in ovalene in contrast to hexa-*peri*-benzocoronene due to the zig-zag edges of ovalene allowing a more uniform motion in comparison with the armchair edges of hexa-*peri*-benzocoronene. This is analogous to the behaviour observed in graphene nanoribbons, further confirming that small analogues such as these are good models for DFT calculations of graphene nanoribbons.

3.1.3 Analysis of models

As would be expected from any computational model, as analogue size increases towards that of a true graphene nanoribbon the calculations show better agreement with experimental data. The calculations on small analogues performed here show small graphene-like fragments consisting of 60 or less carbon atoms can be used to accurately model properties of graphene, which consists of many thousands of carbon atoms. This is highly advantageous in terms of computational ease and in obtaining accurate results in a timely manner.

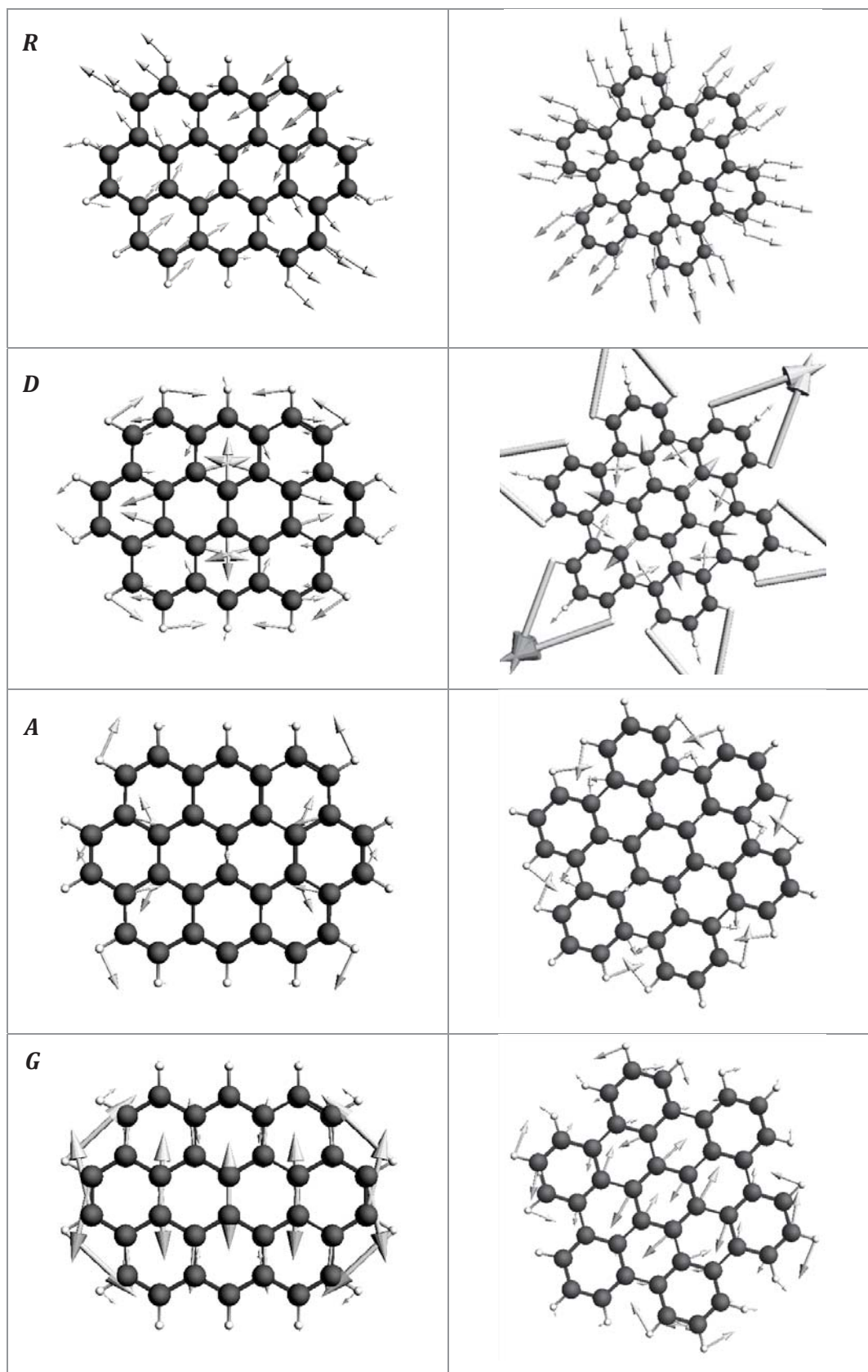


Figure 3.10 - Vibrational modes of ovalene (left) and hexa-*peri*-benzocoronene (right)

3.2 Graphene nanoribbon studies

In general, the choice of basis set and functional can have an effect on the accuracy of results. As such, potential basis sets and functionals were researched to obtain the best choice. Tommasini *et al*⁶⁷ found that a simplified Hückel model gave very good correlation with results obtained using DFT methods, as shown in Figure 3.11.

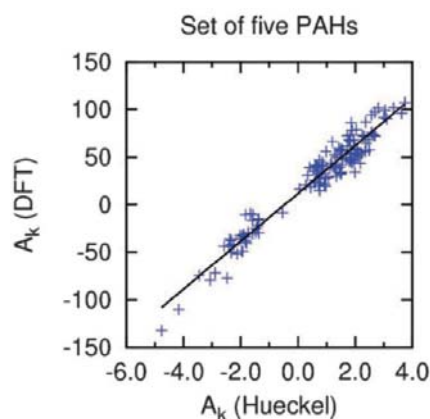


Figure 3.11 - Comparison of Raman bond parameters for graphene fragments using Hückel and DFT methods; good agreement is observed between low and high levels of theory (Reproduced from Ref. 67 with permission from the PCCP Owner Societies)

In consequence of the results of Tommasini *et al*, it was decided to perform calculations on model graphene nanoribbons using the LDA functional with a DZP basis set. The use of LDA/DZP minimises computational time compared with other DFT methods. In choosing this method, it was assumed there would be no loss of accuracy compared with a larger functional or basis set.

3.2.1 Graphene nanoribbon structures

For nanoribbon studies, small (150 atom) ribbons were studied in order to minimise computation time. Based on results from 3.1, it is assumed these small ribbons should act as suitable analogues for a true graphene nanoribbon, calculations on which would be prohibitive computationally.

Two ribbons, one armchair and one zig-zag edged, were studied, the structures of which are shown in Figure 3.12. These structures have been shown in a skeletal form with no explicit double bonds stated as calculations were performed with all C-C bonds having a bond order of 1.5 (i.e. one and a half bonds) for the aromatic system. Hydrogen atoms were bonded to all edge carbon atoms to give a formula of $C_{150}H_{44}$ for both structures.

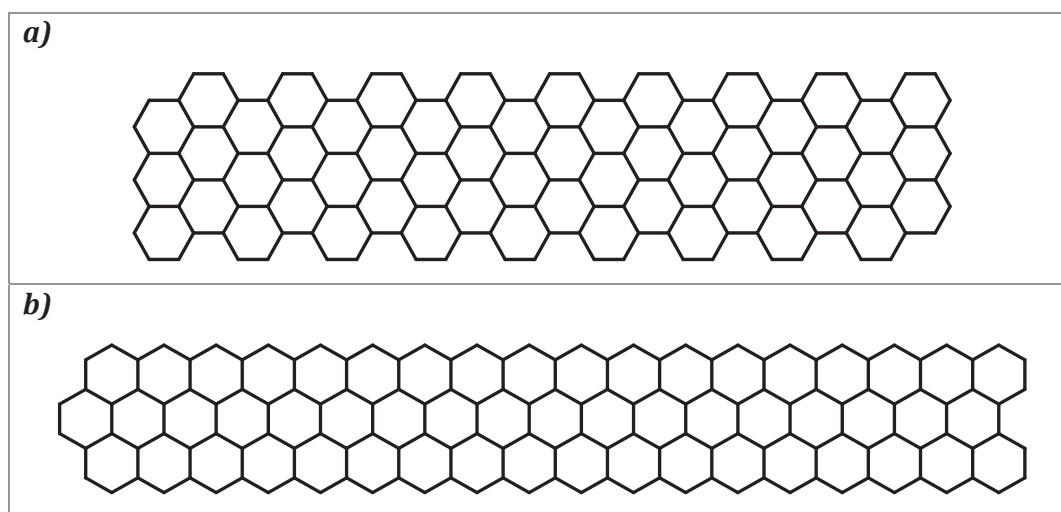


Figure 3.12 - Skeletal structures of a) armchair and b) zig-zag edged nanoribbon analogues

Both geometry optimisations and frequency calculations were carried out using LDA/DZP. Raman spectra were not calculated for these structures due to the computational time cost being large.

3.2.2 Discussion of results

Calculated IR spectra were obtained for both nanoribbon analogues. Vibrational frequencies were scaled as DFT methods are known to give systematic errors for vibrational frequency calculations (scaling factor for LDA/DZP = 0.981). Following scaling, the two calculated spectra were compared, as shown in Figure 3.13. Whilst every vibrational mode has been plotted, it is fairly difficult to make comparisons between the data at most points, with the exception of the large contributions to the

zig-zag analogue IR spectrum around 1500 cm^{-1} . As such, it was decided to also plot the data in an artificially widened form (applying Lorentzian functions with widths of 20 cm^{-1} to each data point) to see more trends. This data is shown in Figure 3.14.

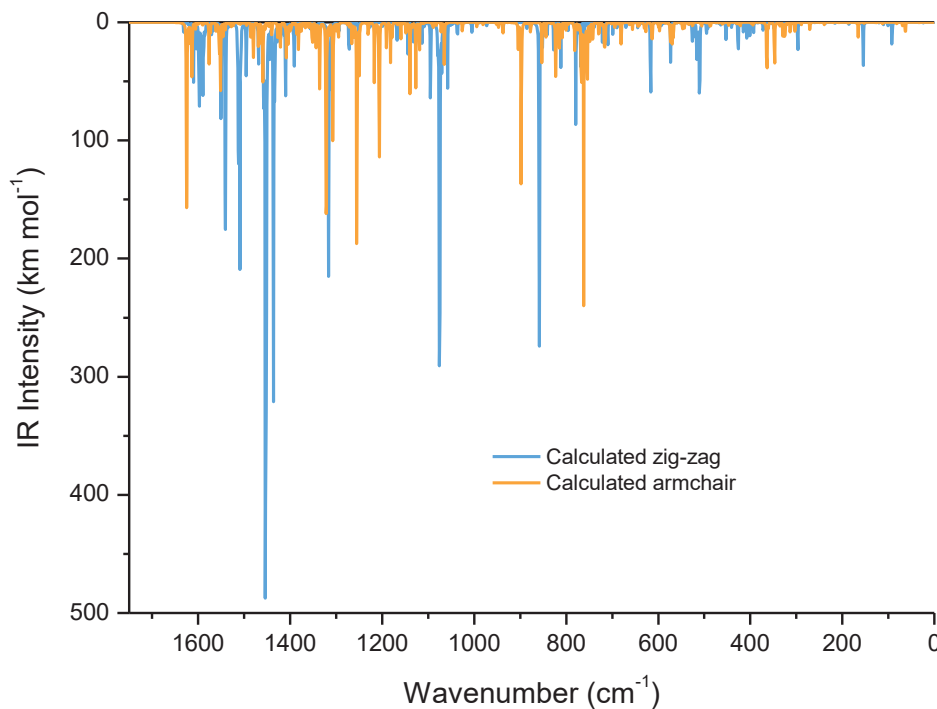


Figure 3.13 - Calculated IR spectra for armchair and zig-zag nanoribbon analogues (individual points plotted)

In the artificially widened spectrum, there are modes common to both armchair and zig-zag nanoribbons at approximately 1300 cm^{-1} and around 1600 cm^{-1} . There are also distinct armchair IR modes at approximately 300 cm^{-1} and 1200 cm^{-1} . In Figure 3.15 the graphene nanoribbon sample analysed contains a mixture of modes which can be assigned to either zig-zag or armchair nanoribbon edge structure. From mode assignments, this sample appears to consist of a higher proportion of zig-zag character, indicating that the sample consists mostly of zig-zag nanoribbons, with a small amount of armchair edged ribbons present, possibly due to defects in the HOPG block during cutting.⁶

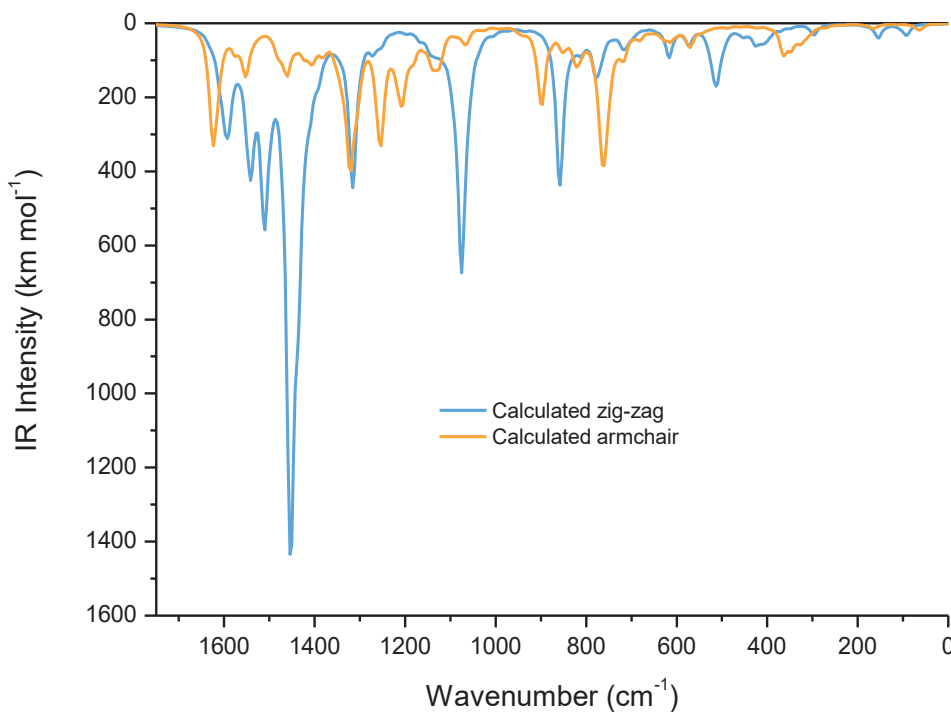


Figure 3.14 - Calculated IR spectra for armchair and zig-zag nanoribbon analogues (artificially widened)

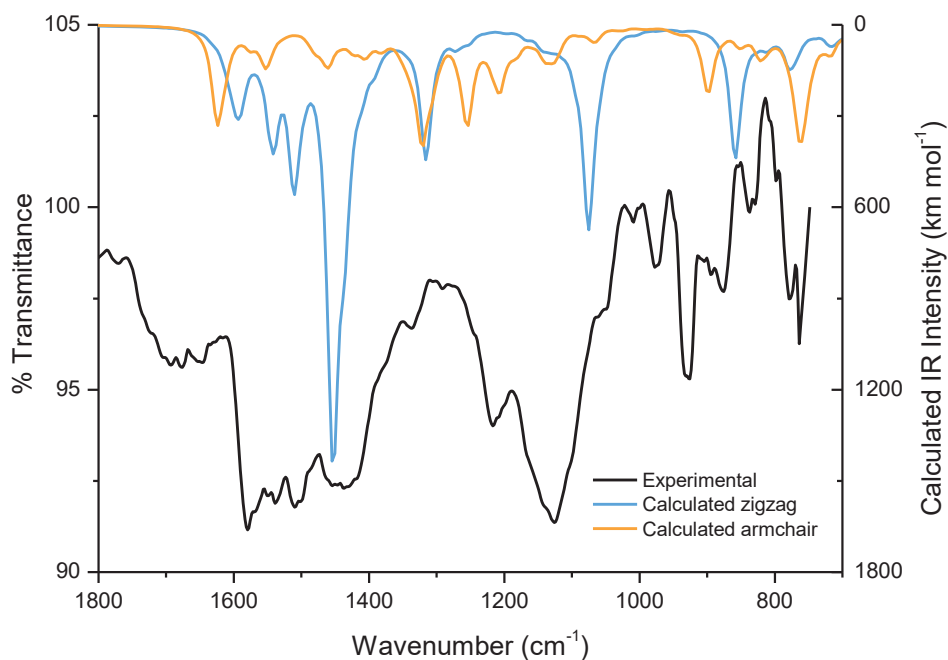


Figure 3.15 - Calculated and experimental IR spectra for graphene nanoribbons. The nanoribbons studied experimentally likely have edges which have not been cleanly fractured, evidenced by the large number of IR active modes

3.3 Functionalisation studies

In order to understand the mechanism of substitution of Cl-BODIPY, computational studies were performed on Cl-BODIPY and all synthetically functionalised analogues (see 2.2). This was done to further understand conditions required for reaction with graphene. Whilst literature indicates the substitution mechanism would appear relatively straight-forward, experimental results (see 2.2) showed unexpected results, such as double substitution and substitution in locations other than those expected. It is hoped that computational studies may assist in the explanation of these results.

The determination of appropriate basis set and functional, and results corresponding to the substitution mechanism, are discussed here, whilst additional results from these calculations, such as calculated spectroscopic information, will be discussed in 4.4.

Due to BODIPY-functionalised analogues having more complex geometries than the graphene analogues studied in 3.1, the choice of functional is expected to make a greater difference to the quality of optimised geometries. As such, it was decided to investigate a range of different functionals. Previous studies of BODIPY-functionalised compounds have utilised the B3LYP functional,^{54-55, 59} so it is expected that this functional should provide good results. In addition, the PBE, MO6 (Minnesota 06), and MO6-2X (Minnesota 06 – additional Hartree-Fock exchange) functionals were also analysed.

To determine the quality of the models, geometry optimisations were performed for two compounds for which crystallographic data was available (see 2.2) and the optimised geometries compared to these in terms of calculated

structure and energies. All calculations utilise a DZP basis set for consistency and computational cost efficiency.

The crystal structures analysed are shown in Figure 3.16. The crystal structure for 1-naphthylamine/BODIPY consists of 4 different orientations of the bridging bond, with two orientations (i.e. 1 and 2) being effectively analogous to the others (i.e. 3 and 4) in terms of orientation and energy, with the lowest energy structure being shown here.

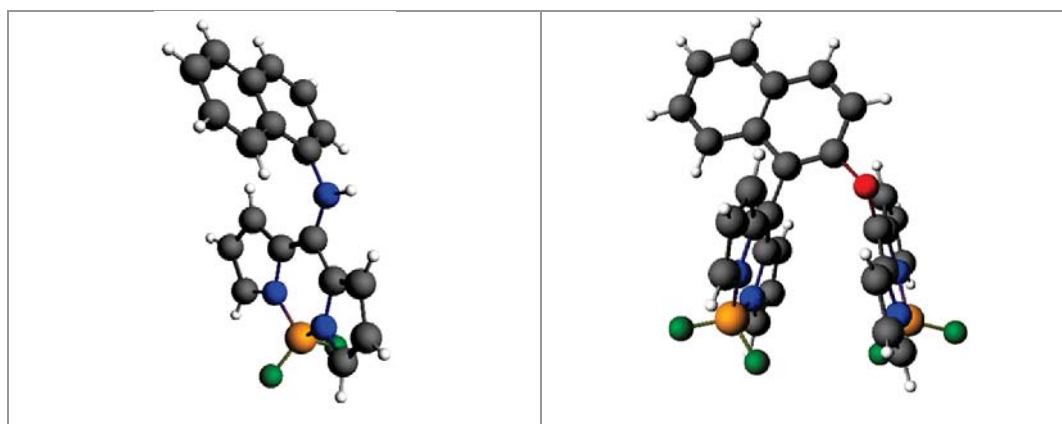


Figure 3.16 - Crystal structures for basis set optimisation; left: 1-naphthylamine/BODIPY; right: 2-naphthol/2xBODIPY

The optimised geometries calculated using different basis sets are shown in Figure 3.17 for 1-naphthylamine/BODIPY, while those for 2-naphthol/2xBODIPY are shown in Figure 3.18.

Looking at the optimised structures for 1-naphthylamine BODIPY, the optimised structures for B3LYP, MO6, and MO6-2X are all very similar to the crystal structure, whereas the structure calculated using PBE has a larger twist around the NH group causing the aromatic part of the structure to appear more out of plane. In addition to obtaining bonding energies for optimised geometries, single point calculations were performed on the crystal structure using each functional in order to remove

any functional effects on single point energy calculation. These calculated energies are shown in Table 3.1. It can be seen through comparing these energies through % error that B3LYP and MO6 provide similarly accurate results, with MO6-2X being slightly better, and PBE being less accurate.

Computational time cost is also an important consideration. Considering geometry optimisations only, starting from the same initial geometry, PBE calculations were the fastest, taking 87 minutes to converge. B3LYP calculations took 337 minutes, whereas MO6 took 834 minutes, and MO6-2X took 568 minutes.

Taking into account accuracy of calculations and computational time cost, it is evident that either B3LYP or MO6-2X functional should be used to obtain the most accurate results in a reasonable time frame.

The same analysis was also performed for the crystal structure and optimised geometries of 2-naphthol/2xBODIPY. This was done to determine whether double functionalisation had any effect on which functional is optimal for calculations. The optimised geometries are shown in Figure 3.18. For this structure, six optimised geometries have been obtained. This is due to initial B3LYP and PBE functionals converging on a different minimum geometry in which the two BODIPY units were perpendicular to each other, compared to being near-parallel with each other in the crystal structure. To overcome this issue, additional B3LYP and PBE calculations were performed, this time starting from the optimised MO6-2X geometry. The four structures which contain parallel BODIPY units are all very similar to the crystal structure. Comparison of bonding energies (Table 3.2) show again that B3LYP, MO6, and MO6-2X are superior to PBE in terms of energy calculations.

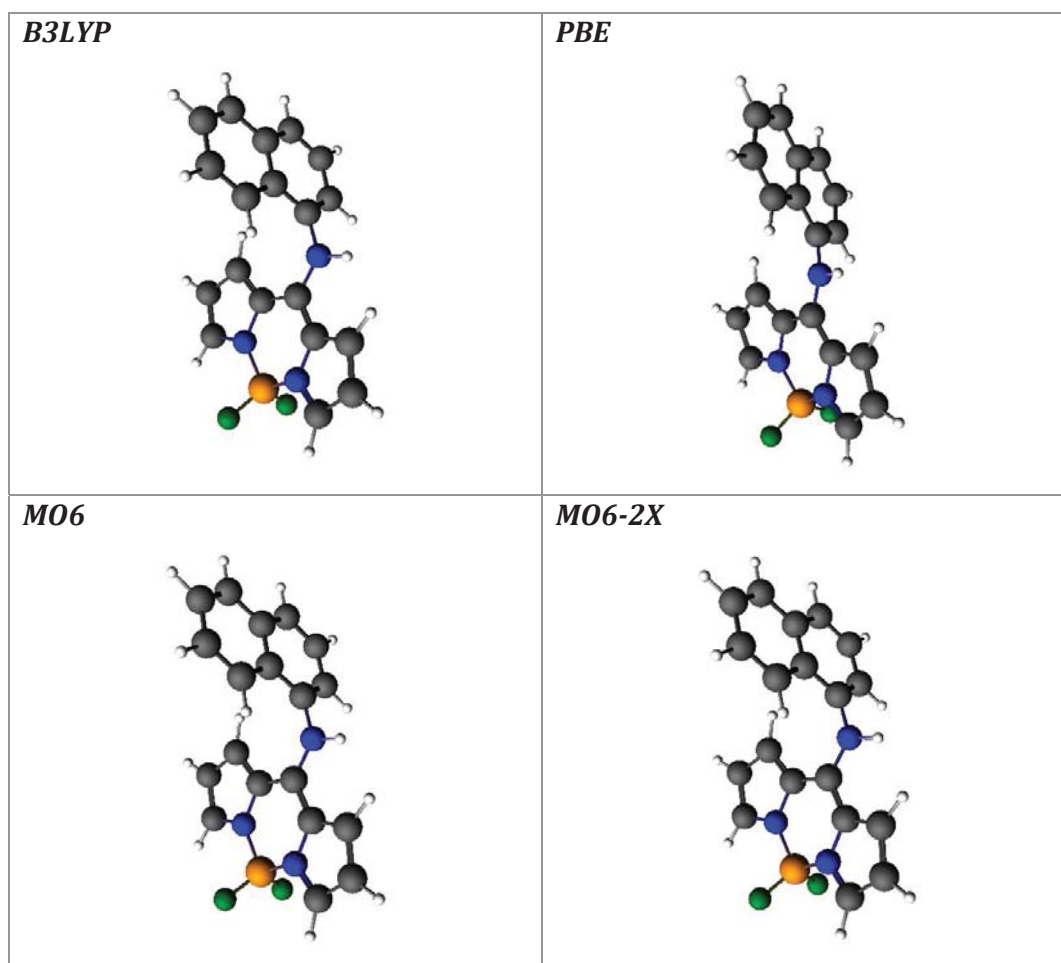


Figure 3.17 - Optimised geometries of 1-naphthylamine/BODIPY

Table 3.1 - Bonding energies for 1-naphthylamine

	Crystal structure kJ mol ⁻¹	Optimised geometry kJ mol ⁻¹	Difference %
B3LYP	-27939	-28639	2.5
PBE	-24543	-25313	3.1
M06	-29398	-30103	2.4
M06-2X	-33980	-34696	2.1

Looking at computational time cost, the results are similar to those for the 1-naphthylamine/BODIPY structure, with PBE being fastest and MO6 the slowest. It is important to note that the PBE and B3LYP calculations from MO6-2X optimised geometry were not from the same initial geometry and those for MO6 and MO6-2X, however, this could have been prevented by use of a starting geometry for initial PBE and B3LYP calculations which more resembled the crystal structure more closely. The choice of a more reasonable starting geometry would also have effected the computational time for MO6 and MO6-2X calculations, however, it would not have improved the time cost enough for MO6 to be considered a good functional.

Table 3.2 - Bonding energies for 2-naphthol/2xBODIPY

	Crystal structure	Optimised geometry	Difference
	kJ mol⁻¹	kJ mol⁻¹	%
B3LYP	-41889	-42572	1.6
PBE	-36766	-37530	2.1
MO6	-44174	-44882	1.6
MO6-2X	-51149	-51882	1.4
B3LYP from MO6-2X	-41889	-42580	1.6
PBE from MO6-2X	-36766	-37544	2.1

After comparing computational results and crystallographic data for both structures, and taking into account computational time cost, it was decided the best functional for geometry optimisations of dipyrin-based structures is B3LYP, and that frequency calculations would be performed using PBE/DZP, as discussed in 3.1.

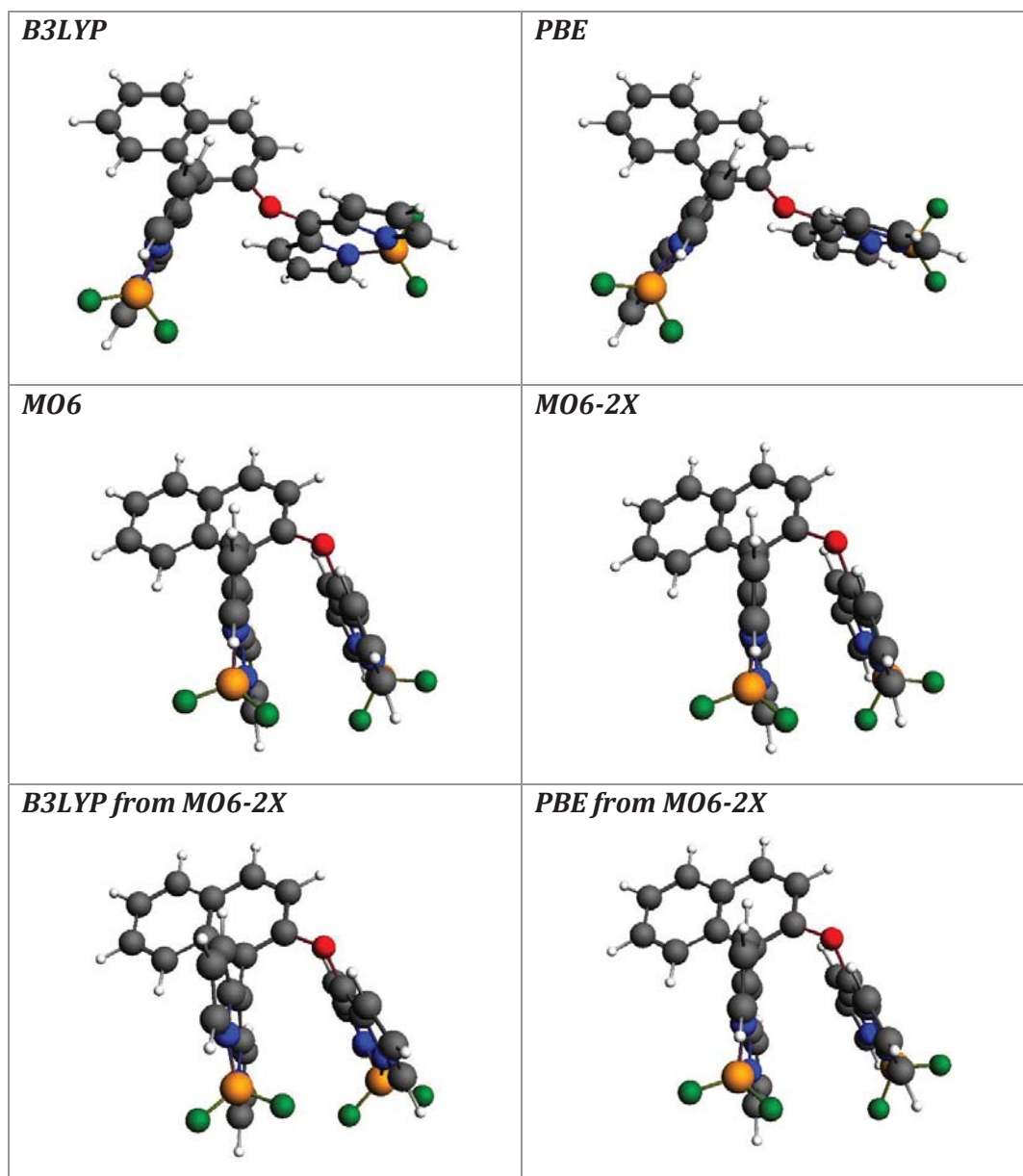


Figure 3.18 - Optimised geometries of 2-naphthol/2xBODIPY

3.4 Reaction mechanism study

BODIPY functionalisation occurs at the *meso* position via nucleophilic aromatic substitution (S_NAr via addition-elimination).⁴⁹ This explains the experimentally observed reactivity, however, there were also cases in which unexpected reactivity was observed, as in the double-substitution of 1-naph-OH/2xBODIPY and 2-naph-OH/2xBODIPY. This suggests another mechanism may be occurring. To further investigate this, and to find the transition state geometry, linear transit calculations were performed. Initially, calculations were performed on the expected reaction between phenol and Cl-BODIPY to test the computational model before expanding the method to direct C-C bond formation.

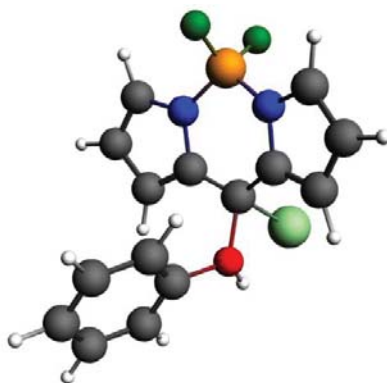


Figure 3.19 - Transition state geometry of Phenol/BODIPY

The linear transit calculation successfully demonstrated the reaction occurring via a concerted nucleophilic attack by phenolic-OH on the positive *meso*-carbon of BODIPY. These calculations also provided a reasonable transition state, shown in Figure 3.19, which was further refined by additional linear transit calculations with small step size, the energy profiles of which are shown in Figure 3.20. The transition state is confirmed by being located at a saddle point on the potential energy surface (Figure 3.20), and having a single imaginary vibrational frequency,⁸⁸ as shown in Figure 3.21. This imaginary frequency corresponds to O-C-Cl bond

formation/breaking of the transition state, further confirming the structure in Figure 3.19 as the transition state geometry.

Following on from the successful calculation of the Phenol/BODIPY transition state, further calculations were performed to investigate the transition state for the reaction of BODIPY with phenanthrene to obtain further information on the formation of analogues functionalised via C-C bond to BODIPY. Unfortunately, a transition state was not able to be determined for this calculation, and as such no further information on the reaction could be obtained using this method. The pKa of these aromatic carbons (see 3.4.1 below) indicates that they are not easily deprotonated. It is therefore likely that some intermediate reaction must occur for the double substitution to take place. The resonance structure of naphthol leads to those carbons which are ortho and para to the hydroxyl group being electron rich. This gives three electron rich sites, including the hydroxyl group, for the electron poor *meso*-carbon on the BODIPY to react with. Providing there is favourable alignment of the pyrrole rings of BODIPY with naphthol due to π - π alignment, it is possible for multiple substitution to occur.

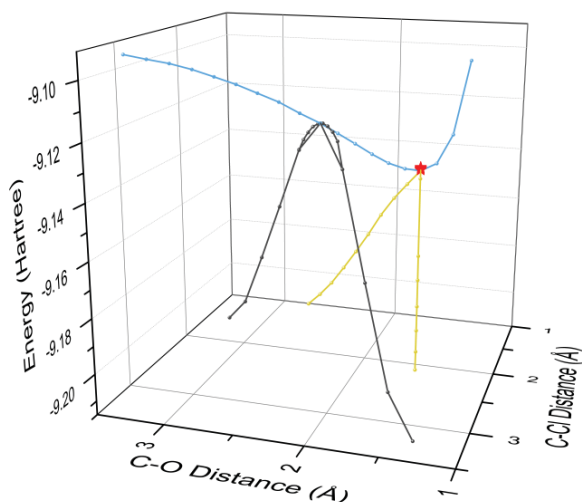


Figure 3.20 - Energy profile created from linear transit calculations; red star indicates transition state geometry

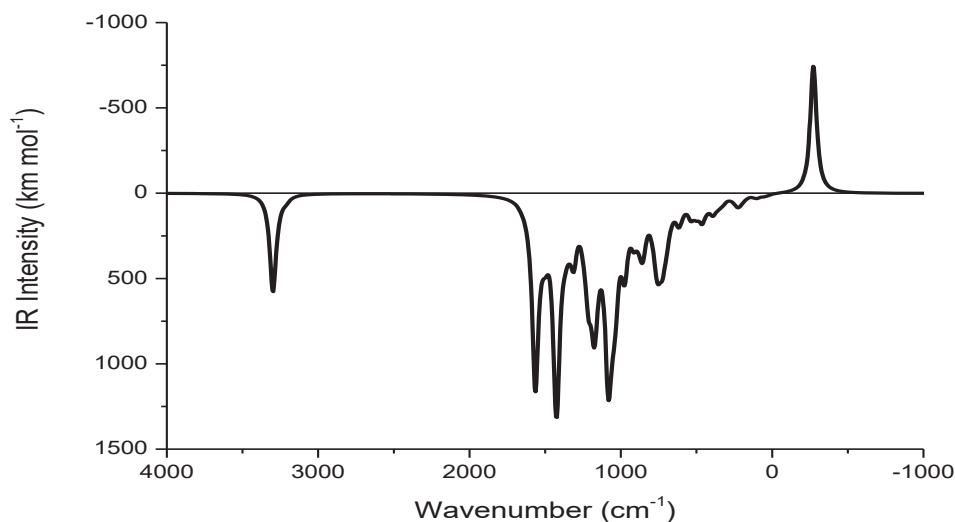
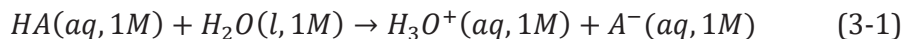


Figure 3.21 - Calculated IR spectrum for transition state geometry

3.4.1 Calculation of pKa values

For the observed double-substitution to occur, the C-H bond on the naphthalene ring must break. pKa is a good measure to approximate the tendency for bond dissociation.⁸⁹ As experimental pKa values are not available for many of the analogue structures studied, calculated pKa values were obtained to provide insight of ease of deprotonation of the analogues. These calculations were performed via an empirical pKa calculation method with a continuum solvent model using the COSMO-RS (Conductor like Screening Model) package within ADF, which provides reasonable approximations to experimental values.⁹⁰⁻⁹¹

As all analogues are acting as acids in this reaction, i.e. they lose a proton, only calculations for the acid case will be described here.



For (3-1) the pKa can be calculated according to (3-2), which has been optimised for the ADF COSMO-RS implementation, and where ΔG_{diss}^* is given by (3-3).

$$pKa = \frac{0.62\Delta G_{diss}^*}{RT \ln 10} + 2.10 \quad (3-2)$$

$$\Delta G_{diss}^* = G(A^-) - G(HA) + G(H_3O^+) - G(H_2O) \quad (3-3)$$

At T = 298.15 K, $(RT \ln 10)^{-1} = 0.733 \text{ mol kcal}^{-1}$.

Optimised geometry optimisations were performed using a B3LYP functional and ADZP (double-zeta, 1 polarisation function, diffuse) basis set on all analogues in their neutral and acidic forms. These optimised geometries are then used as the basis for a “COSMO-RS Compound” calculation using a BP (Becke, Perdew) functional and TZP (triple-zeta, 1 polarisation function) basis set. The output files for these calculations, along with solvent and its corresponding acidic form (i.e. H₃O⁺ for water) are then used in COSMO-RS, whereupon obtained Gibbs Free Energy values can be used to calculate pKa values according to (3-2) and (3-3).

Initially, calculations were performed on a range of structures for which experimental pKa values were available to determine the accuracy of the method. These calculations were performed with a water solvent to match the conditions of the experimental pKa measurements. The results are shown in Table 3.3.

Table 3.3 - Comparison of experimental and calculated pKa values

	Experimental pKa	Calculated pKa
Methane	48	46.5
Benzene	43	40.2
Cyclopentadiene	16	18.2
Methanol	15	16.3
Phenol	10	10.0

It can be seen that all the pKa values agree to within 2 units, which is comparable to literature methods.⁹⁰⁻⁹¹

As BODIPY-functionalisation reactions are performed in dichloromethane (DCM), pKa values are also calculated for dichloroethane (DCE). Experimental pKa values are more widely reported for DCE compared to DCM, with pKa values for DCE being reported relative to picric acid pKa = 0.00. In addition, most of these experimental values are reported for superacids, and therefore the dataset was expanded accordingly for both DCE and water. By expanding the dataset, it is possible to compute new scaling factors, by plotting pKa against $\Delta G_{diss}^*/RT \ln 10$. and therefore new equations for pKa in both water and dichloroethane, shown in (3-4) and (3-5) respectively.

$$\text{Water : } pKa = \frac{0.69\Delta G_{diss}^*}{RT \ln 10} - 0.39 \quad (3-4)$$

$$\text{DCE: } pKa = \frac{0.91\Delta G_{diss}^*}{RT \ln 10} - 64.08 \quad (3-5)$$

The accuracy of the new models can be seen in Table 3.4 and Table 3.5. Overall, the agreement is better for pKa values calculated in water, although there is now more discrepancy between the experimental and calculated pKa values for phenol. The experimental and calculated pKa values in dichloroethane agree well with each other, with values agreeing to within 2 units. After confirming the new equations to be reasonable and that they provide good answers they were then used to calculate pKa values for analogues in both solvents as reported in Table 3.6.

Table 3.4 - Comparison of experimental and calculated pKa values in water

	Experimental pKa	Calculated pKa
2,4,6-trinitrophenol	0.4	0.2
Methane	48	48.7
Benzene	43	41.8
Cyclopentadiene	16	17.4
Methanol	15.3	15.3
Phenol	10	9.0

Table 3.5 - Comparison of experimental and calculated pKa values in dichloroethane

	Experimental pKa	Calculated pKa
2,4,6-trinitrophenol	0	1.9
Pentacyanophenol	-7.6	-6.7
Phenol	19.6	19.4
2-phenol-1,1,3,3-tetracyanopropene	-9.4	-11.5

Table 3.6 - Calculated pKa values for analogues

	pKa Water	pKa DCE
Phenol	9.0	19.4
1-naphthol	8.2	16.3
2-naphthol	8.6	17.8
1-naphthylamine	19.2	30.0
2-naphthylamine	18.9	31.2
1-aminoanthracene	15.3	24.2
2-aminoanthracene	18.6	29.5
9-aminophenanthrene	16.1	26.4
9-hydroxyphenanthrene	7.9	15.4
1-hydroxypyrene	8.2	14.4
2-hydroxytriphenylene	8.5	16.9

3.4.2 Thermodynamics

A range of information is available from the output files of both the geometry optimisations and frequency calculations performed in ADF. Appropriate output information will be discussed in the following section to highlight similarities and differences between the compounds, as well as some of their properties.

Thermodynamic properties can be calculated for individual structures, and subsequently for overall reactions, using information easily obtained from output files. The internal energy, U , is the summation of the nuclear “total bonding energy” obtained from geometry optimisations and the electronic “internal energy” obtained from frequency calculations. The enthalpy is then calculated according to (3-6), where $pV/n = RT$, and as such $pV = 2478.96 \text{ Jmol}^{-1}$ at 298.15 K.

$$H = U + pV \quad (3-6)$$

For each structure, entropy is obtained directly from the output file. Overall reaction thermodynamics are calculated according to equations (3-7), (3-8), and (3-9), and the values for the formation of BODIPY functionalisation reactions are shown in Table 3.7.

$$\Delta H = \sum H(\text{products}) - \sum H(\text{reactants}) \quad (3-7)$$

$$\Delta S = \sum S(\text{products}) - \sum S(\text{reactants}) \quad (3-8)$$

$$\Delta G = \Delta H - T\Delta S \quad (3-9)$$

All thermodynamic information is calculated for the formation of the BODIPY-functionalised analogues synthesised in 2.2. This thermodynamic information can be used to further understand differences between structures, as well as obtaining more information on the mechanism taking place.

For calculations of thermodynamic information for doubly-substituted analogues have assumed the reaction of two BODIPY molecules with one analogue, producing a single disubstituted product and two HCl molecules.

Table 3.7 - Thermodynamic information for functionalisation studies

	ΔH_f	ΔS_f	ΔG_f
	J mol ⁻¹	J mol ⁻¹ K ⁻¹	J mol ⁻¹
Phenol/BODIPY	-20941	-63.71	-1945
Aniline/BODIPY	-50932	-51.73	-35508
2-naphthol/1xBODIPY	-23815	-96.45	4941
1-naphthylamine/BODIPY	-61530	-100.76	-31487
2-naphthylamine/BODIPY	-52810	-83.63	-27876
1-aminoanthracene/BODIPY	-74965	-95.56	-46473
2-aminoanthracene/BODIPY	-53781	-89.91	-26973
9-aminophenanthrene/BODIPY	-72136	-63.33	-53255
9-hydroxyphenanthrene/BODIPY	-27259	-83.26	-2434
1-hydroxypyrene/BODIPY	-24916	-100.34	5001
2-hydroxytriphenylene/BODIPY	-23573	-106.35	8135
HBC(<i>t-Bu</i>)5OH/BODIPY	-41137	-96.44	-12383
HPB(<i>t-Bu</i>)5OH/BODIPY	-23623	-65.92	-3969
Benzoic/BODIPY	-7456	-92.83	20221
1-naphthol/2xBODIPY	-115077	-176.27	-62521
2-naphthol/2xBODIPY	-75634	-156.16	-29076
(1-naphthol/1xBODIPY)	-28573	-95.74	-27

(a) Comparison between bonding positions

The position of the functional group on the ring effects thermodynamic properties and BODIPY functionalisation. Within the calculations performed, there are three “pairs” of analogues which vary only by functional group position, i.e. 1- or 2-.

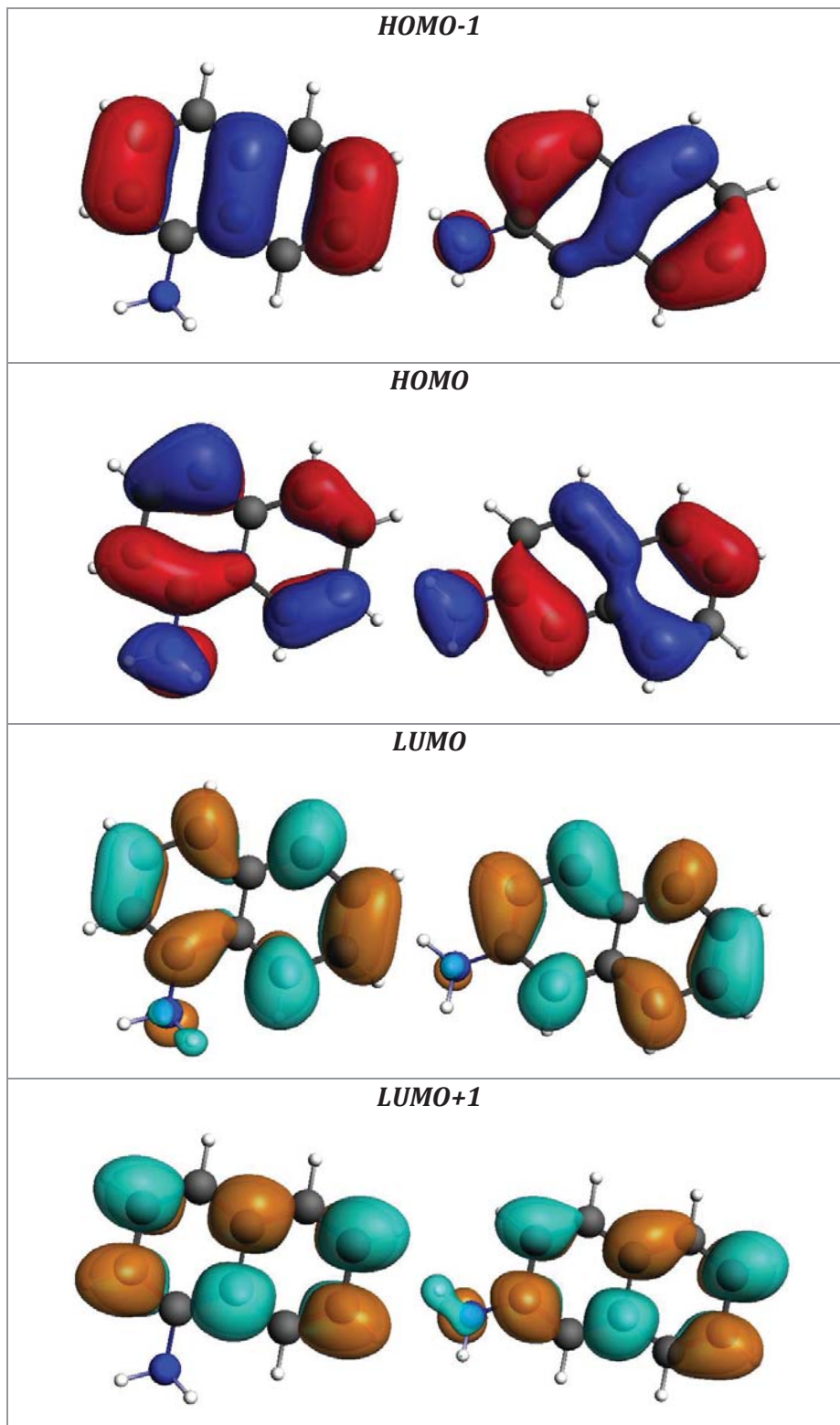


Figure 3.19 - Molecular orbital diagrams for 1-naphthylamine (left) and 2-naphthylamine (right)

Looking at the thermodynamic information shown in Table 3.7, the enthalpy of formation of 1-naphthylamine/BODIPY is 8720 J mol^{-1} larger than that for 2-naphthylamine, a difference equivalent to approximately $3 kT$ (where kT is equal to approximately 2.5 kJ mol^{-1} at 298 K). Similarly, ΔH_f for 1-naphthol/1xBODIPY is approximately $2 kT$ larger than for 2-naphthol/1xBODIPY, and 1-aminoanthracene/BODIPY approximately $8 kT$ larger than for 2-aminoanthracene/BODIPY. Overall, it can be said that functionalisation to functional groups in the 1- position have a larger enthalpy change than those in the 2- position. Additionally, ΔG_f scales similarly to this, with functionalisation to the 1- position more thermodynamically favoured than those to the 2- position.

Looking at the molecular orbitals 1-naphthylamine and 2-naphthylamine, shown in Figure 3.19, it is evident there is a node along the C-N bond in the HOMO and LUMO of both structures. In the HOMO-1 and LUMO+1 molecular orbitals, it can be seen that there is no density over the amine group for 1-naphthylamine, compared to significant density for 2-naphthylamine. Additionally, from the pKa values in Table 3.6 it is evident that the structures with functional groups in the 1- position have lower pKa's than those in 2- position. This indicates that structures with functional groups in the 2-position should react more readily with BODIPY.

(b) Comparisons between substitution group

Table 3.7 shows that the functional group through which reaction with BODIPY takes place has a significant effect on thermodynamic properties. Structurally, the only difference between phenol and aniline is the presence of a hydroxyl and an amine functional group respectively, however, phenol/BODIPY has a significantly smaller ΔH_f and ΔG_f of approximately $13 kT$ compared to aniline/BODIPY.

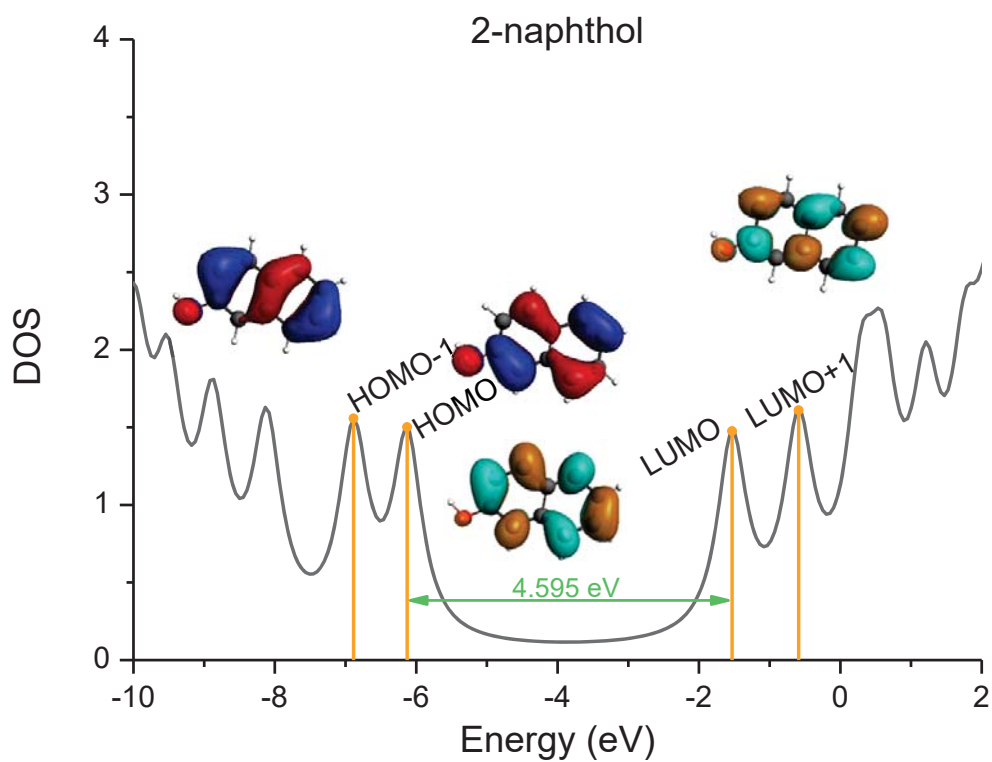


Figure 3.20 - Density of states for 2-naphthol with overlaid molecular orbitals

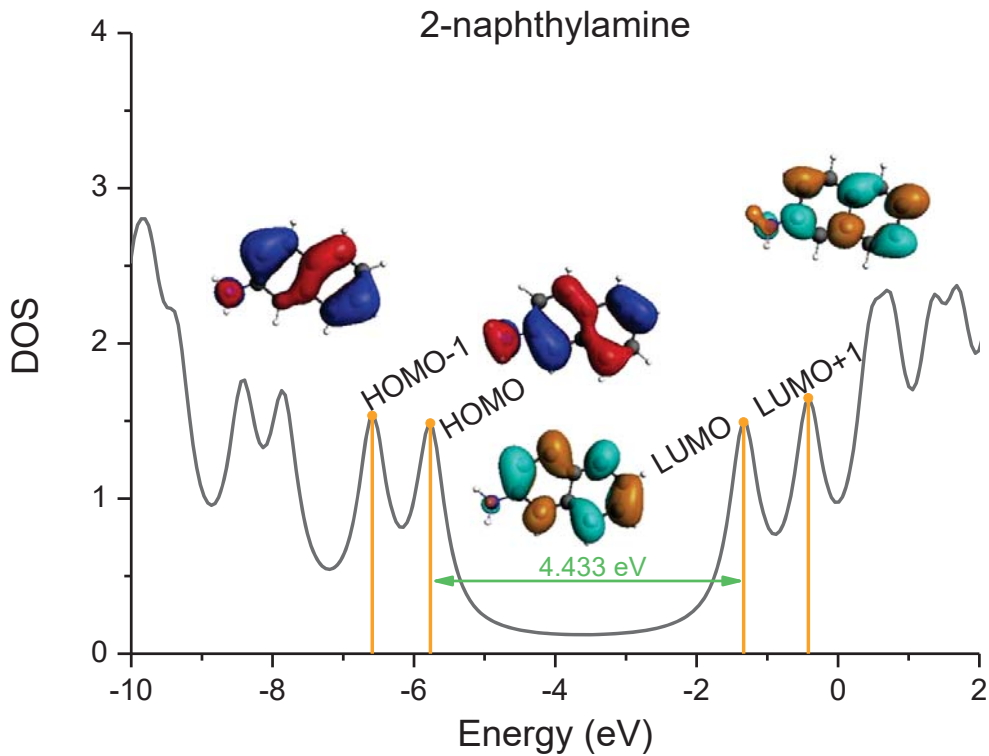


Figure 3.21 - Density of states for 2-naphthylamine with overlaid molecular orbitals

This same difference is apparent between the complementary pairs of: 1-naphthol/BODIPY and 1-naphthylamine/BODIPY; 2-naphthol/BODIPY and 2-naphthylamine/BODIPY; and 9-hydroxyphenanthrene/BODIPY and 9-aminophenanthrene/BODIPY. For all three cases, those with the hydroxyl functional group having significantly smaller ΔH_f and ΔG_f .

In general, it is expected that hydroxyl functionalities will have lower pKa values than amines. This is confirmed in the data shown in Table 3.6. The density of states for 2-naphthol and 2-naphthylamine are shown in Figure 3.20 and Figure 3.21 respectively. The two structures have very similar molecular orbitals and density of states, however, they have a difference in HOMO-LUMO gaps of approximately $6 kT$ due to the differing functional groups present.

(c) Multiple substitutions

The effect of double BODIPY functionalisation can be seen through the comparison of the monosubstituted and disubstituted products formed with both 1-naphthol and 2-naphthol. Both disubstituted structures have significantly larger ΔH_f and ΔG_f than the monosubstituted, and thus become more thermodynamically favourable.

(d) Changing size of analogue

Changing the size of the analogue has a significant effect on the HOMO, with the density moving from BODIPY onto the aromatic structure for some compounds as shown in Figure 3.22. This effect is not seen on the LUMO, which is maintained on the BODIPY for all structures (Figure 3.23).

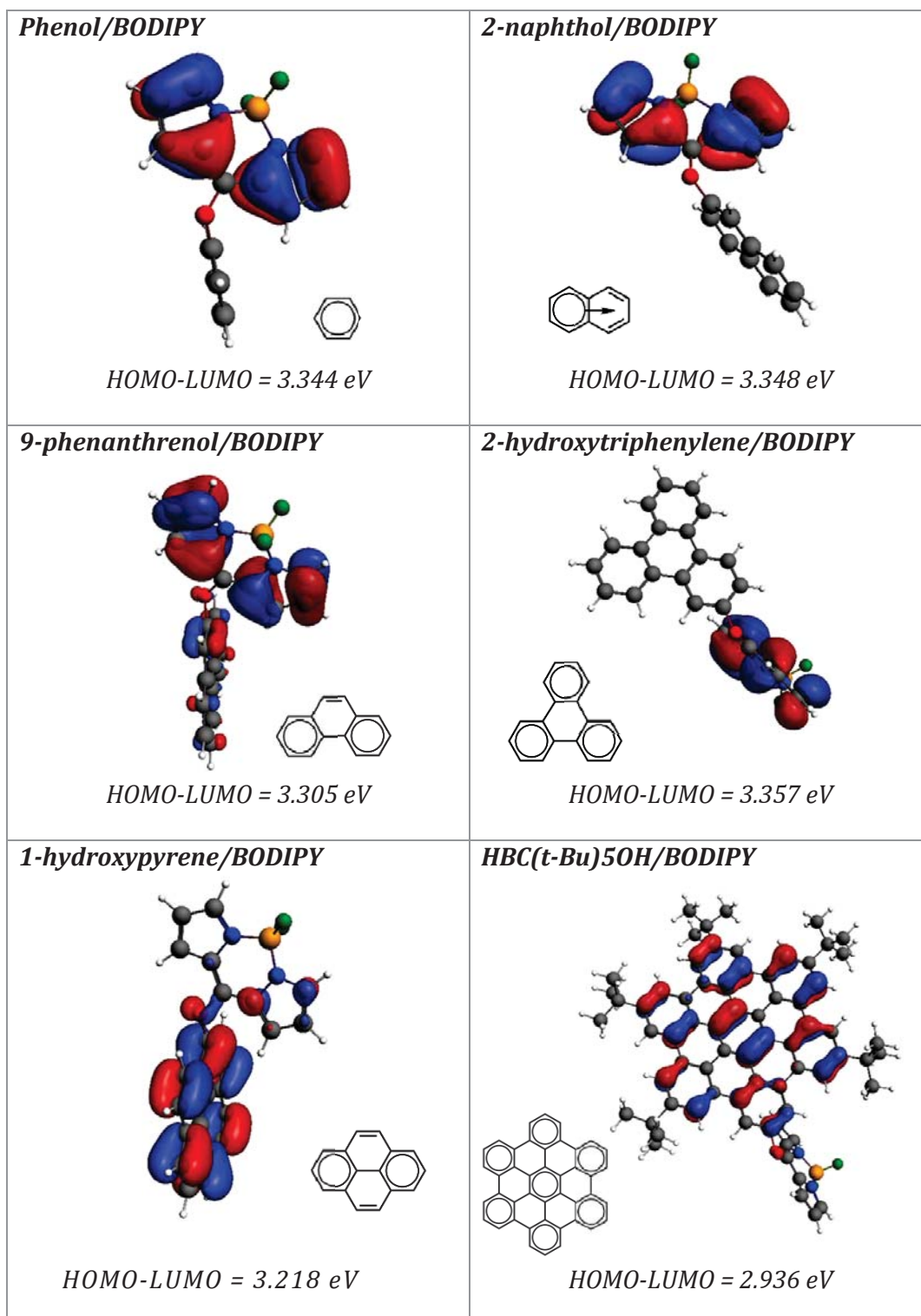


Figure 3.22 - HOMO for -O-BODIPY compounds with HOMO-LUMO gap stated

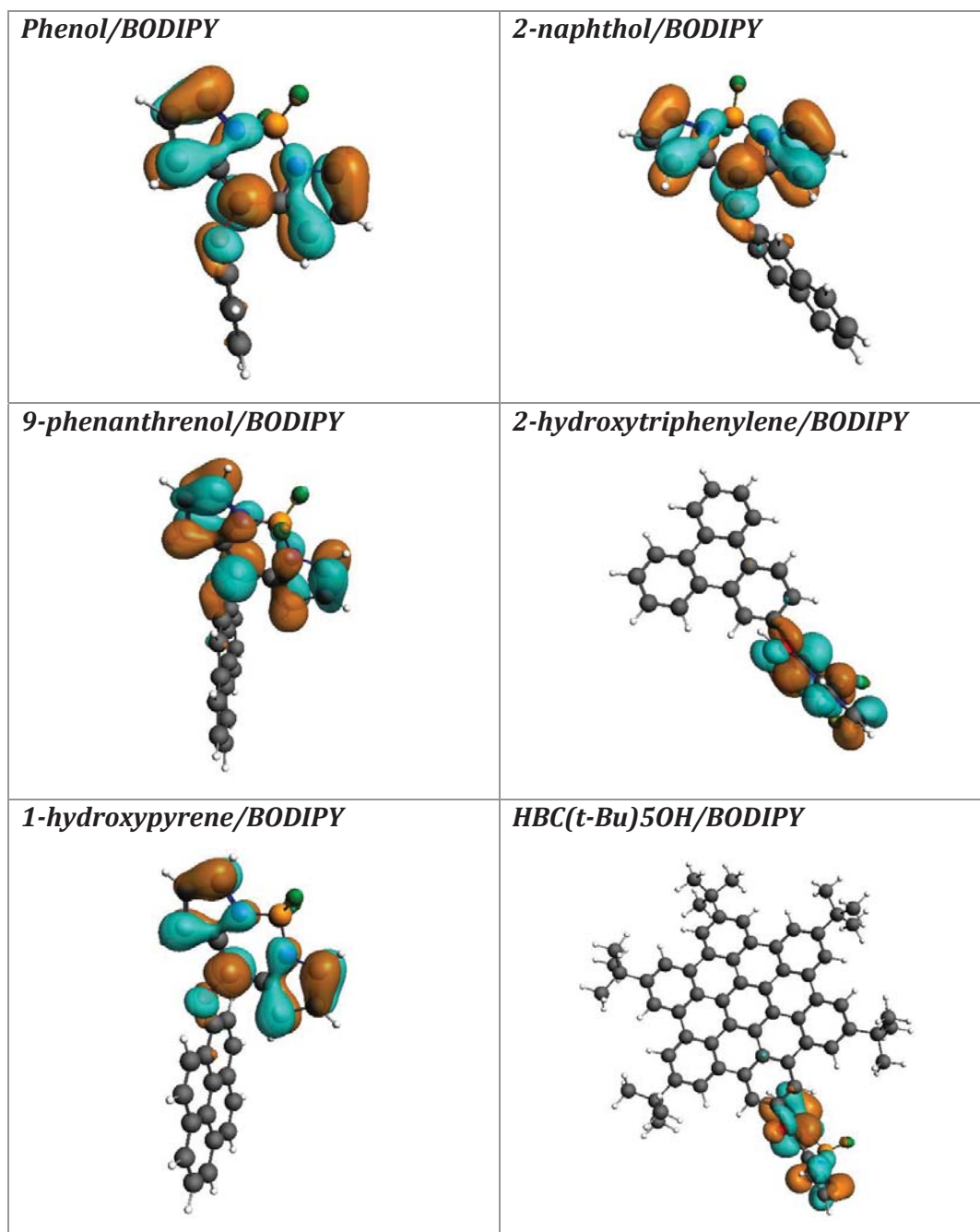


Figure 3.23 - LUMO for -O-BODIPY compounds

The Clar structures of the six analogues are also shown in Figure 3.22. As the proportion of non-benzenoid rings, i.e. those without the circle indicating mobility of electrons, increases the HOMO moves onto the aromatic region of the molecule. In comparison, the structures in which the aromatic regions have a high proportion of benzenoid character have HOMO located on the BODIPY region of the molecule.

For polycyclic aromatic hydrocarbons, Clar attributed a smaller HOMO-LUMO gap with lower kinetic stability.^{82, 92} From computational studies of the analogues themselves, the relative size of the HOMO-LUMO gap was found to be inversely proportional to the size of the analogue, with phenol having the largest HOMO-LUMO gap and HBC(*t-Bu*)₅OH having the smallest. The exception to this trend is 2-hydroxytriphenylene having a larger HOMO-LUMO gap than both 9-hydroxyphenanthrene and 1-hydroxypyrene. This is expected from the Clar interpretation of PAH structure, as 2-hydroxytriphenylene has a higher proportion of benzenoid character than the other structures, making it the more stable of the three compounds. This shows that the proportion of benzenoid character may be more important than size and functional group position for the determination of the HOMO-LUMO gap for analogues.

The effect of benzenoid character on molecular orbitals is demonstrated through the comparison of 2-hydroxytriphenylene/BODIPY and 1-hydroxypyrene/BODIPY. The Clar structure for triphenylene consists of three benzenoid rings, connected via a central non-benzenoid, making the proportion of benzenoid rings in triphenylene 75 %. In comparison, pyrene consists of two benzenoid rings and two non-benzenoid rings, making the proportion of benzenoid rings in pyrene 50 %.

This change in benzenoid proportion is evident in the movement of the HOMO from the BODIPY in triphenylene to the rings in pyrene. Phenanthrene has a benzenoid proportion of 67 %, indicating that upon BODIPY functionalisation the HOMO should lie somewhere between the two extreme cases of 1-hydroxypyrene/BODIPY and 2-hydroxytriphenylene/BODIPY. This is indeed what is seen for 9-hydroxyphenanthrene/BODIPY, showing that Clar theory can be used appropriately for the interpretation of the changes in molecular orbitals.

Relating differing proportions of benzenoid character to the HOMO-LUMO gap, it is evident those structures with more benzenoid character possess larger HOMO-LUMO gaps, and have HOMO located on the BODIPY region of the compound. Those structures with less benzenoid character, and HOMO located on the analogue, have smaller HOMO-LUMO gaps. As the size of the analogue is also likely to play a role in the size of the HOMO-LUMO gap, additional studies would be required on a range of analogues with different size and benzenoid proportion to better understand the relationship between benzenoid character and HOMO-LUMO gap.

Chapter 4. Spectroscopy of dipyrrens

The *meso*-substituted BODIPY compounds which have been previously reported in literature have been well studied spectroscopically, providing a wealth of information about their properties.^{49, 55, 59} Carrying on from the work of these groups, a large number of *meso*-substituted BODIPYs with larger substituent groups have been synthesised, as described in Chapter 2. and similar analyses have been performed to determine the effect of analogue size and edge-type on these *meso*-substituted BODIPYs. The results from these studies will be applied to understand the effect of BODIPY functionalisation on graphene nanoribbons in Chapter 5.

Computational studies are utilised to assist in explaining experimental observations, and to provide understanding of how functionalisation of analogues with BODIPY influence electronic properties. Time-dependent DFT calculations are used to help characterise features observed in experimental absorption spectra, and to understand the inter- and intramolecular interactions occurring in BODIPY-functionalised analogues.

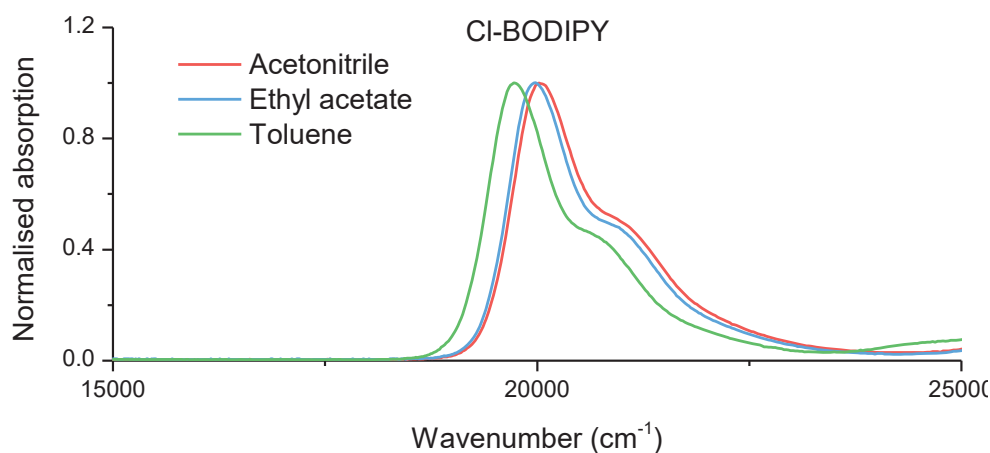


Figure 4.1 - Solvatochromism of Cl-BODIPY

Cl-BODIPY and its derivatives have been found to be solvatochromic,⁵⁹ as demonstrated by Figure 4.1, with an approximately 40 cm⁻¹ difference in absorption maxima wavelength between acetonitrile and ethyl acetate, and approximately 240 cm⁻¹ difference between ethyl acetate and toluene. As such, quantitative spectroscopic studies have been performed in solvents of different polarities, specifically, acetonitrile, ethyl acetate, and toluene.

4.1 Quantitative absorption studies

Absorption spectra were acquired using a Shimadzu UV-3101PC UV-Vis spectrophotometer. Quantitative absorption studies were performed on functionalised small-analogue compounds, as well as Cl-BODIPY, to determine the molar absorptivity. Functionalised analogues were not studied if they were not of sufficiently high purity to obtain quantitative results. Beer-Lambert plots have been produced for each compound and solvent combination in the same manner as that for 2-aminoanthracene/BODIPY in toluene in Figure 4.2.

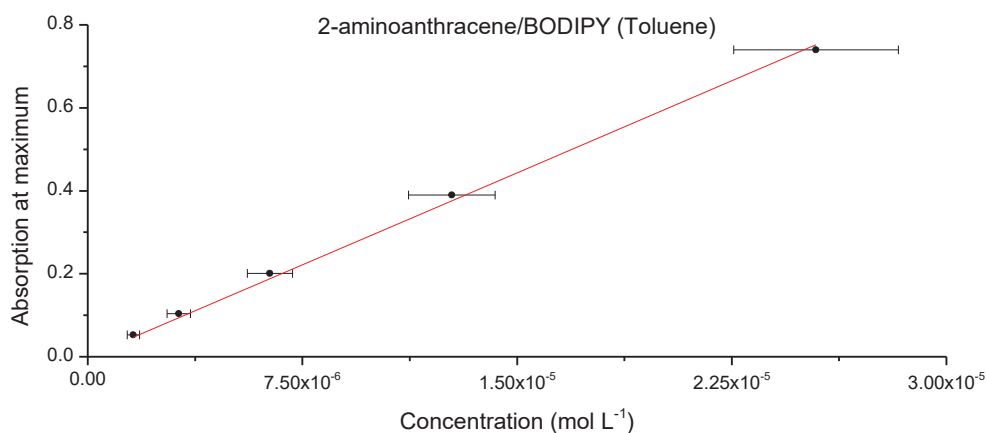


Figure 4.2 - Beer-Lambert plot for 2-aminoanthracene/BODIPY in toluene

Error bars were calculated taking measurement errors into account, but do not include additional error factors. Uncertainties in the concentration of initial stock

solutions were calculated according to (4-1), where m , V , and M_r are mass, volume, and molar mass respectively. The uncertainty in the mass, e_m , comes from the accuracy of the balance used, while the uncertainty in volume, e_V , is the stated uncertainty of the volumetric glassware used.

$$u_{stock} = c_{stock,max} - c_{stock} = \left(\frac{\left(\frac{m + e_m}{V - e_V} \right)}{M_r} \right) - \left(\frac{\left(\frac{m}{V} \right)}{M_r} \right) \quad (4-1)$$

The uncertainty in subsequent dilutions from the stock solution were calculated according to (4-2), where c_x is the concentration of the stock or previous dilution, with $u_{c(x)}$ its corresponding uncertainty, while the volume ratio $v.r.$ has corresponding uncertainty $u_{v.r.}$ given by (4-3), and where V_x is the volume of stock added, and V_{dil} is the final volume of the diluted solution. The uncertainties $e_{V(x)}$ and $e_{V(dil)}$ are given by the accuracy of the volume measurement, in this case given by the smallest division on the pipettes used.

$$u_{dil} = \left((c_x + u_{c(x)}) \times (v.r. + u_{v.r.}) \right) - (c_x \times v.r.) \quad (4-2)$$

$$u_{v.r.} = \left(\frac{V_x + e_{V(x)}}{V_{dil} + e_{V(dil)}} \right) - \left(\frac{V_x}{V_{dil}} \right) \quad (4-3)$$

Molar absorptivity coefficients for the studied compounds are shown in Table 4.1. In general, the functionalised analogues have smaller molar absorptivity coefficients than Cl-BODIPY, however there are some exceptions to this with 1-naphthol/2xBODIPY having a significantly higher molar absorptivity coefficient than Cl-BODIPY in both ethyl acetate and toluene. There is also a trend for those analogues which are functionalised via an amine to have smaller molar absorptivity coefficients than those functionalised via hydroxyl groups.

Table 4.1 – Summary of molar absorptivity coefficients ($\text{mol}^{-1}\text{Lcm}^{-1}$) for Cl-BODIPY and its small-analogue products. Standard errors (rounded to 1 significant figure) are included in brackets

	Acetonitrile	Ethyl acetate	Toluene
Cl-BODIPY	44400 (500)	52000 (1000)	51400 (300)
Aniline/BODIPY	11000 (3000)	19500 (700)	25000 (200)
1-naphthol/2xBODIPY	36000 (500)	58000 (4000)	67000 (2000)
2-naphthol/BODIPY	27800 (400)	33000 (1000)	37700 (800)
2-naphthol/2xBODIPY 464 nm	16700 (200)	22200 (700)	22900 (700)
2-naphthol/2xBODIPY 510 nm	18900 (300)	15700 (200)	16300 (400)
1-naphthylamine/BODIPY	5700 (900)	20500 (100)	21960 (60)
2-naphthylamine/BODIPY	13800 (700)	25200 (500)	23000 (500)
2-aminoanthracene/BODIPY	3170 (70)	15600 (300)	29600 (400)
9-phenanthrenol/BODIPY	17900 (90)	26700 (300)	27600 (500)
1-hydroxypyrene/BODIPY	29600 (800)	26700 (300)	27600 (500)
2-hydroxytriphenylene/BODIPY	27000 (700)	37000 (600)	37000 (1000)
HBC(<i>t</i> -Bu) ₅ OH/BODIPY	20700 (200)	26060 (50)	26100 (200)
HPB(<i>t</i> -Bu) ₅ OH/BODIPY	23000 (1000)	29600 (400)	27700 (700)
Benzoic/BODIPY	18100 (100)	33000 (600)	39800 (900)

4.1.1 TD-DFT studies of excitations

Time-dependent (TD) DFT calculations can be used to assist with the understanding of absorption spectra. All TD-DFT calculations have been performed using optimised geometries from B3LYP/DZP calculations. To ensure both high quality of results and low computational time cost, several functionals were tested using the small phenol/BODIPY structure. As TD-DFT calculations are unable to be performed using frozen-core for hybrid functionals in ADF, calculations were performed using the PBE functional both with and without a frozen core. It was found the effect of the frozen core was minimal, and therefore deemed appropriate to include hybrid functionals in the test cases. The functionals used were PBE,

B3LYP, MO62X, and BLYP. It was found that, overall, B3LYP gave the best results for the time cost. TD-DFT calculations were therefore performed on all BODIPY-functionalised analogue structures using B3LYP/DZP. Although it was assumed no singlet-triplet excitations would occur, excitations were calculated for both singlet and triplet states for all structures to confirm this.

4.1.2 Solvent dependent excitations

Significant solvent dependence is observed in 1-naphthol/2xBODIPY (Figure 4.3). Significant solvatochromism is observed, with the absorption maxima for toluene and ethyl acetate being approximately 240 cm^{-1} different, and the difference between ethyl acetate and acetonitrile being approximately 500 cm^{-1} . This solvatochromism is significantly larger than that observed for Cl-BODIPY. The shoulder at approximately 21000 cm^{-1} changes in relative intensity in different solvents also, a behaviour which is not observed significantly in monosubstituted structures. This indicates that solvent properties have much more influence over disubstituted analogues.

Additionally, there is an absorption band of significant intensity at low energy observed only in acetonitrile. This is seen to a very small extent in ethyl acetate, and is not observed at all in toluene. This is likely due to intermolecular interactions facilitated by the polar acetonitrile.

To further investigate the interactions occurring in 1-naphthol/2xBODIPY, and any solvent effects, TD-DFT calculations were utilised. All four solvents utilised the same initial geometry for consistency, as solvent model can have a small effect on optimised geometry. Geometry optimisations were also performed with solvent models to determine the effect on energy. It was found that the geometry used for

TD-DFT and those optimised utilising solvent models were less than 2 *kT* different, indicating this method is sensible.

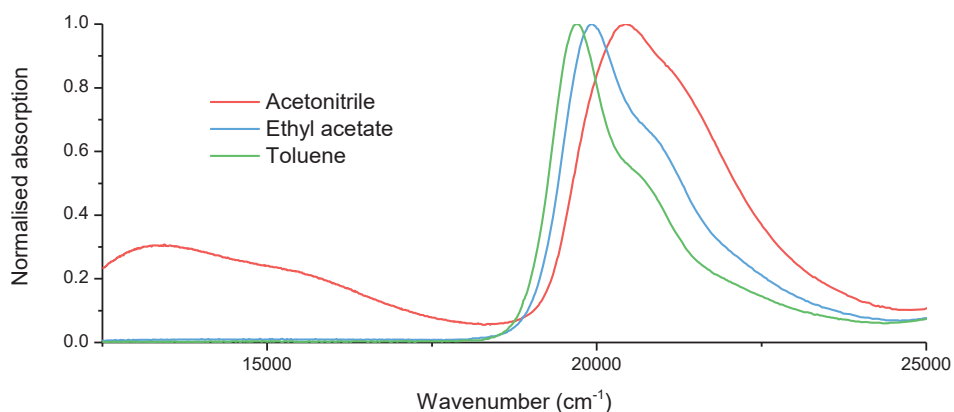


Figure 4.3 - Normalised absorption spectra of 1-naphthol/2xBODIPY

As expected, no singlet-triplet interactions were observed. TD-DFT excitation spectra are shown in Figure 4.4. An excitation is described by a pair of occupied and virtual orbitals, and the contribution of each excitation to the transition is determined by the height of the coloured bars in the stacked bar plots. Only excitations with oscillator strength greater than 0.1 are included, and the orbitals which these excitations consist of are shown in Figure 4.5 and Figure 4.6 respectively. Assignments have been performed according to percentage contributions from TD-DFT output, with any individual contributions less than 10% assigned to an “other” category.

The calculations performed without a solvent model act as a control, and can be compared against TD-DFT calculations for other compounds for which solvent models have not been included. There are two significant excitation bands, with the band at 0.13 Hartree being due to predominantly exciton interactions, which are interactions occurring between different chromophores, i.e. the HOMO occurring on one BODIPY with the LUMO occurring on the other. The larger band at 0.115 Hartree

involves two strong excitations, with both consisting of local, i.e. within one BODIPY molecule, and exciton interactions.

The molecular orbitals are dependent on solvent model. In accordance with Figure 4.5, α corresponds to the HOMO for toluene and the no solvent case, whereas it corresponds to the HOMO-1 for ethyl acetate and acetonitrile, with their HOMO corresponding to β . The four cases share the same HOMO-2, but again have different molecular orbitals for the other cases shown. Acetonitrile and ethyl acetate have HOMO-3 and HOMO-4 corresponding to η and ι respectively, in comparison with ζ and θ for toluene and the no solvent case. HOMO-5 for the three cases involving a solvent model correspond to η in comparison to ζ in the absence of solvent. This is interesting, as the HOMO-3 is equivalent to HOMO-5 for all cases except toluene, indicating that HOMO-5 is more sensitive to solvent polarity than HOMO-3. Overall, the solvent dependence on molecular orbitals is very interesting, and assists with understanding the solvent dependent behaviour of the functionalised compounds.

The inclusion of a solvent model causes significant differences in the energies of excitation bands, and the types of excitations observed. Focussing on the most intense bands in each spectrum, it can be seen that the band consists of predominantly local and charge-transfer interactions, which are interactions between the BODIPY chromophore and the analogue structure. The local interactions observed consist of exciton interactions also, with transfer of electron density between the two dipyrin molecules observable. Looking at the higher energy bands, there are two bands corresponding to charge transfer ($\eta - \Lambda$) seen in ethyl acetate.

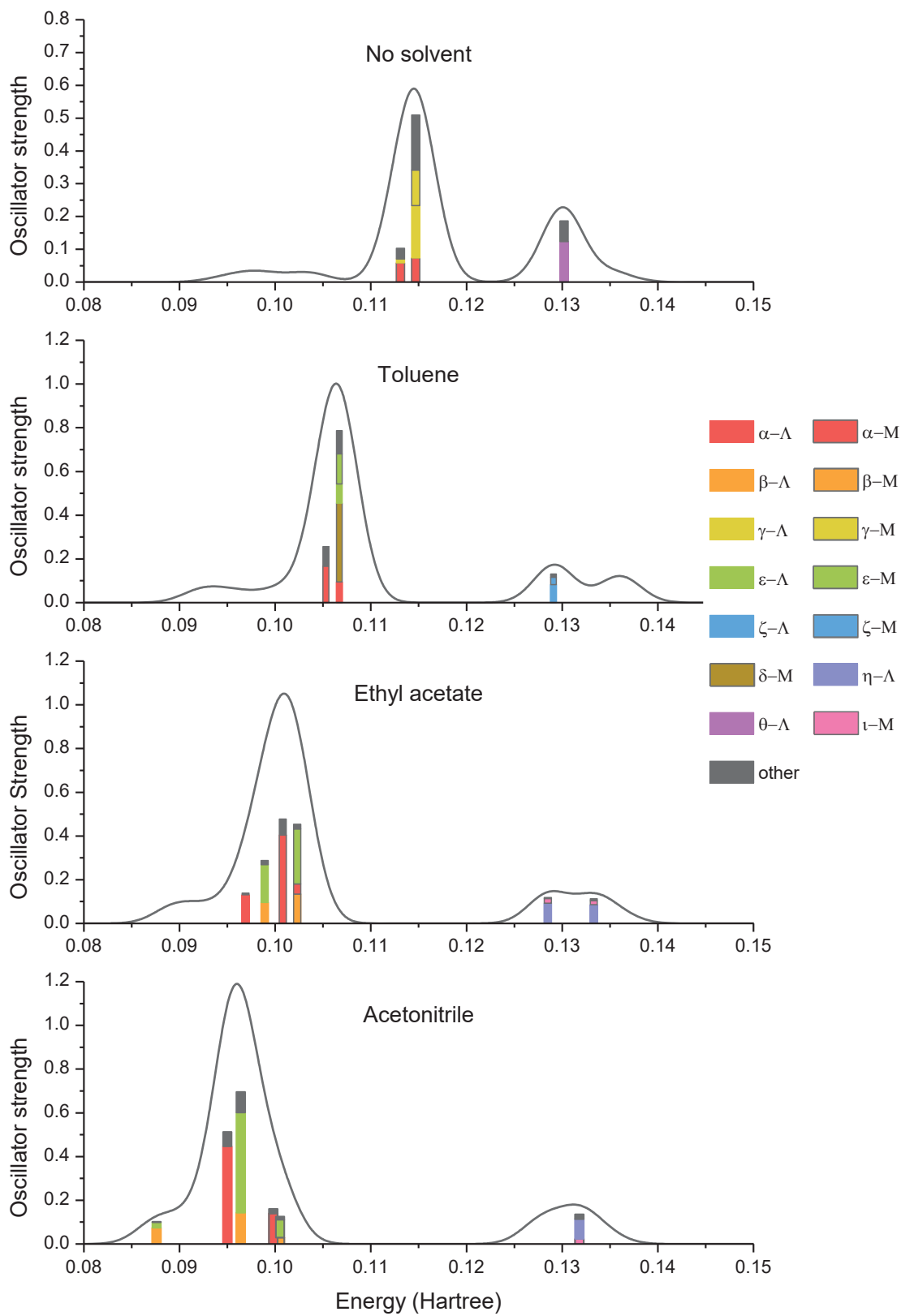


Figure 4.4 - TD-DFT excitation spectra of 1-naphthol/2xBODIPY; Modes with oscillator strength > 0.1 have been assigned to molecular orbital transitions

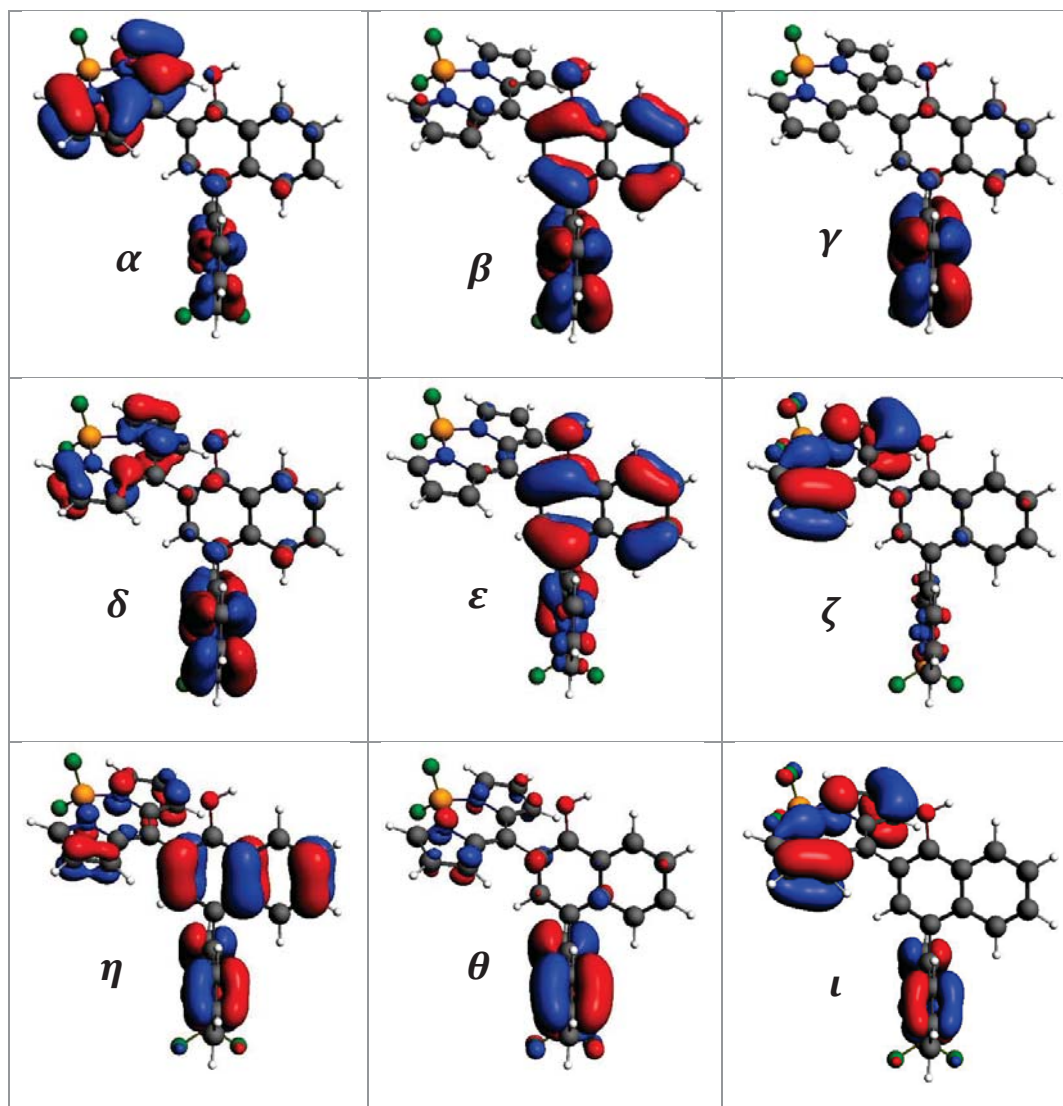


Figure 4.5 - Occupied orbitals: 1-naphthol/2xBODIPY

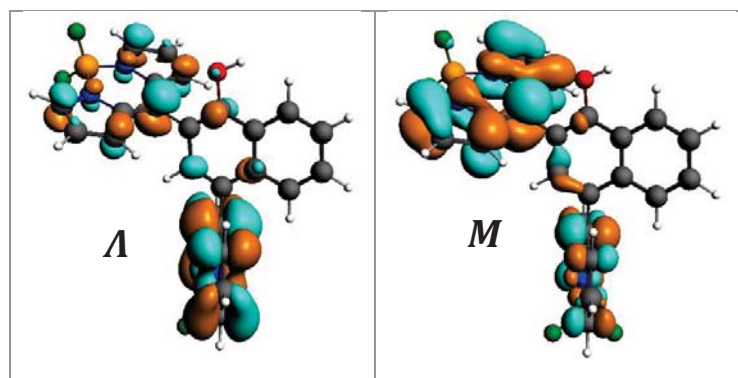


Figure 4.6 - Virtual orbitals: 1-naphthol/2xBODIPY

Going to a less polar solvent model, the intensity of the highest energy band decreases to an oscillator strength less than 0.1, while the band just below 0.13 Hartree becomes attributable to a predominantly exciton interaction, like that observed with the absence of a solvent model. Looking at the more polar acetonitrile, the opposite behaviour has occurred, with the higher energy excitation now becoming predominant, and corresponding to charge transfer, as with ethyl acetate. This band, and its changes, corresponds to the behaviour of the shoulder observed in the experimental absorption spectra.

Another noticeable change in excitations with solvent polarity occurs at low energy, with the appearance of a mostly exciton interaction with increasing solvent polarity. This excitation is visible in toluene and ethyl acetate also, however, it has a total oscillator strength of approximately 0.04 in toluene, and 0.06 in ethyl acetate. This indicates that the strength of exciton interactions is proportional to solvent polarity. This solvent-dependent exciton interaction likely corresponds with the large absorption band observed for 1-naphthol/2xBODIPY in acetonitrile, and demonstrates why this band is not observed experimentally in solvents of lower polarity.

4.1.3 Effect of double-substitution on spectra

The normalised absorption spectra of 2-naphthol/1xBODIPY, shown in Figure 4.7 contain a single peak at approximately 22000 cm^{-1} in all three solvents. As for Cl-BODIPY, solvatochromism is evident in this compound also. The absorption maxima gaps are similar, however, the difference of 100 cm^{-1} in absorption maxima wavelength between acetonitrile and ethyl acetate is much larger than for Cl-

BODIPY, while the 260 cm^{-1} difference between ethyl acetate and toluene is very similar.

Figure 4.7 demonstrates the differences between normalised absorption spectra of mono- and di- BODIPY functionalised 2-naphthol. Firstly, a second absorption band has appeared at approximately 19500 cm^{-1} . Due to the appearance of the secondary absorption band, molar absorptivity coefficients have been calculated for both peaks for this compound. Additionally, Figure 4.7 shows that the solvatochromism is highly evident for the band at approximately 450 nm, but is not significantly changed from Cl-BODIPY for that at 500 nm. The solvatochromism is not as large as for that of 1-naphthol/2xBODIPY, indicating that both bonding position and the type of bonding between the BODIPY and aromatic structure influence exciton excitations and solvatochromism. TD-DFT results for both structures, shown in Figure 4.8, can be used to aid in the understanding of this.

The monosubstituted 2-naphthol structure exhibits both local ($\beta - \Lambda$) and charge transfer ($\alpha - \Lambda$) excitations in the most intense band at approximately 0.12 Hartree. At higher energy, the strongest excitations are predominantly local within the dipyrin part of the structure, with some charge transfer occurring between α and M.

The disubstituted structure also demonstrates some charge transfer ($\eta - N$), however this only occurs at lower energy, and there is a distinct lack of excitations observed in the higher energy part of the spectrum compared to the monosubstituted case.

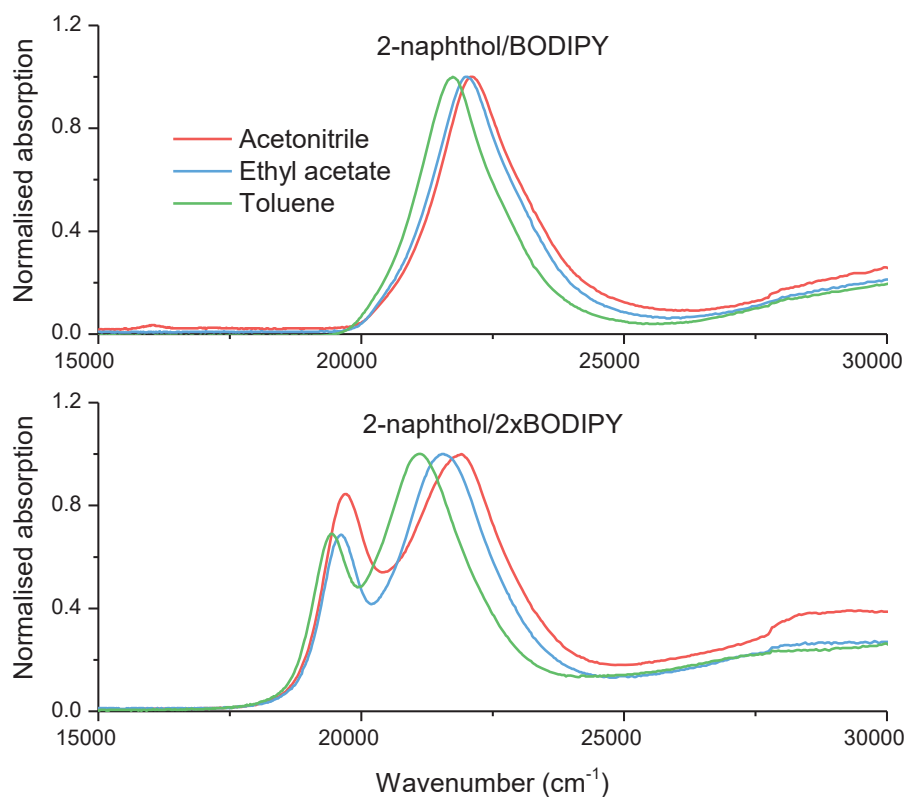


Figure 4.7 - Absorption spectra of 2-naphthol/1x and 2xBODIPY

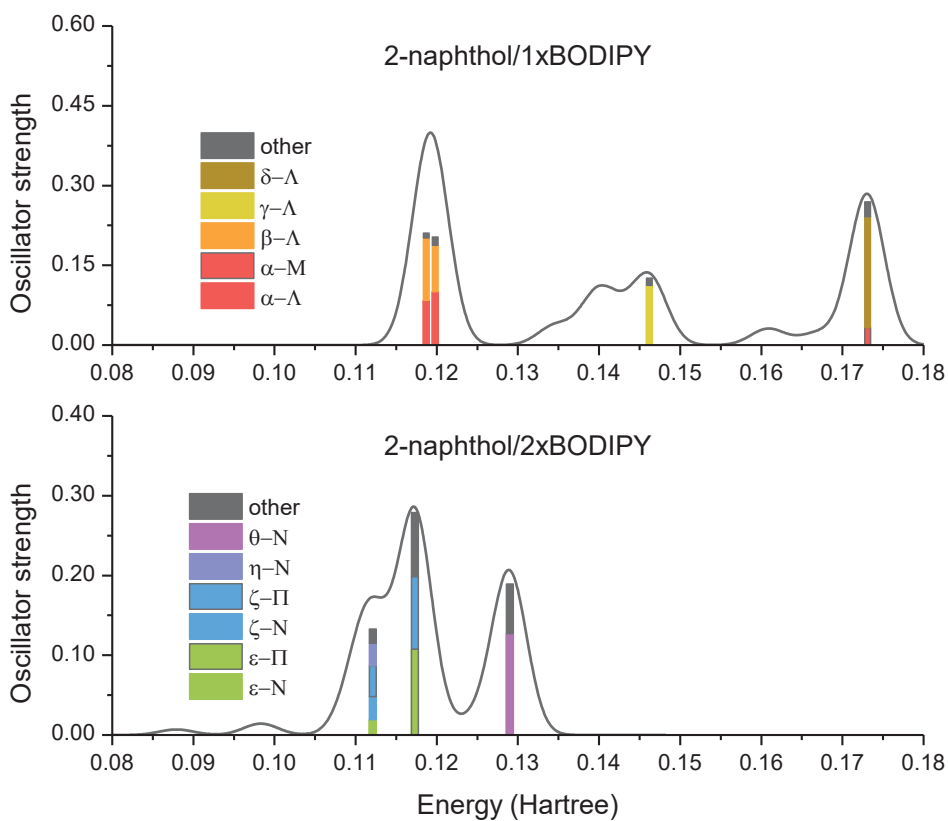


Figure 4.8 - TD-DFT excitation spectra of 2-naphthol/1x and 2xBODIPY; Modes with oscillator strength > 0.1 have been assigned to molecular orbital transitions

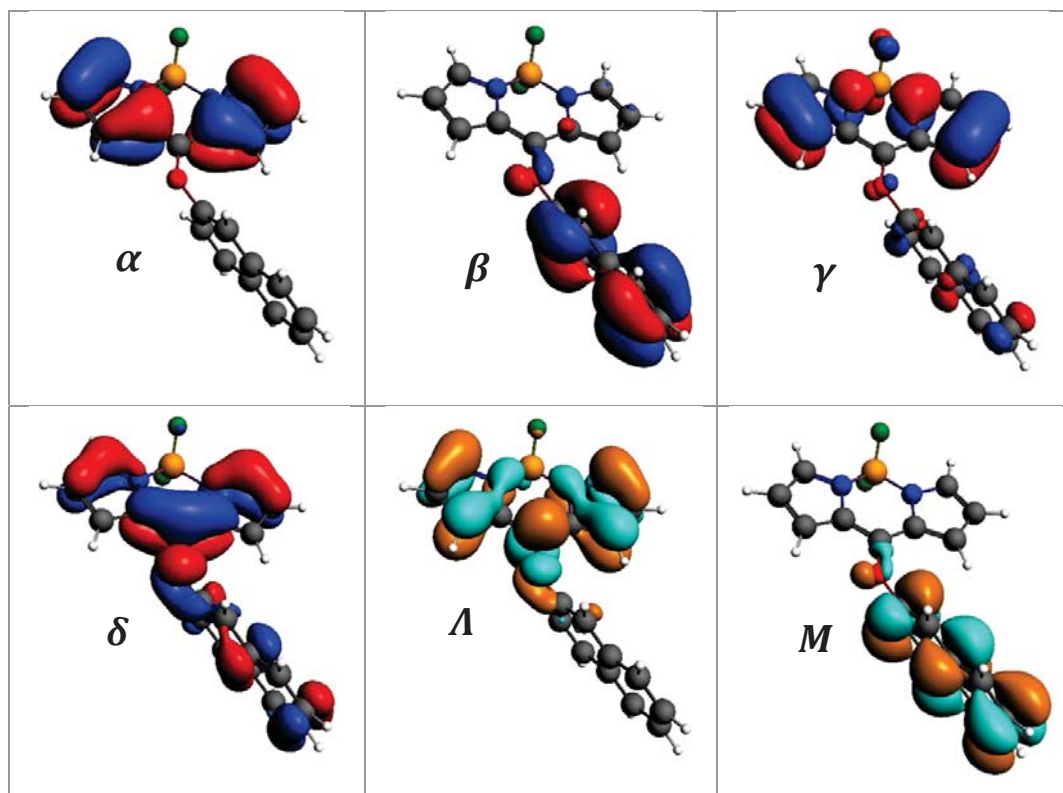


Figure 4.9 - Occupied (blue and red) and virtual (orange and teal) orbitals: 2-naphthol/1xBODIPY

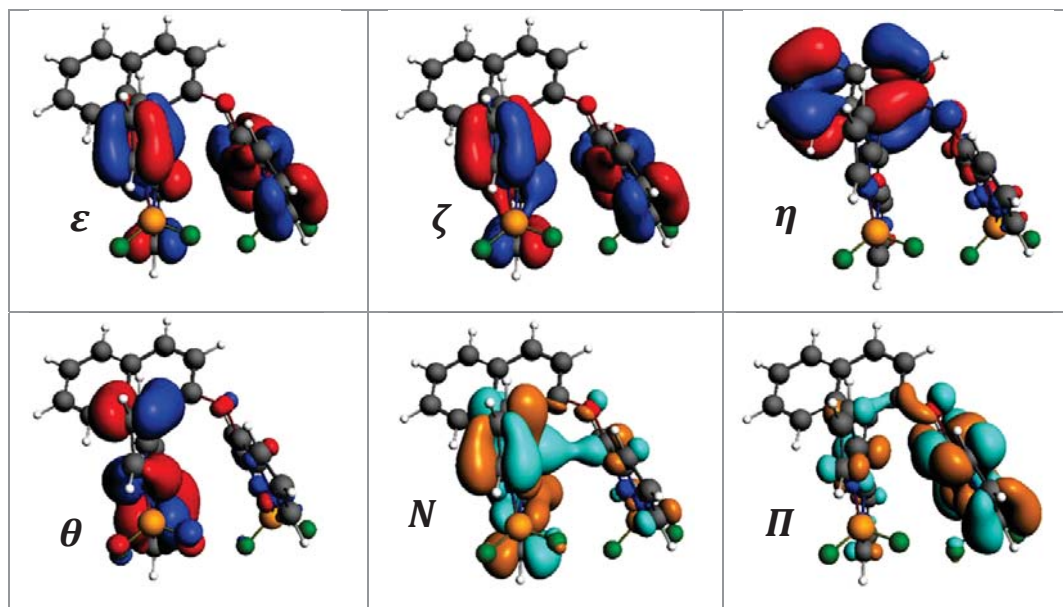


Figure 4.10- Occupied (blue and red) and virtual (orange and teal) orbitals: 2-naphthol/2xBODIPY

As with 1-naphthol/2xBODIPY, excitation bands are observed at low energy. The strength of these excitations is very low (0.0069 for the excitation at 0.09 Hartree, and 0.0142 at 0.10 Hartree) so they have not been explicitly included in Figure 4.8, however they are attributable to $\varepsilon - N/M$ and $\zeta - N/M$ transitions, which consist of a combination of exciton and local interactions between dipyrin molecules within the structure. The large, local transition at 0.13 Hartree occurs within the C-C bonded dipyrin, and is analogous to the transition observed at 0.13 Hartree for 1-naphthol/2xBODIPY. From 1-naphthol/2xBODIPY results, the nature of this band is highly solvent dependent, indicating that experimental absorption spectra would demonstrate large shifts in peak position due to changes in interactions, which is what is observed in the band at 22000 cm^{-1} in Figure 4.3. The differences in solvatochromic shift between the two structures is likely due to differences in relative position of the two dipyrins within the molecule.

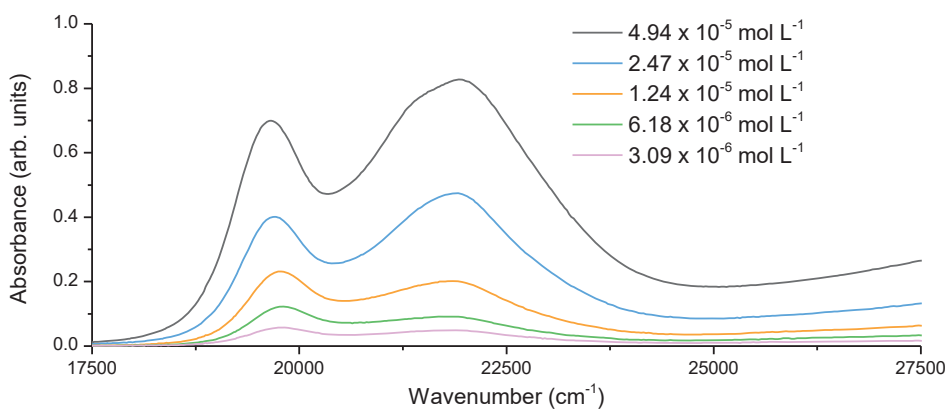


Figure 4.11 - Absorption spectra of 2-naphthol/2xBODIPY in acetonitrile at different concentrations

Another interesting phenomenon is observed in the absorption spectra of 2-naphthol/2xBODIPY in acetonitrile, shown in Figure 4.11, with the dominant band in the absorption spectra changing as concentration increases. The exciton nature of this band observed in the absence of a solvent model is likely shifted towards a

charge transfer interaction in solvents of high polarity, as observed with 1-naphthol/2xBODIPY. The changing dominance of this band can be explained by an increase in intermolecular charge transfer, or aggregation, with increasing concentration. It is likely only acetonitrile has high enough polarity to induce this effect.

4.1.4 Exciton coupling in multi-chromophore systems

Exciton coupling behaviour exhibited by the two disubstituted compounds can be better understood through the investigation of relative dipole angles, and thus the strength of coupling, in accordance with the work of Kasha *et al.*⁹³

Upon excitation from a ground electronic state via photon absorption a change in electron density occurs between the two states, creating an instantaneous dipole, μ . This is described by a vector with an orientation corresponding to the direction of electron displacement.⁹⁴ The transition dipole moment, μ , for BODIPY is shown in Figure 4.12.

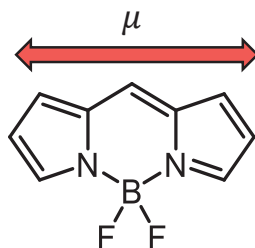


Figure 4.12 - Transition dipole for BODIPY

When multiple chromophores are in close proximity the electronic excitation becomes delocalised over all chromophores. This is known as exciton coupling. The orientation of these chromophores impacts the extent of exciton coupling which occurs.

The orientation of two transition dipole moments, μ_A and μ_B , can be utilised to quantify the strength of exciton coupling, J , through (4-4), where r is defined in Figure 4.13 (a). An alternative expression to calculate J , (4-5), utilises the centres of gravity of the chromophores, as shown in Figure 4.13 (b).

$$J = \frac{\mu_A \cdot \mu_B}{r^3} - 3 \frac{(\mu_A \cdot r)(\mu_B \cdot r)}{r^5} \quad (4-4)$$

$$J = \frac{\mu^2}{r^3} (\cos \beta - 3 \cos \alpha \cos \alpha') \quad (4-5)$$

The relationships in (4-4) and (4-5) can be used to provide relative exciton strengths for two different chromophore orientations where transition dipole moments are equal across all chromophores but not explicitly known. If either α angle goes to 90° , the overall exciton coupling is described only by β , and vice-versa in accordance with (4-5). The strongest coupling will therefore occur when the two cosine terms are out of phase.

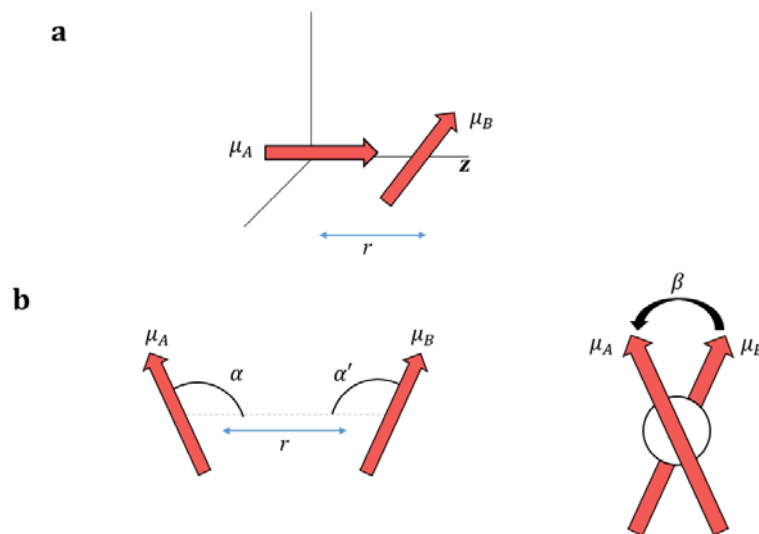


Figure 4.13 - Geometrical parameters used to define the orientation of two transition dipole moments (Adapted from Ref. 94)

To quantify the relative strengths of exciton coupling occurring in the doubly BODIPY substituted compounds, the values of α , α' , β , and r are required for each structure. Figure 4.14 shows the structures of interest, with red vectors indicating

the dipole transition moment, and a red vector connecting the centres of mass analogous to r . The values of these parameters are shown in Table 4.2, where J/μ^2 is the exciton strength relative to the dipole moment.

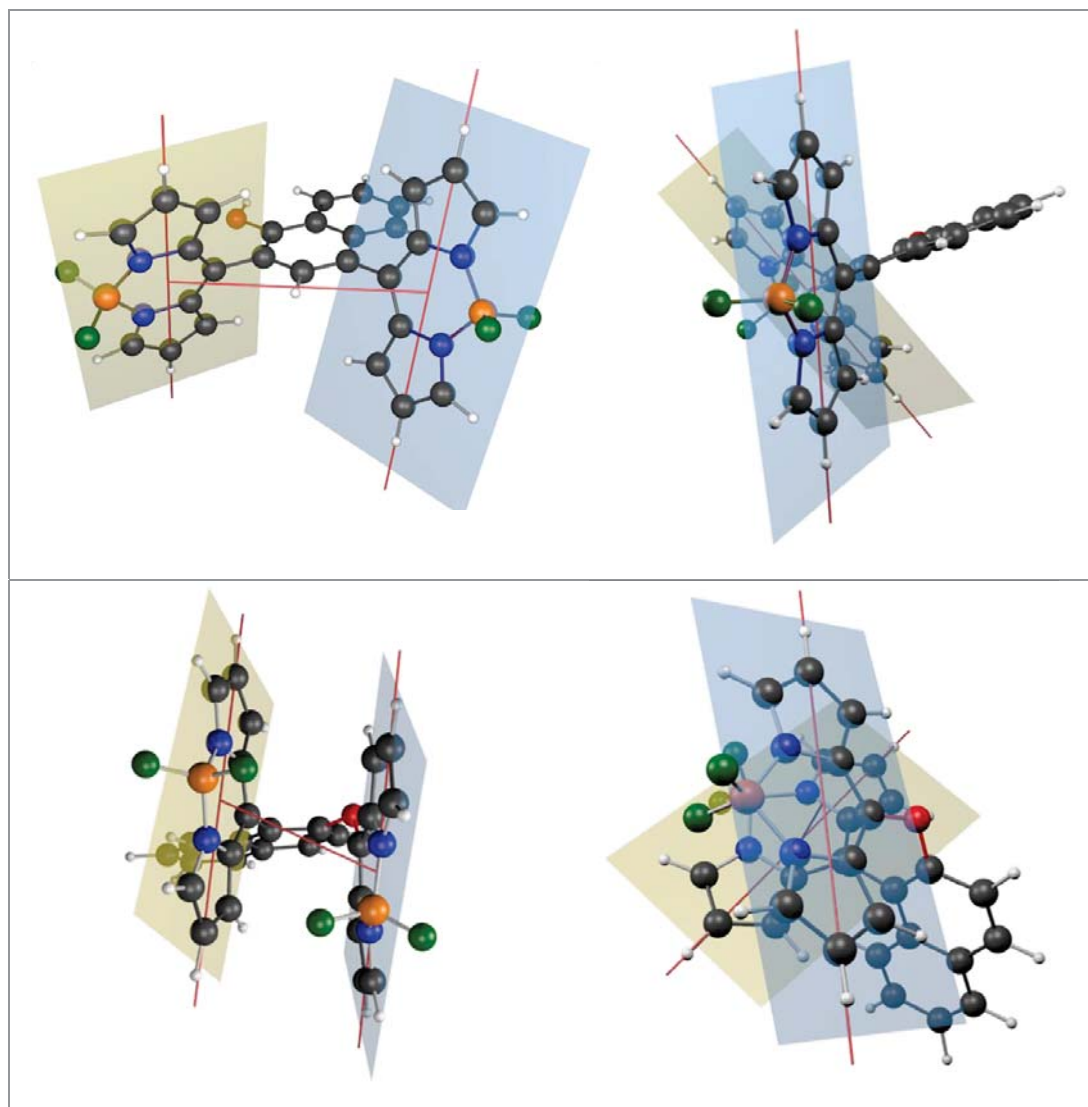


Figure 4.14 - Determination of geometrical parameters for 1-naphthol/2xBODIPY (top) and 2-naphthol/2xBODIPY (bottom) with α and α' (left) and β (right). BODIPY planes (long axis = dipole) are shown for clarity

From (4-5) it is evident that the most significant influence on the strength of exciton coupling is from the distance between the centres of mass of the chromophores, r . The cubing of this term causes small differences in distance to correspond to significant differences in exciton strength. The data in Table 4.2

confirms this. The difference in the values of $\cos \beta - 3 \cos \alpha \cos \alpha'$ for the two compounds is small, however, the difference in r is almost 3 Å, which causes a difference in relative exciton strength of approximately $7 \times 10^{-3} \text{ Å}^{-3}$.

Table 4.2 - Geometrical parameters for exciton coupling

	1-naphthol/2xBODIPY	2-naphthol/2xBODIPY
α	78.7°	87.6°
α'	79.6°	109.8°
β	29.5°	45.6°
r (Å)	7.188	4.307
$\cos \beta - 3 \cos \alpha \cos \alpha'$	0.764	0.742
$\frac{J}{\mu^2}$ (Å ⁻³)	2.06×10^{-3}	9.29×10^{-3}

The difference in relative exciton strength agree with information obtained from TD-DFT calculations. Looking at the solvent exempt cases of doubly substituted compounds, the relative oscillator strengths of the purple exciton interactions in both Figure 4.4 and Figure 4.8 at 0.13 Hartree can be observed. The magnitude of exciton coupling relative to the most intense excitation band is larger for 2-naphthol/2xBODIPY, indicating larger exciton coupling strength for this compound in agreement with Table 4.2.

4.2 Quantitative emission studies

4.2.1 Determination of Quantum Yields

Quantum yields for Cl-BODIPY and substituted analogues were determined using the method of Telfer *et al.*⁹⁵ Relative quantum yields are determined relative to a sample of known quantum yield according to (4-6), where subscripts x and s refer to the unknown and the standard, respectively. A is the absorbance at the

excitation wavelength, F is the area under the corrected emission curve, and n is the refractive index of the solvents used.

$$\Phi_{F(x)} = \left(\frac{A_s}{A_x}\right) \left(\frac{F_x}{F_s}\right) \left(\frac{n_x}{n_s}\right)^2 \Phi_{F(s)} \quad (4-6)$$

In systems where triplet formation is possible, oxygen must be removed through freeze-pump-thaw, or other, methods. Although it was assumed in this case that no triplet formation would occur, tests were performed using samples which had and had not had oxygen removed. It was found there were no differences between emission spectra of the two sample types, and therefore samples did not require oxygen removal prior to emission studies.

The reference standards used for this study were Coumarin 334, for excitation wavelengths between 440 nm and 470 nm, and Coumarin 6H, for excitation wavelengths between 390 nm and 440 nm. A literature quantum yield was found for Coumarin 334; however, this only appears in one resource with no additional reference provided, and is also stated as having two different values (0.60 and 0.69) within the body of the paper and supporting information.⁹⁶ Additionally, a literature quantum yield was not able to be found for Coumarin 6H. As such, it was decided to measure quantum yields for the two standards directly using an integrating sphere. Steady-state photoluminescence measurements were recorded using an Edinburgh Instruments FLS980 fluorescence spectrometer with a Xe lamp as light source (Edinburgh Instruments, Edinburgh, Scotland).

Coumarin 334 and 6H were used as-received from Sigma-Aldrich and diluted in absolute ethanol for emission measurements. The values obtained using the integrating sphere method were Φ (Coumarin 334) = 0.5469, and

Φ (Coumarin 6H) = 0.9632. To confirm these values were reasonable, $\Phi_{F(x)}$ was calculated for Coumarin 6H relative to Coumarin 334 according to equation (4-6), with a value of 0.9658. The closeness of relative and directly measured quantum yields for Coumarin 6H confirms the quality relative quantum yield determination method.

Table 4.3 - Relative quantum yields. * indicates reference standard used is Coumarin 6H; all others calculated with Coumarin 334 as standard

	Acetonitrile	Ethyl acetate	Toluene
Cl-BODIPY	0.446 ± 0.003	0.501 ± 0.003	0.440 ± 0.002
Aniline/BODIPY	0.012 ± 0.001	0.026 ± 0.001	0.084 ± 0.001
1-naphthol/2xBODIPY	0.000	0.001 ± 0.001	0.058 ± 0.001
2-naphthol/BODIPY	0.000	0.008 ± 0.001	0.442 ± 0.001
2-naphthol/2xBODIPY	0.010 ± 0.001	0.001 ± 0.001	0.005 ± 0.001
1-naphthylamine/BODIPY	0.003 ± 0.001*	0.007 ± 0.001*	0.019 ± 0.001*
2-naphthylamine/BODIPY	0.018 ± 0.001*	0.025 ± 0.001*	0.059 ± 0.001*
2-aminoanthracene/BODIPY	0.005 ± 0.001*	0.158 ± 0.001*	0.270 ± 0.001*
9-phenanthrenol/BODIPY	0.014 ± 0.001	0.007 ± 0.001	0.165 ± 0.001
1-hydroxypyrene/BODIPY	0.000	0.000	0.000
2-hydroxytriphenylene/BODIPY	0.000	0.006 ± 0.001	0.300 ± 0.001
HBC(<i>t-Bu</i>) ₅ OH/BODIPY	0.061 ± 0.001	0.006 ± 0.001	0.005 ± 0.001
HPB(<i>t-Bu</i>) ₅ OH/BODIPY	0.008 ± 0.001	0.001 ± 0.001	0.321 ± 0.001
Benzoic/BODIPY	0.506 ± 0.002	0.531 ± 0.001	0.407 ± 0.001

Samples were prepared to have maximum absorption intensity of approximately 0.1 to reduce self-absorption events. Emission spectra were obtained using a Perkin Elmer LS 50B Luminescence Spectrometer. Relative quantum yields are listed in Table 4.3. In cases where the quantum yields were outside the detection limit, they have been reported as 0.000 and no uncertainties have been included.

Quantum yields for Cl-BODIPY and aniline/BODIPY have been previously reported by Dehaen et al.⁵⁹ The values calculated in this study are not in agreement

with those, with the quantum yields for Cl-BODIPY calculated here being much lower, and those for aniline/BODIPY being significantly higher than those calculated by the Dehaen group. The reasons for these discrepancies are unknown, however may be due to differences in fluorescence standards used.

4.2.2 3-Dimensional emission plots

3-Dimensional emission scans of Cl-BODIPY in solvents of differing polarity were performed, and the data is shown in Figure 4.16 and Figure 4.17. The plots show additional emission at $\lambda_{\text{ex}} \cong 380$ nm in some solvents. This behaviour was initially observed in toluene, and to a much lesser extent in acetonitrile, but was not observed in ethyl acetate, which has an intermediate solvent polarity. To further investigate this behaviour, additional emission-excitation studies were performed in chloroform, chlorobenzene, and isopropyl alcohol. This behaviour was again observed in chloroform and isopropyl alcohol, but not in chlorobenzene.

Figure 4.15 highlights in shades of red the solvents which cause this behaviour to be observed, with a darker red indicating strong emission of this $\lambda_{\text{ex}} \cong 380$ nm band. No trends in solvent polarity are observable, indicating this behaviour is not caused solely by solvent polarity.

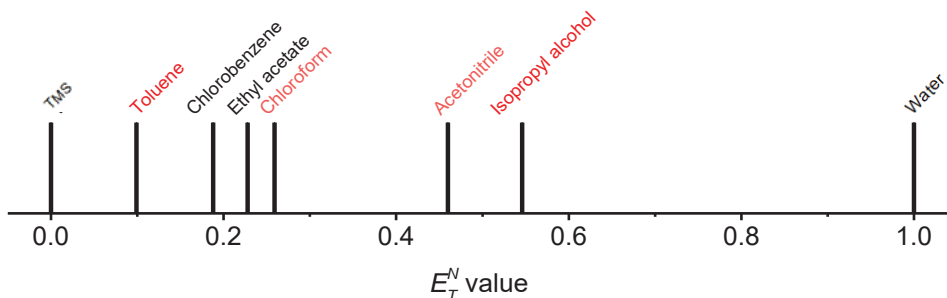


Figure 4.15 - E_T^N scale for selected solvents

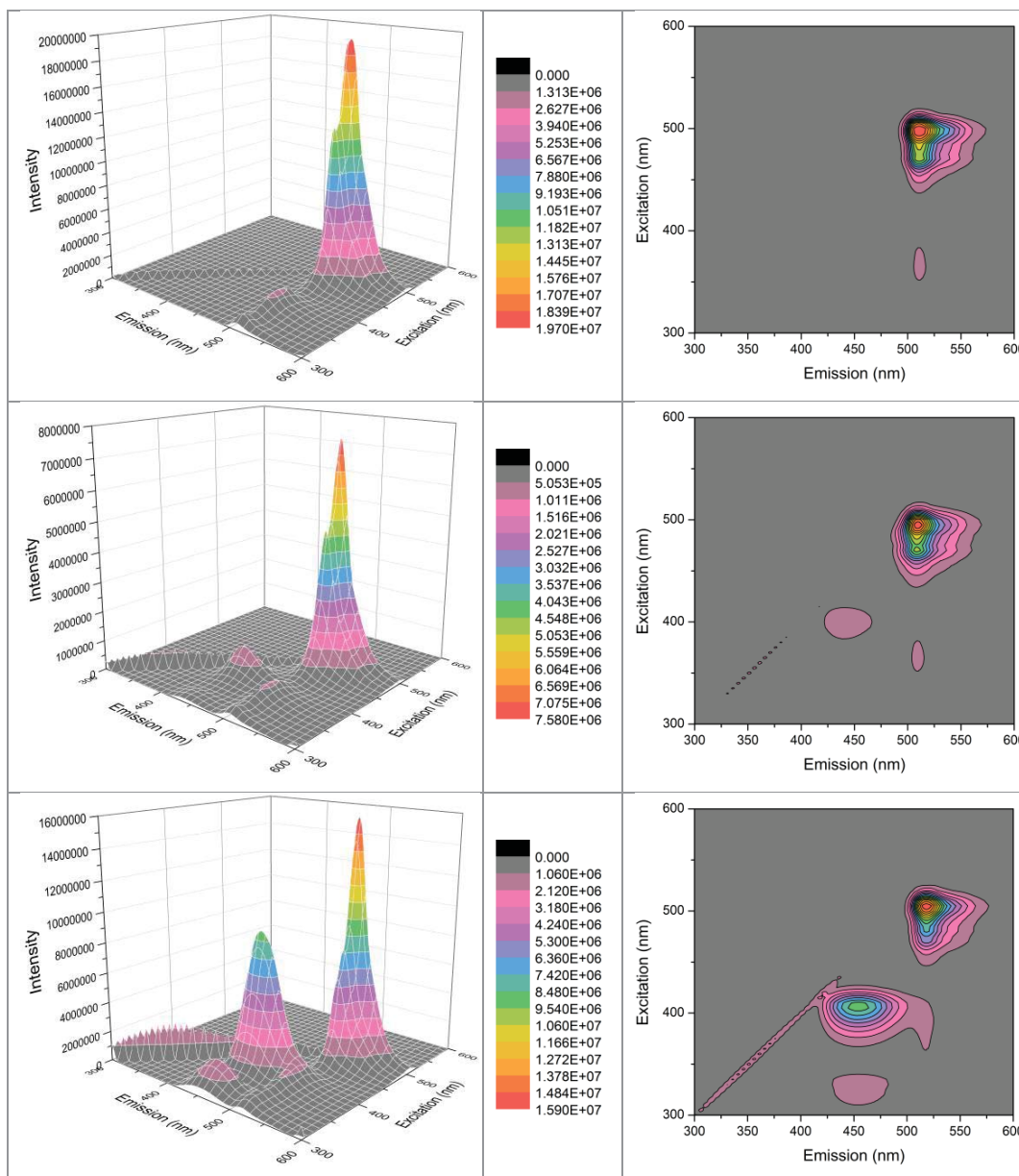


Figure 4.16 - 3D (left) and contour (right) plots of Cl-BODIPY in: ethyl acetate (top); acetonitrile (centre); and toluene (bottom)

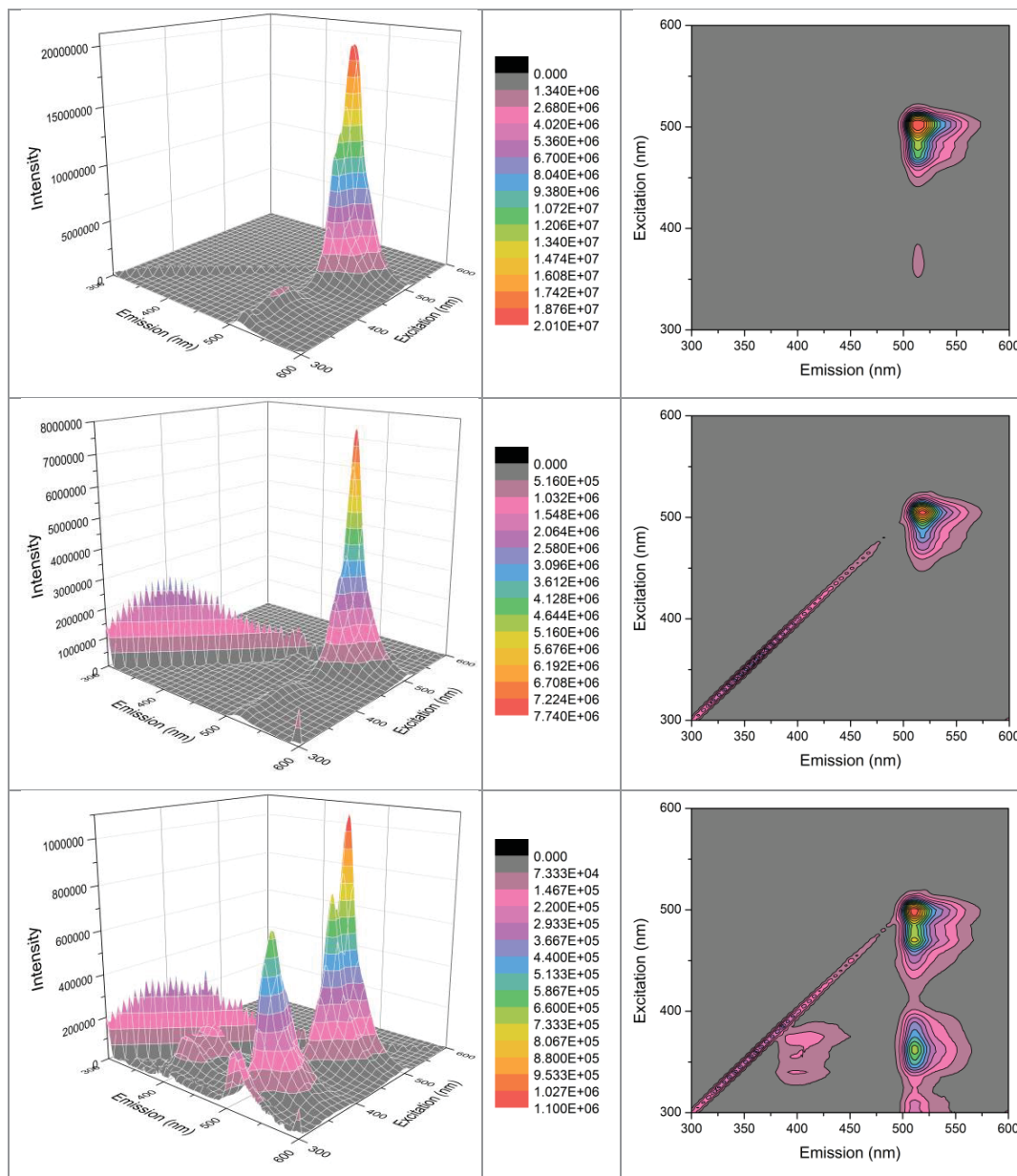


Figure 4.17 - 3D (left) and contour (right) plots of Cl-BODIPY in: chloroform (top); chlorobenzene (centre); and isopropyl alcohol (bottom)

The shape of the solvent was also considered, as some shapes may be favourable for aggregation of BODIPY, however, this was also found to not be solely responsible, based on the observation of significant emission in toluene compared to unobservable emission in chlorobenzene.

This behaviour is also observed for Benzoic/BODIPY, and may appear in other compounds, however, they are more visible in these compounds due to their relatively large quantum yields (see 4.2.1).

Looking at the data for 400 nm excitation across solvents, as shown in Figure 4.18, it is evident the $\lambda_{ex} \cong 380$ nm mode does appear in ethyl acetate also, however, its intensity is significantly lower than the Rayleigh emission band at 400 nm, and hence is not seen in the 3D or contour plot for Cl-BODIPY in ethyl acetate. Additionally, through comparison with the solvent data on the same plots, it is evident these emission bands do not occur due to impurities in solvent. Quantum yield calculations for both Cl-BODIPY and Benzoic/BODIPY were performed at $\lambda_{ex} = 470$ nm. From Figure 4.18 it is evident that this behaviour does not effect the emission band of interest (Maximum $\lambda_{em} \cong 510$ nm) and therefore this behaviour will not effect the calculation of integrated peak areas or fluorescence quantum yields, provided appropriate excitation wavelengths are chosen.

4.3 Time-resolved emission

Lifetime measurements were performed using TCSPC with a 320 or 380 nm picosecond pulsed LED-laser (Edinburgh Instruments, Edinburgh, Scotland). Lifetimes were recorded in a 100 ns time range using 8192 channels. The measurement was stopped when the number of photons in any one channel reached 10000 counts.

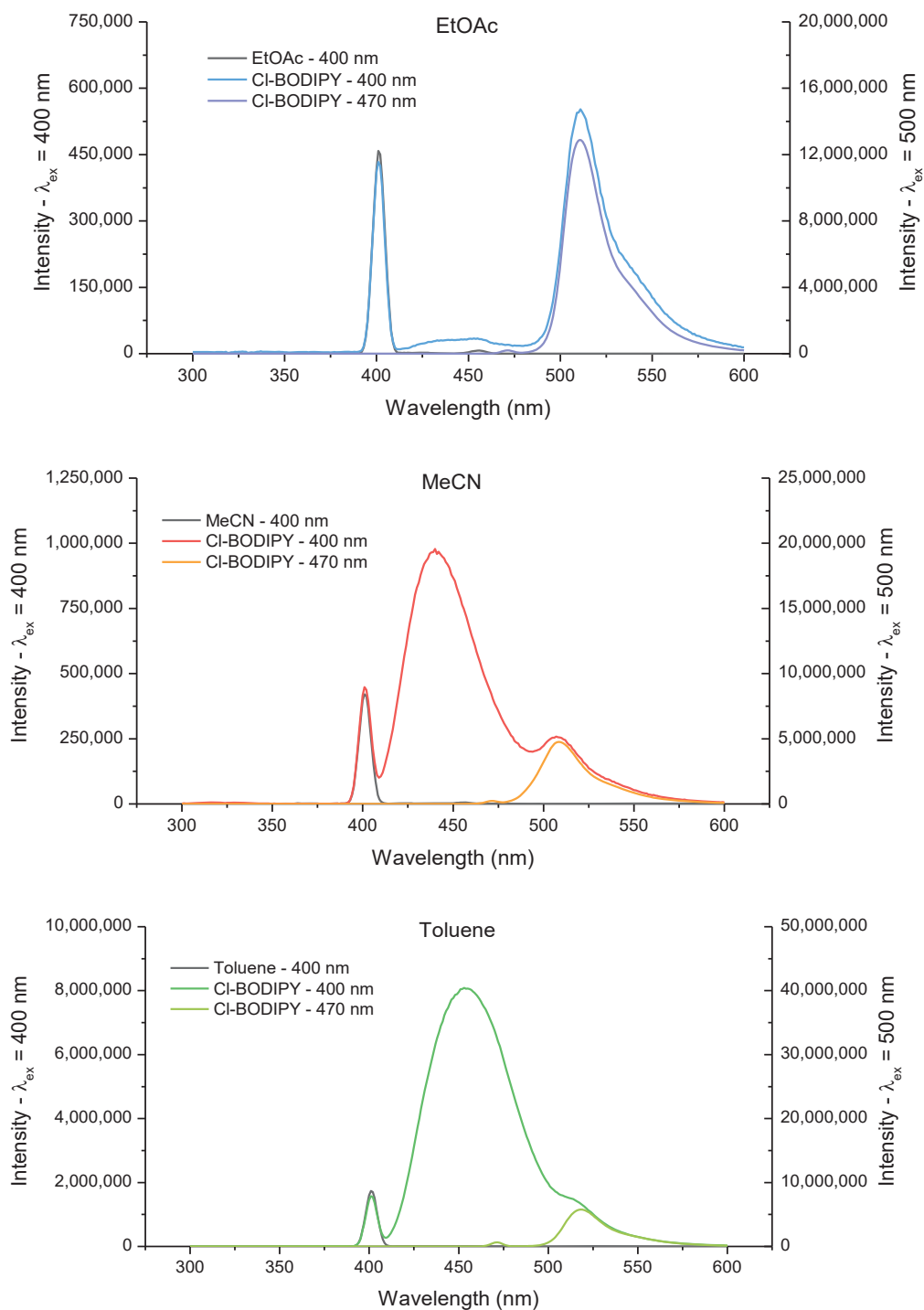


**Figure 4.18 - Excitation data for Cl-BODIPY in three solvents;
Data for $\lambda_{ex} = 500$ nm has been scaled to match λ_{em} at approximately 525 nm**

Table 4.4 - Lifetimes in ethyl acetate

	τ_0 (ns)	k_r ($10^8 s^{-1}$)	k_{nr} ($10^8 s^{-1}$)	E_{em} ($10^3 cm^{-1}$)
Cl-BODIPY	8.58	0.584 ± 0.003	0.581 ± 0.003	19.569
Aniline/BODIPY	2.62	0.099 ± 0.004	3.712 ± 0.004	23.866
1-naphthol/2xBODIPY	4.20	0.003 ± 0.002	2.377 ± 0.002	19.380
2-naphthol/2xBODIPY	4.22	0.002 ± 0.002	2.366 ± 0.002	19.157
1-naphthylamine/BODIPY	2.39	0.029 ± 0.004	4.156 ± 0.004	23.364
2-naphthylamine/BODIPY	2.39	0.104 ± 0.004	4.082 ± 0.004	23.419
2-aminoanthracene/BODIPY	3.17	0.041 ± 0.003	3.109 ± 0.003	22.422
9-phenanthrenol/BODIPY	2.45	0.002 ± 0.004	4.086 ± 0.004	19.157
1-hydroxypyrene/BODIPY	8.32	0.000 ± 0.001	1.202 ± 0.001	20.833
2-hydroxytriphenylene/BODIPY	4.28	0.013 ± 0.002	2.325 ± 0.002	20.080
HBC(<i>t</i> -Bu) ₅ OH/BODIPY	12.09	0.053 ± 0.008	0.774 ± 0.008	19.685
HPB(<i>t</i> -Bu) ₅ OH/BODIPY	1.63	0.049 ± 0.006	6.080 ± 0.006	20.243
Benzoic acid/BODIPY	7.11	0.794 ± 0.001	0.612 ± 0.001	19.569

Table 4.5 - Lifetimes in acetonitrile

	τ_0 (ns)	k_r ($10^8 s^{-1}$)	k_{nr} ($10^8 s^{-1}$)	E_{em} ($10^3 cm^{-1}$)
Cl-BODIPY	8.97	0.498 ± 0.003	0.617 ± 0.003	19.608
1-naphthol/2xBODIPY	4.50	0.002 ± 0.002	2.222 ± 0.002	19.305
2-naphthol/BODIPY	5.34	0.001 ± 0.002	1.873 ± 0.002	20.284
2-naphthol/2xBODIPY	4.48	0.032 ± 0.002	2.202 ± 0.002	19.305
2-hydroxytriphenylene/BODIPY	4.55	0.001 ± 0.002	2.199 ± 0.002	20.121

Table 4.6 - Lifetimes in toluene

	τ_0 (ns)	k_r ($10^8 s^{-1}$)	k_{nr} ($10^8 s^{-1}$)	E_{em} ($10^3 cm^{-1}$)
Cl-BODIPY	7.83	0.563 ± 0.003	0.715 ± 0.003	19.268
1-naphthol/2xBODIPY	3.81	0.117 ± 0.003	2.507 ± 0.003	19.231
2-naphthol/BODIPY	4.21	1.049 ± 0.002	1.324 ± 0.002	19.881
2-naphthol/2xBODIPY	3.66	0.004 ± 0.003	2.730 ± 0.003	19.048
2-hydroxytriphenylene/BODIPY	2.42	1.241 ± 0.004	2.895 ± 0.004	19.920

Measured lifetimes (τ_0), as well as radiative (k_r) and non-radiative (k_{nr}) rate constants and emission maxima energies (E_{em}) are summarised in Table 4.4 (ethyl acetate), Table 4.5 (acetonitrile), and Table 4.6 (toluene). All lifetimes are given assuming mono-exponential decay, except for that for HPB(*t*-Bu)₅OH/BODIPY, which is bi-exponential. Rate constants were determined using the method of Caspar and Meyer.⁹⁷ Radiative and non-radiative rate constants are calculated according to (4-7) and (4-8), where $\Phi_{F(X)}$ was calculated previously in (4-6).

$$\tau_0 = (k_r + k_{nr})^{-1} \quad (4-7)$$

$$\Phi_{F(X)} = k_r \tau_0 \quad (4-8)$$

The energy gap law relates the excited-state, non-radiative decay rate to the emission energy.⁹⁷ By plotting $\ln k_{nr}$ against the emission energy (E_{em}), it is hoped that a relationship will appear between the size and nature of the substituted dipyrin analogue.

As evident in Figure 4.19, there is no obvious trend when all data is included, with the amine-functionalised structures and those with non-hydroxyl functionalised analogues also not fitting an overall trend. This is logical, as functional group has a significant effect on the properties of the compounds. Treating the amine compounds separately, it is evident that the one- and two-ring compounds appear to fit a linear negative trend, however, this does not apply for the 2-aminoanthracene/BODIPY compound. Due to the limited size of the dataset, further conclusions about the nature of the relationship between k_{nr} and E_{em} are unable to be made. The same restrictions apply with the larger analogue structures, Cl-BODIPY, and Benzoic/BODIPY also.

Looking at the data for hydroxyl functionalised analogues (Figure 4.20), however, trends are visible for both monosubstituted and disubstituted data. Overall, the two datasets have very similar, negative linear relationships, however they have been treated separately as the presence of additional dipyrin molecules is expected to influence the compounds' properties. Additionally, the linear fit for the monosubstituted data has been calculated excluding the data point for 2-naphthol/1xBODIPY in toluene, due to it appearing to be a significant outlier. These trends show that the energy gap law applies for hydroxyl-BODIPY functionalised polycyclic aromatic hydrocarbons.

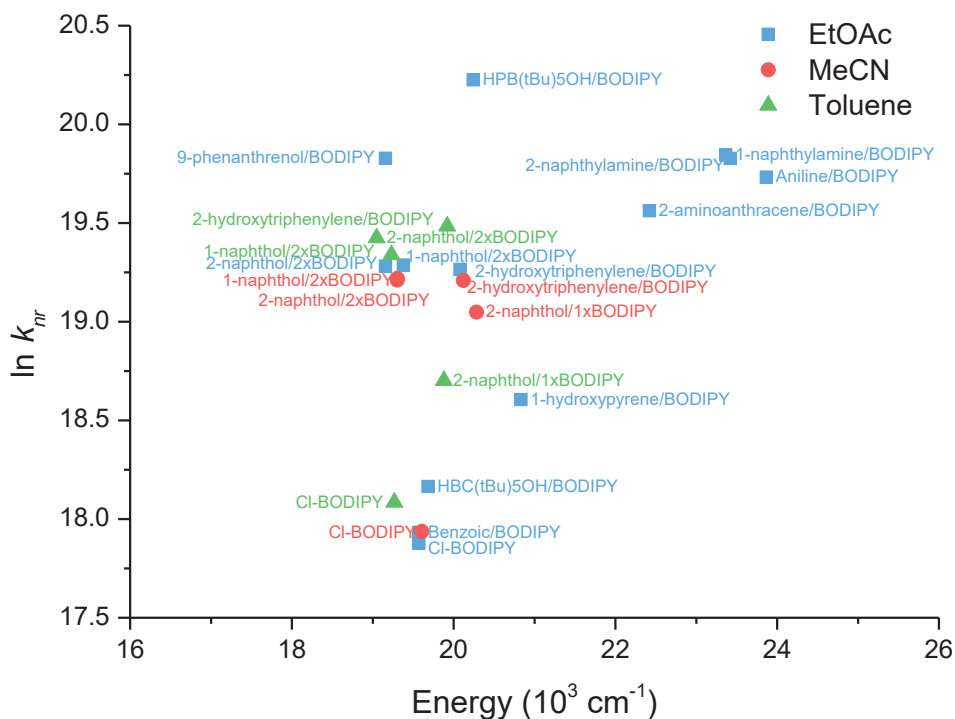


Figure 4.19 - $\ln k_{nr}$ vs E_{em} for all compounds

Based on the relationship discussed in 3.4.2(d) wherein the size of the HOMO-LUMO gap can be related to the amount of benzenoid character an analogue contains, it would follow that similar relationships may be observed between the amount of benzenoid character and the energy gap law plot.

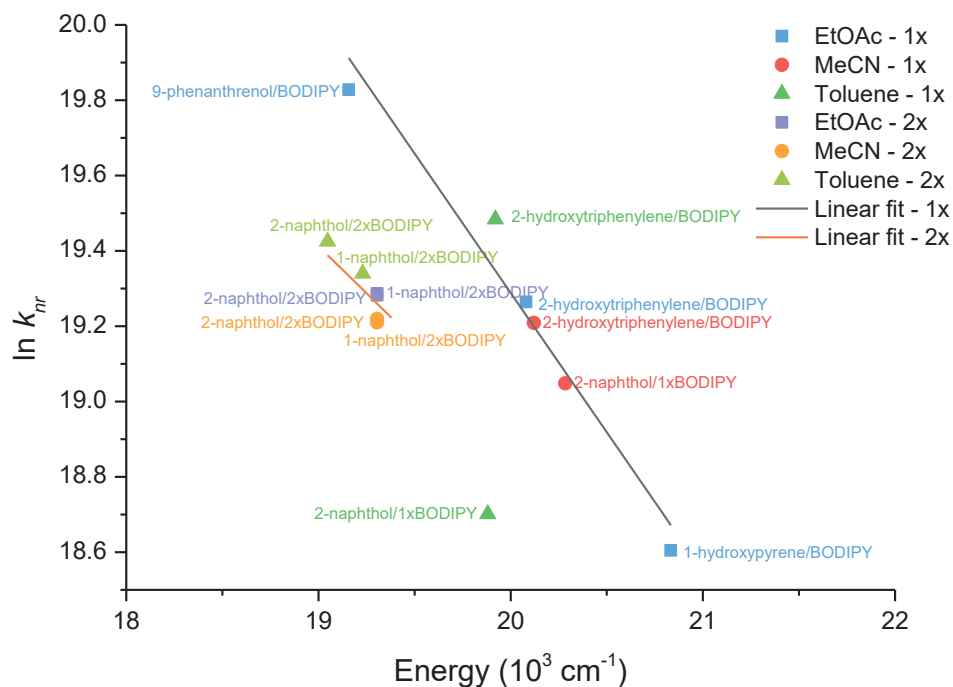


Figure 4.20 - $\ln k_{nr}$ vs E_{em} for hydroxyl containing compounds; Data has been separated between mono- (1x) and d- (2x) substituted analogues

Examining the energy gap law plot for hydroxyl functionalised analogues in Figure 4.20, it would be expected that those analogues having more benzenoid character would be located in the upper left portion of the plot (lower energy, higher $\ln k_{nr}$), whilst those with less benzenoid character would appear in the lower right portion (i.e. higher energy, lower $\ln k_{nr}$). This holds for most of the monosubstituted compounds, as hydroxytriphenylene has more benzenoid character than naphthol, which in turn is more benzenoid than hydroxypyrene, however, the data shown for 9-phenanthrenol/BODIPY in ethyl acetate does not fit this trend. More data would be required to determine whether 9-phenanthrenol/BODIPY is an outlier, or whether the relationship between benzenoid character and the energy gap law does not hold.

4.4 Infrared spectroscopy

Experimental infrared (IR) spectra of functionalised small molecules were collected using a Thermofisher Scientific Nicolet 5700 equipped with a Germanium crystal Smart iTR™ Attenuated Total Reflectance (ATR) sampling accessory.

DFT calculations were performed on both 1-hydroxypyrene and 1-hydroxypyrene/BODIPY to obtain calculated IR spectra. Geometry optimisations were performed using B3LYP/DZP, whilst frequency calculations were performed using PBE/DZP.

(a) Accuracy of computational methods

Comparing calculated and experimental vibrational modes shown in Figure 4.21 and Figure 4.22, it can be seen that the overall agreement is very good. Calculated vibrational modes here are represented by Lorentzian functions of 1 cm^{-1} width.

Additionally, vibrational frequencies have been scaled to better match experimental frequencies (PBE/DZP = 0.986).

While vibrational frequencies agree to within a few wavenumbers, they do not all agree in terms of relative vibrational intensity. This is not a concern, as the positions of vibrational modes are of much greater interest than relative intensities, as experimental infrared (IR) intensities can be effected by a number of factors which are not accounted for in a computational model.

The agreement between computational and experimental spectra provides confirmation that the model is reasonable, and that results obtained using the model should be expandable to provide insight for compounds which are too complex to model using DFT methods.

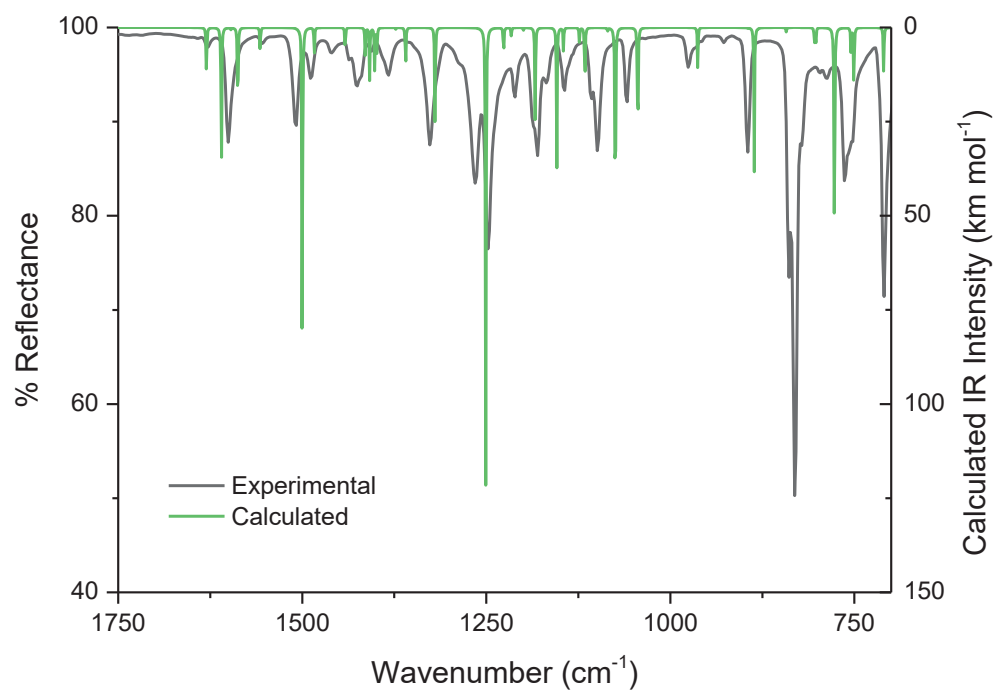


Figure 4.21 - Comparison between calculated and experimental IR spectra of 1-hydroxypyrene

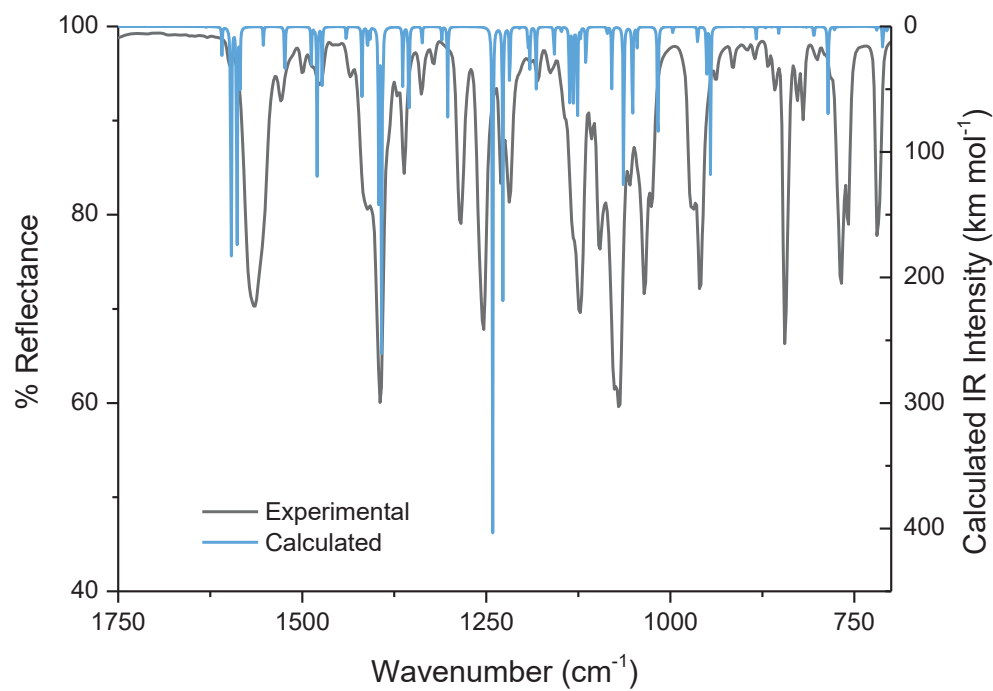


Figure 4.22 - Comparison between calculated and experimental IR spectra of 1-hydroxypyrene/BODIPY

(b) Effect of BODIPY-functionalisation on IR spectra

The influence of BODIPY-functionalisation on vibrational modes can be seen in the experimental IR spectra of 1-hydroxypyrene and 1-hydroxypyrene/BODIPY shown in Figure 4.23. As expected, the O-H vibrational mode at 3275 cm^{-1} in 1-hydroxypyrene has disappeared upon BODIPY functionalisation, confirming functionalisation has occurred in the expected position. Looking at the inset, it can be seen there are a number of modes which have appeared in the IR spectrum upon functionalisation with BODIPY. To gain further understanding of these vibrational modes, and to assign the modes to the different regions of the molecule, computational methods are employed.

As shown already, computational IR spectra provide a good approximation for the experimental spectra, and as such, can be used to assign the vibrational modes which appear upon BODIPY functionalisation.

In order to confirm that new modes are due to BODIPY functionalisation, two systems are analysed to confirm consistencies between the IR spectra. The analogues used for this are 1-hydroxypyrene and $\text{HBC}(t\text{-Bu})_5\text{OH}$, with their computational IR spectra shown in Figure 4.24 and Figure 4.25 respectively.

The spectra are only shown for the selected region as there is very little IR activity outside of this region with the exception of the O-H vibrational mode at approximately 3200 cm^{-1} . $\text{HBC}(t\text{-Bu})_5\text{OH}$ is utilised here due to its large size being shown in 3.1 to be a good model for the behaviour of graphene nanoribbon structures, leading these results to be extendable to experimental graphene nanoribbon systems.

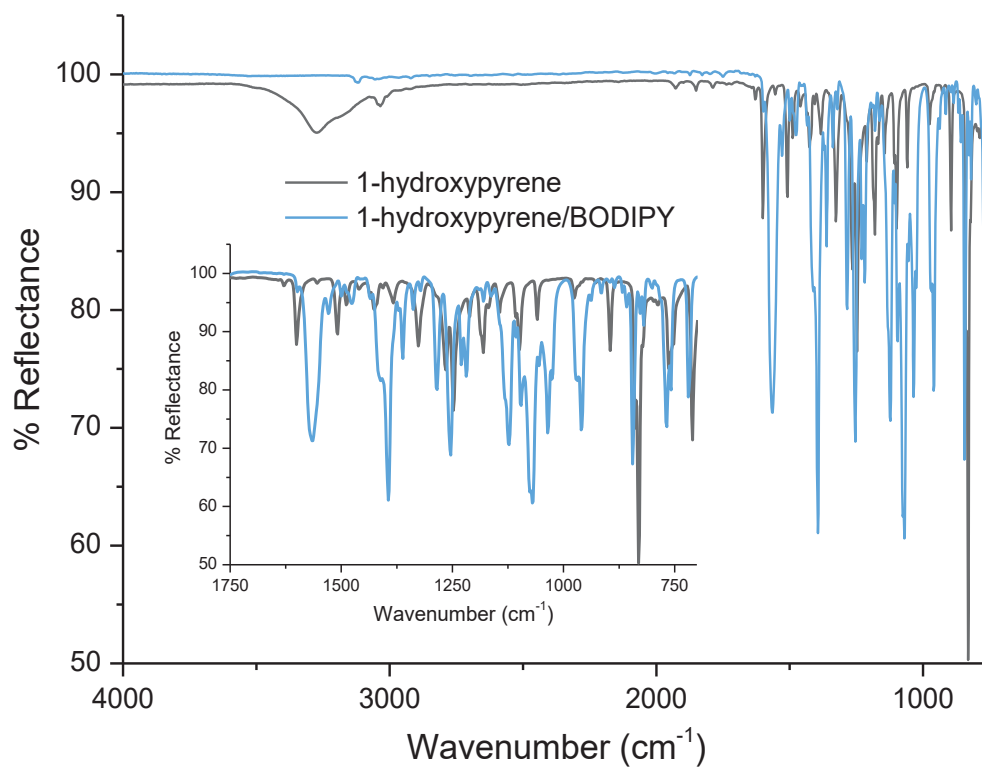


Figure 4.23 - Experimental IR spectra of 1-hydroxypyrene and 1-hydroxypyrene/BODIPY

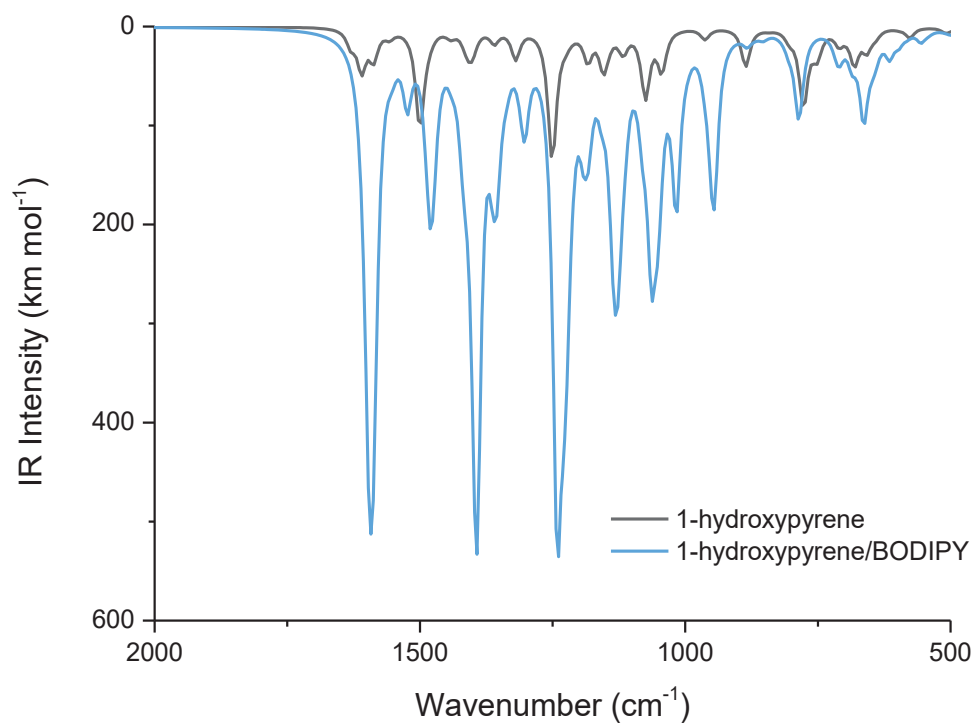


Figure 4.24 - Calculated IR spectra of 1-hydroxypyrene and 1-hydroxypyrene/BODIPY

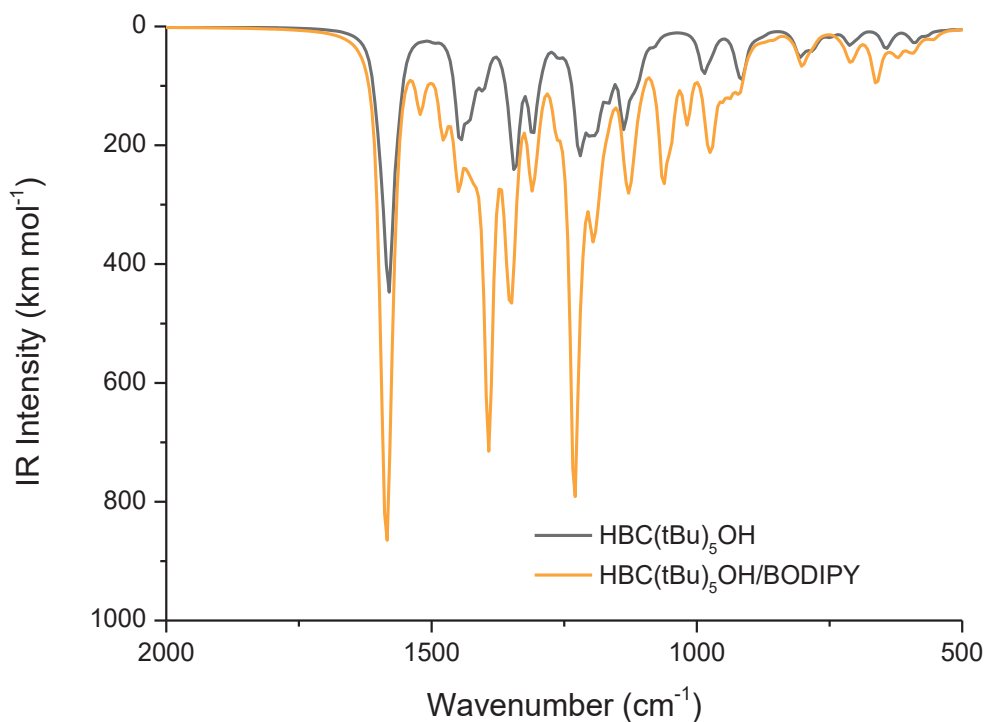
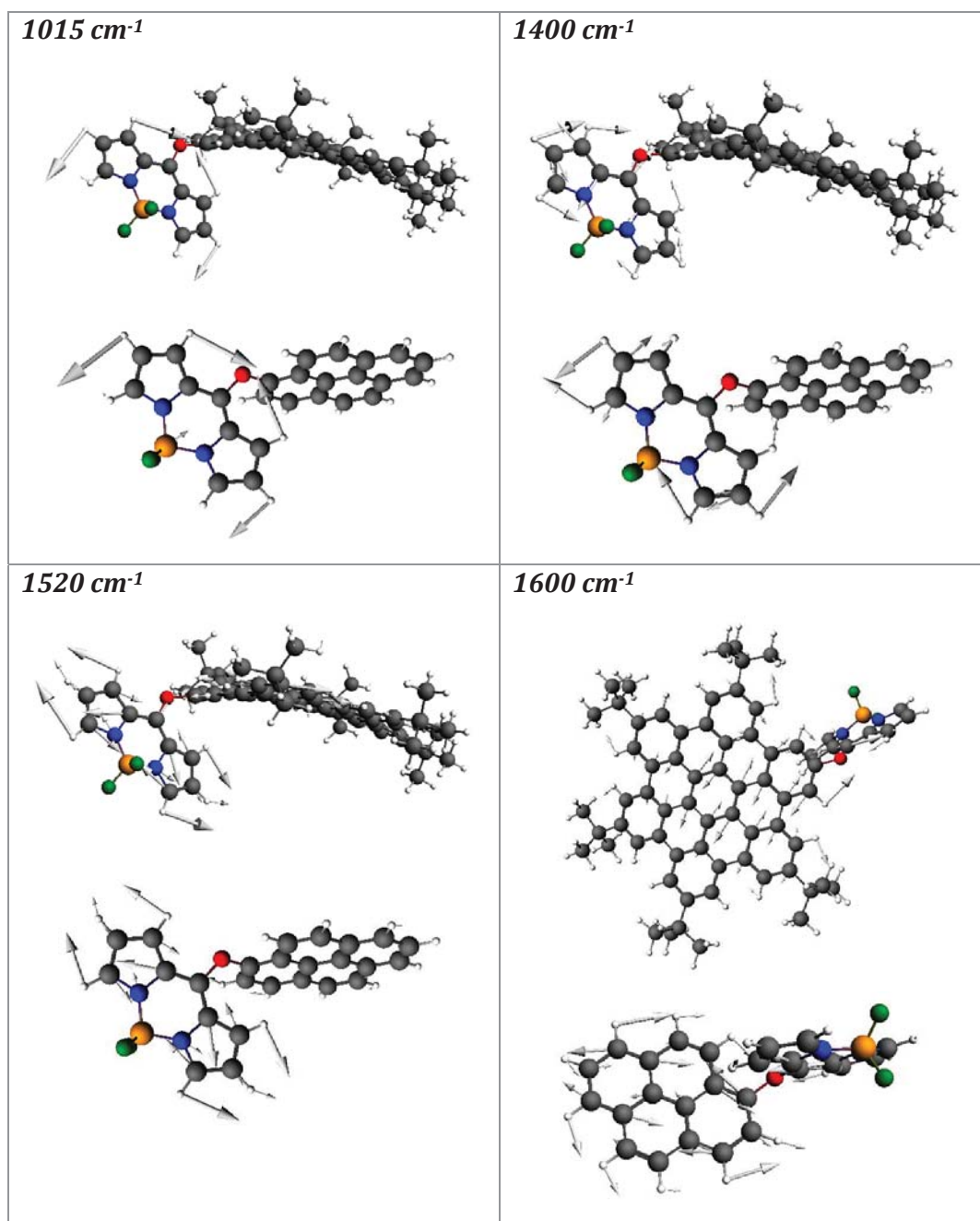


Figure 4.25 - Calculated IR spectra of HBC(*t*-Bu)₅OH and HBC(*t*-Bu)₅OH/BODIPY

The vibrational mode frequencies have been scaled using the appropriate factor (PBE/DZP = 0.986), and calculated vibrational modes have been artificially widened using Lorentzian functions with widths of 20 cm⁻¹.

Looking at both spectra, there are three vibrational modes of large intensity, and a few of lower intensity, which can be analysed and assigned. The vibrations associated with these modes are shown in Figure 4.26.

The large peak at approximately 1600 cm⁻¹ is the G mode, and whilst this appears in calculated IR spectra, it is not expected to occur with significant intensity in experimental IR spectra of graphene nanoribbons due to the largely symmetrical nature of the larger graphene lattice. Changes to the lattice, such as modifications of the basal plane and the presence of edges, can change this, however, BODIPY specific modes would have much more significant changes in intensity upon functionalisation.



**Figure 4.26 - Vibrational modes - BODIPY functionalisation;
 In each grid: top - HBC(*t*-Bu)5OH/BODIPY; bottom - 1-hydroxypyrene/BODIPY.
 Figures have been oriented to show the atoms with largest displacements in the plane**

The large vibrational mode just below 1250 cm^{-1} is attributed to both the BODIPY and the aromatic hydrocarbon, and is a ring breathing mode, however, as it is present at low intensity in the non-functionalised analogues, it is unable to be used as a mode to characterise BODIPY functionalisation.

There are a number of vibrational modes of varying intensities which can be attributed to BODIPY only at (approximately) 1015 cm^{-1} , 1400 cm^{-1} , and 1520 cm^{-1} , with modes at 650 cm^{-1} and 1480 cm^{-1} also being attributable, but also near enough to other vibrational modes that they may not be distinguishable experimentally.

Experimentally (Figure 4.23), intense modes are seen at 1035 cm^{-1} and 1395 cm^{-1} for BODIPY-functionalised 1-hydroxypyrene, with a low intensity mode also seen at 1530 cm^{-1} . In both computational and experimental spectra, these three modes occur independently of modes attributed to the non-functionalised analogue. From this, these three modes should provide information on BODIPY functionalisation of any polycyclic aromatic material, including graphene nanoribbons.

(c) Analysis of vibrational spectra

Continuing from the mode assignments shown in 4.4(b), all vibrational modes can be assigned as belonging to one or more components of the molecule structure. The mode assignments for 1-hydroxypyrene/BODIPY are shown in Figure 4.27. The vibrational modes are scaled using the appropriate factor (PBE/DZP = 0.986), and in this case are plotted without any artificial widening.

In this case, the vibrational mode can be assigned as belonging purely or mostly to BODIPY or to pyrene, and also assigned as being across both parts of the structure. It can be seen that there are some distinct regions of purely pyrene behaviour as well as purely BODIPY behaviour.

There are also regions of vibrational modes attributed to the whole molecule. It should be noted that, as expected, regions of pure BODIPY and whole molecule vibrations are in agreement with the characteristic modes attributed to BODIPY functionalisation in (b).

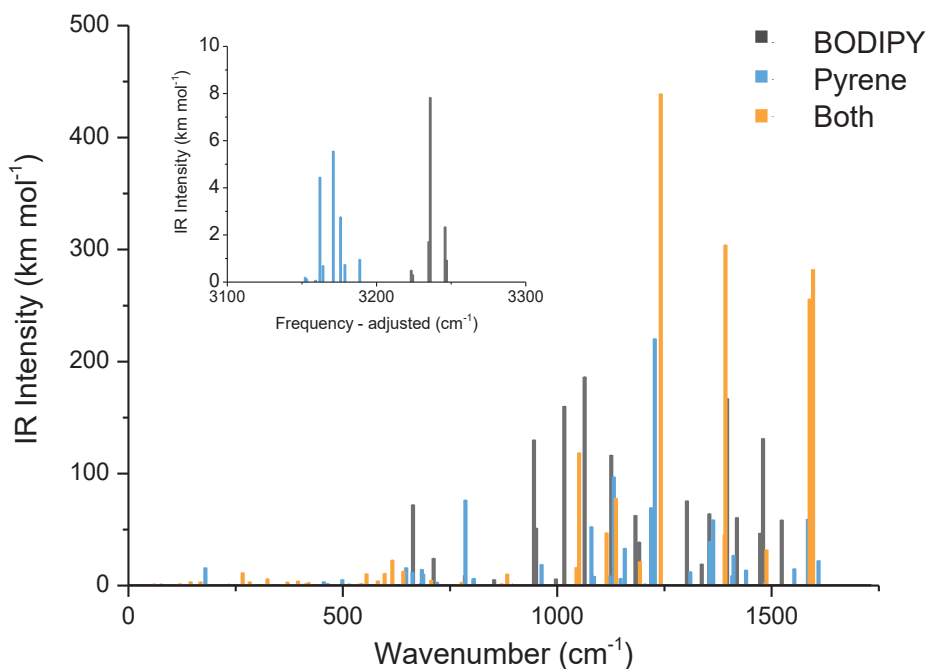


Figure 4.27 - Calculated IR spectrum for 1-hydroxypyrene/BODIPY with assigned vibrational modes

This mode assignment method has also been applied to HBC(*t-Bu*)₅OH/BODIPY as shown in Figure 4.28. In this case, the presence of tertiary-butyl (*t-Bu*) functional groups make the assignment more complex and leads to a potential seven characterisations, as opposed to three for the case of 1-hydroxypyrene/BODIPY.

Because graphene nanoribbons are not expected to contain edge-functional groups in such high proportion, those characterisations including *t-Bu* with either BODIPY or the aromatic (HBC) part of the molecule have been coloured similarly to those without *t-Bu* influence.

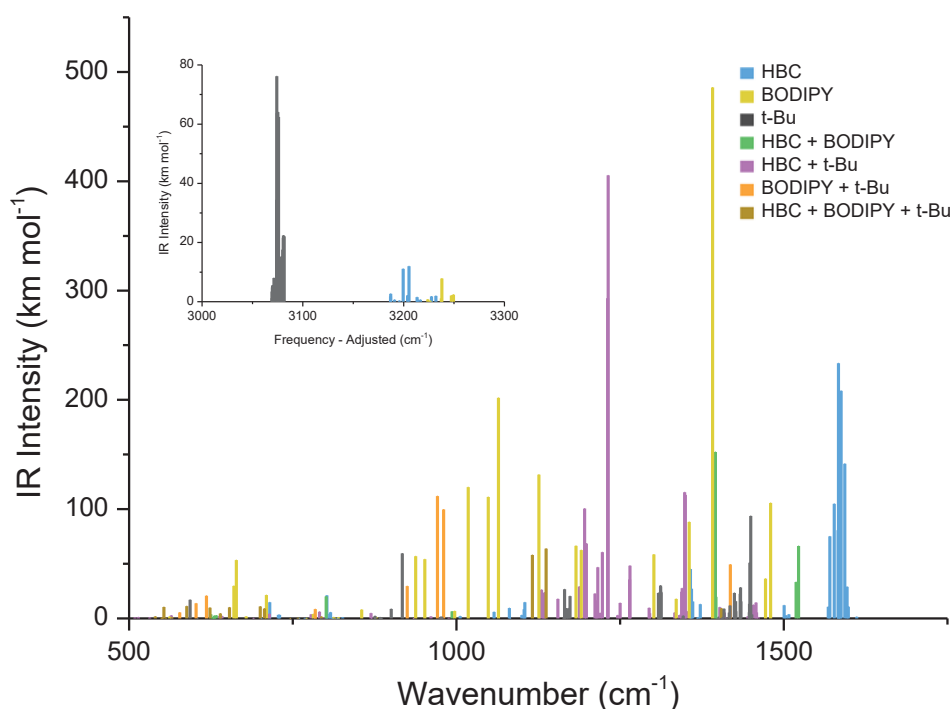


Figure 4.28 - Calculated IR spectrum for HBC(*t*-Bu)5OH/BODIPY with assigned vibrational modes

As with 1-hydroxypyrene/BODIPY, regions can be seen in which vibrational modes are grouped with similarly assigned modes. These again are in agreement with the characteristic BODIPY modes discussed in (b), further strengthening the case for those selected modes being used to characterise BODIPY functionalisation.

4.5 Raman spectroscopy

Analysis using Raman spectroscopy was attempted on Cl-BODIPY and 1-hydroxypyrene/BODIPY. These compounds were chosen due to their respective emission quantum yields being the largest and smallest of the compounds studied. As Raman measurements are highly sensitive to emission, the two selected compounds were used to determine whether Raman measurements would be possible for either all, some, or none of the functionalised BODIPY compounds synthesised.

Whilst both compounds are solvatochromic, 1-hydroxypyrene/BODIPY has an absorption maxima at approximately 455 nm, whilst Cl-BODIPY has absorption maxima at approximately 500 nm, with a shoulder at approximately 480 nm. As such, excitation wavelengths of both 488 nm and 532 nm were selected for Raman studies. Raman measurements performed on the pure, solid sample were found to be dominated by emission at 532 nm excitation. Because of this, surface-enhanced Raman spectroscopy (SERS) measurements were attempted. 0.5 mL silver nanoparticles were combined with 0.25 mL 40 mM aqueous KNO_3 and 0.25 mL of approximately 10^{-7} M BODIPY sample in water (prepared via phase transfer dilutions beginning with 10^{-4} M dye in IPA). SERS measurements at 532 nm excitation showed potential emission quenching, but no Raman peaks attributable to the dye molecules. This indicates that either the dye concentration or excitation wavelength were not optimal. SERS measurements at 488 nm excitation had large observable emission, indicating the dye molecules were not adhering to the nanoparticles properly, ruling out this method for obtaining Raman spectra of these materials.

From attempts at Raman measurements, it was evident that the emission of these dye molecules, even those with very low quantum yields such as 1-hydroxypyrene/BODIPY, were too great for Raman spectroscopy to be utilised.

Chapter 5. Dipyrrin-functionalised graphene nanoribbons

The analysis and characterisation of functionalised graphene nanoribbons is difficult for many reasons. The large relaxation time of these large structures disqualifies the use of NMR characterisation methods, while the broad-spectrum absorption of graphene nanoribbons makes absorption and emission spectroscopy difficult. Additionally, depending on the proportion of edge functionalisation, bands indicating the presence of dipyrrin may be overwhelmed by those associated with graphene. Infrared and Raman spectroscopy methods allow for the characterisation of such large materials, however, issues with the size of the functionalised analogue are expected to still be present. Studies have shown that the functionalisation of graphene nanoribbons can be determined using Raman through shifting positions of D and G modes.⁵

Results from 4.4 show that dipyrrin functionalisation of graphene analogues caused an increase in the number of vibrational modes observed in both computational and experimental IR spectra. From this, it is expected that dipyrrin functionalisation of graphene nanoribbons should also cause an increase in the number of modes.

Infrared spectroscopy is a useful tool for determining whether graphene nanoribbons have been functionalised, however, it is not well understood enough for graphene nanoribbons to be able to quantify the position of functionalisation, i.e. whether the functionalisation has occurred at the edges, as is desired in this study, or whether the interactions have occurred on the basal plane.

Raman spectroscopy of graphene nanoribbons, whilst difficult for low quantities of compound, is well understood, and the effects of edge and basal plane functionalisation can be distinguished using Raman techniques. Edge functionalisation has been shown to cause slight shifts in the position of the G band, however, typically with edge-functionalised graphene nanoribbons the overall shape of the Raman spectrum remains relatively unchanged from that of the original nanoribbon. In contrast, modification of the basal plane would lead to changes in the intensity of disorder-induced modes such as the D mode.

Overall, infrared spectroscopy is used to confirm functionalisation has occurred, while Raman spectroscopy is used to determine where it has occurred. The combination of these two techniques allows for a more complete characterisation than either of the techniques alone.

All graphene nanoribbons were cut in air and transferred to dry dichloromethane prior to reactions being performed. Prior to functionalisation, each batch of nanoribbons was split between three reaction vials, to give “control” (C-GNRs), “BODIPY control” (BC-GNRs) and “functionalised” graphene nanoribbons (F-GNRs). The reaction conditions for each type of nanoribbons are given in Table 5.1. All nanoribbon samples were sonicated for the same time periods to overcome potential sonication induced effects on the ribbons.

Table 5.1 – General reaction conditions for GNR samples

	Cl-BODIPY added	DIPEA added
C-GNR	✗	✗
BC-GNR	✓	✗
F-GNR	✓	✓

5.1 Infrared spectroscopy

Infrared spectroscopy of graphene nanoribbons was performed using a Nicolet 6700 FT-IR spectrometry with microscope attachment was used to perform absorption measurement in a reflection geometry. A mercury-cadmium-telluride (type a) (MCT-a) detector was used in conjunction with a KBr beam splitter. Room temperature collection was used, with a sample spot size of $\sim 20 \times 20 \mu\text{m}$.

IR spectra of a batch of graphene nanoribbons are shown in Figure 5.1 and Figure 5.2. It is evident there has been significant changes in the IR spectra between C-GNR and F-GNR. These samples exhibit IR spectra more closely related to aggregated graphene nanoribbons, however, this is not of concern, as it is likely this has happened due to insufficient sonication of both samples prior to IR sample preparation as opposed to during the functionalisation reaction. In Figure 5.1 benzene fingers, aromatic and ring-stretching substituent modes,⁹⁸⁻⁹⁹ are evident in the C-GNR spectrum, but have been distorted in that of F-GNR, indicating substitution affecting these bands. Figure 5.2 shows a significant increase in the number of vibrational bands from C-GNR to F-GNR, further indicating functionalisation with BODIPY was successful. Additionally, characteristic modes identified in section 4.4(b) are evident in the spectrum of F-GNR, further indicating successful functionalisation.

A concern with the functionalisation process is the potential for unreacted BODIPY to interact non-covalently with the graphene nanoribbons, and therefore not be removed during the purification process. To determine if this was occurring, C-GNR spectra were compared to those for BC-GNR, as shown in Figure 5.3. It is evident that, excluding backgrounds, the two spectra are very similar.

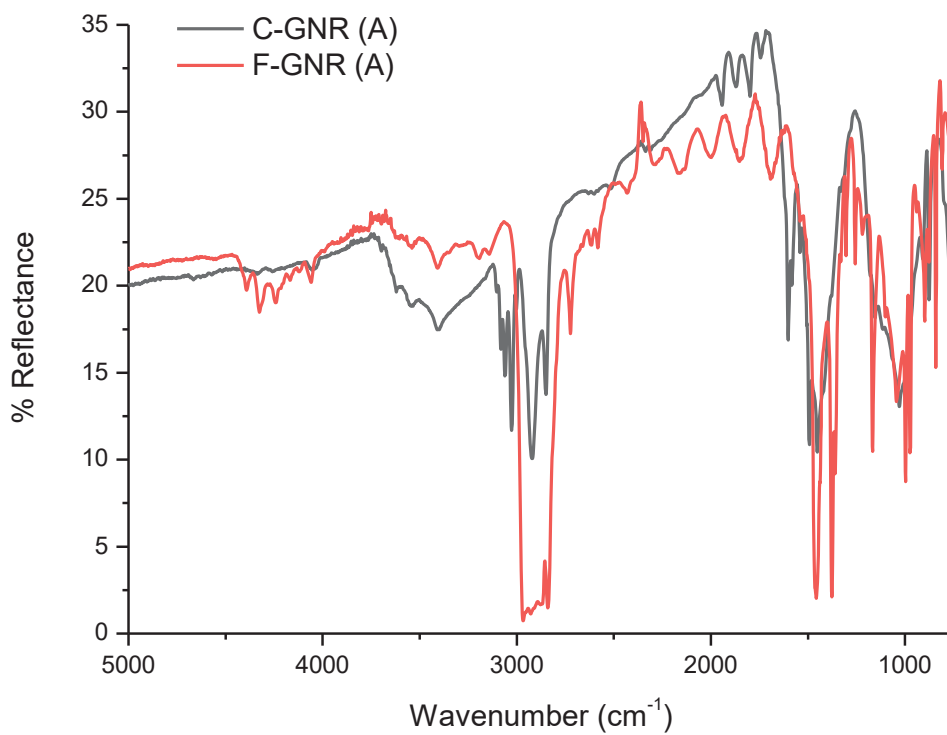


Figure 5.1 - IR spectra of C-GNR and F-GNR for a batch of graphene nanoribbons

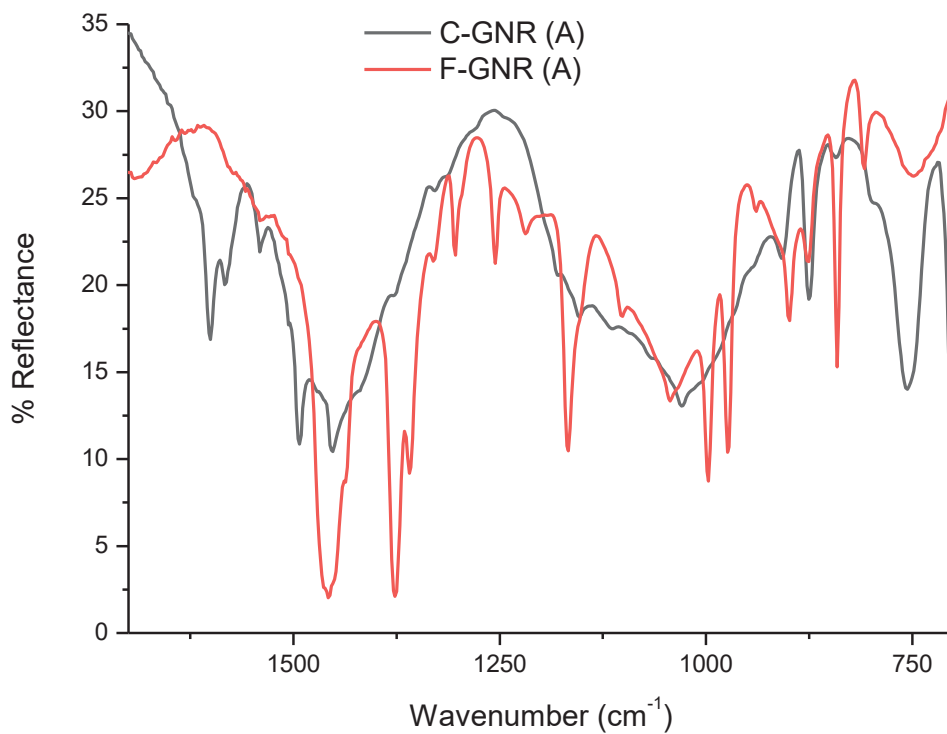


Figure 5.2 - IR spectra of C-GNR and F-GNR for a batch of graphene nanoribbons; zoomed to show primary region of interest

As demonstrated by Figure 5.2, the influence of BODIPY on IR spectra is significant, therefore it can be assumed that BC-GNR contains no unreacted BODIPY or non-covalently interacting BODIPY.

The infrared spectral analysis of GNRs shows promise as a useful characterisation method to determine whether functionalisation has occurred, however, the extent of functionalisation is not currently obtainable through this method.

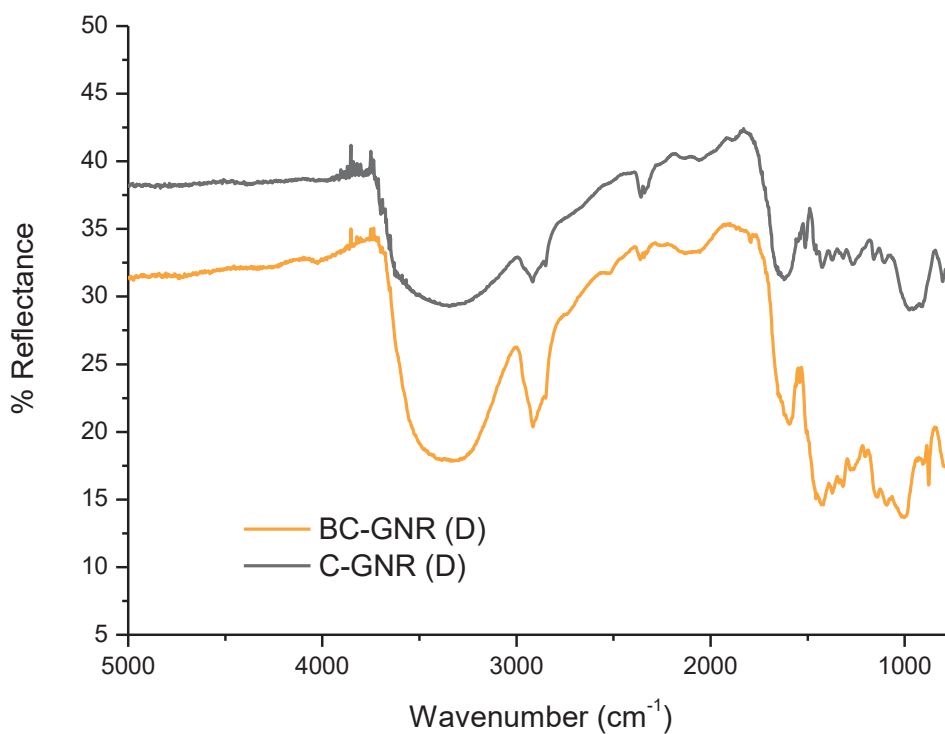


Figure 5.3 - Comparison between C-GNR and BC-GNR

5.2 Raman spectroscopy

Raman spectra were collected on a custom-Built Raman microscope, based on an Olympus IX70 inverted fluorescence microscope, utilising OptiGrate volume Bragg gratings as beam-splitters and notch filters. An objective with $NA = 0.65$ and $40\times$ magnification was used to focus the incident light (532 nm, ≈ 2 mW at the

sample) and to collect scattered radiation. A Princeton Instruments FERGIE spectrograph system was used for dispersion and detection.

Samples of graphene nanoribbons were prepared by pipetting 50 μ L of GNRs suspended in dichloromethane onto glass cover slips and allowing to dry. All spectra were acquired via the summation of ten 60 second exposures of the sample to ensure spectra could be compared with one another with ease. Spectra of the cover slip only were obtained at the same focal length for each sample to determine substrate influence on spectra. There was found to be no substrate bands present within the region of interest for graphene nanoribbons, however, the substrate did cause a broad background. Backgrounds were removed using an asymmetric least squares method,¹⁰⁰ which use the spectrum itself to iteratively establish a baseline.¹⁰¹ Through controlling parameters, baselines can be generated which sit below the original spectrum, which is desirable in the context of Raman spectroscopy.¹⁰²⁻¹⁰⁵

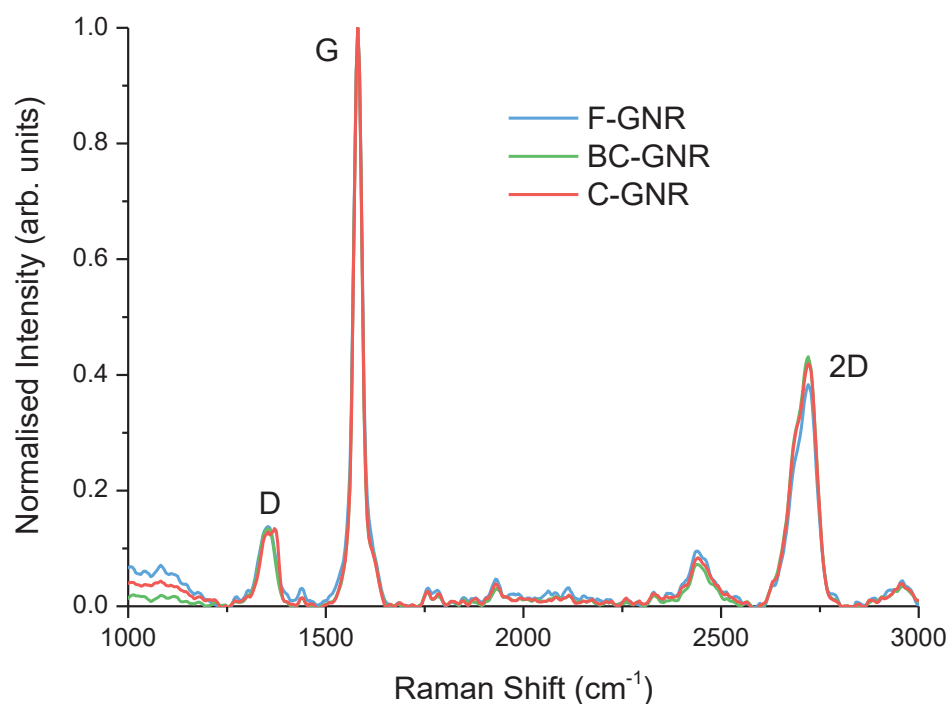


Figure 5.4 – Normalised Raman spectra of graphene nanoribbons

Figure 5.4 shows the Raman spectra of each sample type for a batch of nanoribbons. These spectra have been normalised to have a G-mode intensity of 1. Looking at the defect-induced D mode, there are no significant changes in relative intensity between the three samples. This indicates that no changes have occurred to the basal plane, and that any functionalisation occurring in the F-GNR sample must have taken place at the nanoribbon edges. As mentioned previously, functionalisation at the edges can lead to slight shifts in the G mode position, however, due to the resolution of these spectra, any such changes would not be observed. The 2D mode is sensitive to the number of layers of graphene. From the spectra, it is evident the number of layers is similar for each spectrum.

Chapter 6. Summary and Perspectives

A novel series of dipyrin-functionalised small molecule compounds have been synthesised via nucleophilic aromatic substitution. This library of compounds has been further analysed using spectroscopic and computational methods. Absorption spectroscopy showed large molar absorptivity coefficients for all compounds, with those functionalised via hydroxyl substitution having generally larger coefficients than those functionalised via amine groups. Time-dependent DFT calculations were used to analyse the absorption spectra, and to quantify both inter- and intramolecular interactions, in particular those observed in disubstituted aromatic compounds.

The emission quantum yields of these BODIPY functionalised small molecule compounds were found to vary with the group via which functionalisation was performed, i.e. hydroxyl or amine, the size of the functional group, and the solvent in which measurements were performed. This behaviour was found to fit the energy gap law in the case of hydroxyl functionalised compounds, however, the size of the data set was not sufficient to determine if this relationship also holds for those functionalised via amine groups.

Spectroscopic analyses were performed on BODIPY functionalised small molecule compounds to determine the effect of BODIPY functionalisation on vibrational spectra. Although both infrared and Raman spectroscopy methods were investigated, it was found that the inherent emission associated with BODIPY compounds was too significant for Raman measurements. Experimental infrared spectra showed a significant increase in the number of IR-active vibrational modes observed upon functionalisation. Computational methods were used to further

characterise these vibrations, and to isolate characteristic vibrational modes corresponding to BODIPY functionalisation.

The edge modification of graphene nanoribbons has been investigated through functionalisation with dipyrins. Infrared spectroscopy indicated that graphene nanoribbons were successfully functionalised via the same method as small molecule analogue. This was confirmed due to an increase in the number of bands observed, and further confirmed by the appearance of bands characteristic of BODIPY functionalisation in small molecule systems. Raman spectroscopy shows functionalisation occurred at the graphene edges due to no significant changes being observed in the disorder induced D mode, indicating the basal plane has not been disturbed.

The combination of infrared and Raman spectroscopy has been shown to be a useful tool in the determination of graphene nanoribbon functionalisation, with infrared spectroscopy providing information on the success of functionalisation, and Raman providing information on where functionalisation is occurring.

The BODIPY-functionalised graphene nanoribbons prepared in this study have significant potential. Additional chemical modifications could be performed via the BF_2 group of the BODIPY, allowing for specific functionalities to be added to the graphene nanoribbons. Given the straightforward preparation of BODIPY functionalised graphene nanoribbons, this may provide an alternate pathway for functionalities which are not able to easily functionalise graphene directly. This method could prove a useful route for tuning the graphene nanoribbon properties for specific applications.

Furthermore, the functionalised nanoribbons could be further studied to determine their potential in applications such as solar energy, sensors, or energy storage devices. Through the control of edge functionality, control over stacking interactions can be achieved. This leads to the potential to make hybrids with other materials, such as those commonly used in solar cells.

Bibliography

1. Baldoni, M.; Sgamellotti, A.; Mercuri, F., Electronic properties and stability of graphene nanoribbons: An interpretation based on Clar sextet theory. *Chemical Physics Letters* **2008**, *464* (4–6), 202-207.
2. Dubois, S. M. M.; Lopez-Bezanilla, A.; Cresti, A.; Triozon, F.; Biel, B.; Charlier, J.-C.; Roche, S., Quantum Transport in Graphene Nanoribbons: Effects of Edge Reconstruction and Chemical Reactivity. *ACS Nano* **2010**, *4* (4), 1971-1976.
3. Ruffieux, P.; Cai, J.; Plumb, N. C.; Patthey, L.; Prezzi, D.; Ferretti, A.; Molinari, E.; Feng, X.; Müllen, K.; Pignedoli, C. A.; Fasel, R., Electronic Structure of Atomically Precise Graphene Nanoribbons. *ACS Nano* **2012**, *6* (8), 6930-6935.
4. Tour, J. M. K., D.V.; Higginbotham, A.L.; Dimiev, A.; Siniskii, A.; Lomeda, J.R.; Price, B.K., Longitudinal unzipping of carbon nanotubes to form graphene nanoribbons. *Nature* **2009**, *458*, 872-877.
5. Ryu, S.; Maultzsch, J.; Han, M. Y.; Kim, P.; Brus, L. E., Raman Spectroscopy of Lithographically Patterned Graphene Nanoribbons. *ACS Nano* **2011**, *5* (5), 4123-4130.
6. Mohanty, N.; Moore, D.; Xu, Z.; Sreeprasad, T. S.; Nagaraja, A.; Rodriguez, A. A.; Berry, V., Nanotomy-based production of transferable and dispersible graphene nanostructures of controlled shape and size. *Nature Communications* **2012**, *3*, 844.
7. Novoselov, K. S. G., A.K.; Morozov, S.V.; Jiang, J.; Zhang, Y.; Dubonos, S.V.; Grigorieva, I.V.; Firsov, A.A., Electric Field Effect in Atomically Thin Carbon Films. *Science* **2004**, *306*, 666-669.
8. Zhou, W.; Li, W.; Xie, Y.; Wang, L.; Pan, K.; Tian, G.; Li, M.; Wang, G.; Qu, Y.; Fu, H., Fabrication of noncovalently functionalized brick-like [small beta]-cyclodextrins/graphene composite dispersions with favorable stability. *RSC Advances* **2014**, *4* (6), 2813-2819.
9. Ishii, Y. S., H.; Kato, H.; Takatori, M.; Kawasaki, S., Facile bottom-up synthesis of graphene nanofragments and nanoribbons by thermal polymerization of pentacenes. *Nanoscale* **2012**, *4*, 6553-6561.
10. Müllen, K. P., K.; Wu, Z.; Li, R.; Liu, X.; Graf, R.; Feng, X., Exfoliation of Graphite into Graphene in Aqueous Solutions of Inorganic Salts. *Journal of the American Chemical Society* **2014**, *136*, 6083-6091.
11. Park, J. S.; Cho, S. M.; Kim, W.-J.; Park, J.; Yoo, P. J., Fabrication of Graphene Thin Films Based on Layer-by-Layer Self-Assembly of Functionalized Graphene Nanosheets. *ACS Applied Materials & Interfaces* **2011**, *3* (2), 360-368.
12. Britnell, L.; Ribeiro, R. M.; Eckmann, A.; Jalil, R.; Belle, B. D.; Mishchenko, A.; Kim, Y.-J.; Gorbachev, R. V.; Georgiou, T.; Morozov, S. V.; Grigorenko, A. N.; Geim, A. K.; Casiraghi, C.; Neto, A. H. C.; Novoselov, K. S., Strong Light-Matter Interactions in Heterostructures of Atomically Thin Films. *Science* **2013**, *340* (6138), 1311-1314.
13. Leenaerts, O.; Partoens, B.; Peeters, F. M., Adsorption of small molecules on graphene. *Microelectronics Journal* **2009**, *40* (4–5), 860-862.
14. Wang, J.; Shi, Z.; Fan, J.; Ge, Y.; Yin, J.; Hu, G., Self-assembly of graphene into three-dimensional structures promoted by natural phenolic acids. *Journal of Materials Chemistry* **2012**, *22* (42), 22459-22466.
15. Seol, J. H.; Jo, I.; Moore, A. L.; Lindsay, L.; Aitken, Z. H.; Pettes, M. T.; Li, X.; Yao, Z.; Huang, R.; Broido, D.; Mingo, N.; Ruoff, R. S.; Shi, L., Two-Dimensional Phonon Transport in Supported Graphene. *Science* **2010**, *328* (5975), 213-216.

16. Johannsen, J. C.; Ulstrup, S.; Crepaldi, A.; Cilento, F.; Zacchigna, M.; Miwa, J. A.; Cacho, C.; Chapman, R. T.; Springate, E.; Fromm, F.; Raidel, C.; Seyller, T.; King, P. D. C.; Parmigiani, F.; Grioni, M.; Hofmann, P., Tunable Carrier Multiplication and Cooling in Graphene. *Nano Letters* **2014**, *15* (1), 326-331.
17. Meyer, J. C.; Geim, A. K.; Katsnelson, M. I.; Novoselov, K. S.; Booth, T. J.; Roth, S., The structure of suspended graphene sheets. *Nature* **2007**, *446* (7131), 60-63.
18. Bermudez, V. M.; Robinson, J. T., Effects of Molecular Adsorption on the Electronic Structure of Single-Layer Graphene. *Langmuir* **2011**, *27* (17), 11026-11036.
19. Coleman, J. N., Liquid-Phase Exfoliation of Nanotubes and Graphene. *Advanced Functional Materials* **2009**, *19* (23), 3680-3695.
20. Cooper, A. J.; Wilson, N. R.; Kinloch, I. A.; Dryfe, R. A. W., Single stage electrochemical exfoliation method for the production of few-layer graphene via intercalation of tetraalkylammonium cations. *Carbon* **2014**, *66*, 340-350.
21. Kim, K. S. G., V.; Otyepka, M.; Bourlinos, A.B.; Chandra, V.; Kim, N.; Kemp, K.C.; Hobza, P.; Zboril, R., Functionalization of Graphene: Covalent and Non-Covalent Approaches, Derivatives and Applications. *Chemical Reviews* **2012**, *112*, 6156-6214.
22. Haddon, R. C. C., E.H.; deHeer, W.A.; Lau, C.N.; Berger, C.; Sprinkle, M.; Hicks, J.; Shepperd, K.; Zhang, H.; Itkis, M.E.; Bekyarova, E.; Niyogi, S., Spectroscopy of Covalently Functionalized Graphene. *Nano Letters* **2010**, *10*, 4061-4066.
23. Pumera, M. C., C.K., Covalent chemistry on graphene. *Chemical Society Reviews* **2013**, *42*, 3222-3233.
24. Brooksby, P. A.; Farquhar, A. K.; Dykstra, H. M.; Waterland, M. R.; Downard, A. J., Quantum Capacitance of Aryldiazonium Modified Large Area Few-Layer Graphene Electrodes. *The Journal of Physical Chemistry C* **2015**, *119* (46), 25778-25785.
25. Braganca, A. M.; Greenwood, J.; Ivashenko, O.; Phan, T. H.; Mullen, K.; De Feyter, S., The impact of grafted surface defects and their controlled removal on supramolecular self-assembly. *Chemical Science* **2016**, *7* (12), 7028-7033.
26. Sarkar, S.; Bekyarova, E.; Haddon, R. C., Chemistry at the Dirac Point: Diels-Alder Reactivity of Graphene. *Accounts of Chemical Research* **2012**, *45* (4), 673-682.
27. Dai, H. L., Z.; Robinson, J.T.; Sun, X., PEGylated Nanographene Oxide for Delivery of Water-Insoluble Cancer Drugs. *Journal of the American Chemical Society* **2008**, *130*, 10876-10877.
28. Gudarzi, M. M.; Sharif, F., Self assembly of graphene oxide at the liquid-liquid interface: A new route to the fabrication of graphene based composites. *Soft Matter* **2011**, *7* (7), 3432-3440.
29. Jalili, R.; Aboutalebi, S. H.; Esrafilzadeh, D.; Konstantinov, K.; Moulton, S. E.; Razal, J. M.; Wallace, G. G., Organic Solvent-Based Graphene Oxide Liquid Crystals: A Facile Route toward the Next Generation of Self-Assembled Layer-by-Layer Multifunctional 3D Architectures. *ACS Nano* **2013**, *7* (5), 3981-3990.
30. Tour, J. M. K., D.V.; Fursina, A.A.; Corley, D.A.; Dimiev, A.; Siniskii, A., Kinetics of Diazonium Functionalization of Chemically Converted Graphene Nanoribbons. *ACS Nano* **2010**, *4*, 1949-1954.
31. Brus, L. E. N., C.; Steigerwald, Chen, Z.; Ryu, S.; Liu, H., Photochemical Reactivity of Graphene. *Journal of the American Chemical Society* **2009**, *131*, 17099-17101.
32. Chen, Y. L., Y.; Zhou, J.; Zhang, X.; Liu, Z.; Wan, X.; Tian, J.; Wang, T., Synthesis, characterization and optical limiting property of covalently oligothiophene-functionalized graphene material. *Carbon* **2009**, *47*, 3113-3121.

33. Chen, Y. Z., X.; Ma, Y.; Huang, Y.; Tian, J.; Wang, Y.; Zhang, X.; Liu, Z.; Xu, Y., A Graphene Hybrid Material Covalently Functionalized with Porphyrin: Synthesis and Optical Limiting Property. *Advanced Materials* **2009**, *21*, 1275-1279.
34. Dai, L. B., J.; Durstock, M.; Yang, Y.; Yu, D., Soluble P3HT-Grafted Graphene for Efficient Bilayer-Heterojunction Photovoltaic Devices. *ACS Nano* **2010**, *4*, 5633-5640.
35. Niu, L. S., C.; Yang, H.; Han, D.; Zhang, Q.; Ivaska, A., Water-Soluble Graphene Covalently Functionalized by Biocompatible Poly-L-lysine. *Langmuir* **2009**, *25*, 12030-12033.
36. Yan, D. G., C.; Kong, H., Controlled Functionalization of Multiwalled Carbon Nanotubes by in Situ Atom Transfer Radical Polymerization. *Journal of the American Chemical Society* **2004**, *126*, 412-413.
37. Le Ru, E.; Etchegoin, P., *Principles of Surface-Enhanced Raman Spectroscopy: and Related Plasmonic Effects*. Elsevier Science: 2008.
38. Batzill, M., The surface science of graphene: Metal interfaces, CVD synthesis, nanoribbons, chemical modifications, and defects. *Surface Science Reports* **2012**, *67*, 83-115.
39. Tour, J. M. Z., Z.; Sun, Z.; Yao, J.; Beitler, E.; Zhu, Y., Growth of graphene from solid carbon sources. *Nature* **2010**, *468*, 549-552.
40. Tour, J. M. Z., Z.; Sun, Z.; Yao, J.; Kosynkin, D.V., Transforming Carbon Nanotube Devices into Nanoribbon Devices. *Journal of the American Chemical Society* **2009**, *131*, 13460-13463.
41. Xiao, B.; Li, X.; Li, X.; Wang, B.; Langford, C.; Li, R.; Sun, X., Graphene Nanoribbons Derived from the Unzipping of Carbon Nanotubes: Controlled Synthesis and Superior Lithium Storage Performance. *The Journal of Physical Chemistry C* **2014**, *118* (2), 881-890.
42. Cataldo, F.; Compagnini, G.; Patané, G.; Ursini, O.; Angelini, G.; Ribic, P. R.; Margaritondo, G.; Cricenti, A.; Palleschi, G.; Valentini, F., Graphene nanoribbons produced by the oxidative unzipping of single-wall carbon nanotubes. *Carbon* **2010**, *48* (9), 2596-2602.
43. Jiao, L.; Zhang, L.; Wang, X.; Diankov, G.; Dai, H., Narrow graphene nanoribbons from carbon nanotubes. *Nature* **2009**, *458* (7240), 877-880.
44. Ambrosi, A.; Pumera, M., Electrochemically Exfoliated Graphene and Graphene Oxide for Energy Storage and Electrochemistry Applications. *Chemistry – A European Journal* **2016**, *22* (1), 153-159.
45. Shinde, D. B.; Brenker, J.; Easton, C. D.; Tabor, R. F.; Neild, A.; Majumder, M., Shear Assisted Electrochemical Exfoliation of Graphite to Graphene. *Langmuir* **2016**, *32* (14), 3552-3559.
46. Ma, C.; Xiao, Z.; Zhang, H.; Liang, L.; Huang, J.; Lu, W.; Sumpter, B. G.; Hong, K.; Bernholc, J.; Li, A.-P., Controllable conversion of quasi-freestanding polymer chains to graphene nanoribbons. **2017**, *8*, 14815.
47. Kawai, S.; Eren, B.; Marot, L.; Meyer, E., Graphene Synthesis via Thermal Polymerization of Aromatic Quinone Molecules. *ACS Nano* **2014**, *8* (6), 5932-5938.
48. Fischer, H. O., H., *Die Chemie des Pyrrols*. Akademische Verlagsgesellschaft: Leipzig, 1934-40.
49. Leen, V. Y., P.; Wang, L.; Beons, N.; Dehaen, W., Synthesis of Meso-Halogenated BODIPYs and Access to Meso-Substituted Analogues. *Organic Letters* **2012**, *14*, 6150-6153.

50. McLean, T. M.; Cleland, D.; Gordon, K. C.; Telfer, S. G.; Waterland, M. R., Raman spectroscopy of dipyrrens: nonresonant, resonant and surface-enhanced cross-sections and enhancement factors. *Journal of Raman Spectroscopy* **2011**, *42* (12), 2154-2164.
51. McLean, T. M.; Cleland, D. M.; Lind, S. J.; Gordon, K. C.; Telfer, S. G.; Waterland, M. R., Strongly Absorbing π - π^* States in Heteroleptic Dipyrin/2,2'-Bipyridine Ruthenium Complexes: Excited-State Dynamics from Resonance Raman Spectroscopy. *Chemistry – An Asian Journal* **2010**, *5* (9), 2036-2046.
52. Boens, N.; Leen, V.; Dehaen, W., Fluorescent indicators based on BODIPY. *Chemical Society Reviews* **2012**, *41* (3), 1130-1172.
53. Coskun, A.; Akkaya, E. U., Ion Sensing Coupled to Resonance Energy Transfer: A Highly Selective and Sensitive Ratiometric Fluorescent Chemosensor for Ag(I) by a Modular Approach. *Journal of the American Chemical Society* **2005**, *127* (30), 10464-10465.
54. Gomez-Duran, C. F. A.; Hu, R.; Feng, G.; Li, T.; Bu, F.; Arseneault, M.; Liu, B.; Peña-Cabrera, E.; Tang, B. Z., Effect of AIE Substituents on the Fluorescence of Tetraphenylethene-Containing BODIPY Derivatives. *ACS Applied Materials & Interfaces* **2015**, *7* (28), 15168-15176.
55. Flores-Rizo, J. O. E., I; Osorio-Martínez, C.A.; Gómez-Durán, C.F.A.; Bañuelos, J.; López Arbeloa, I.; Pannell, K.H.; Metta-Magaña, A.J.; Peña-Cabrera, E., 8-Alkoxy- and 8-Aryloxy-BODIPYs: Straightforward Fluorescent Tagging of Alcohols and Phenols. *Journal of Organic Chemistry* **2013**, *78*, 5867-5877.
56. Ulrich, G.; Ziesel, R.; Harriman, A., The Chemistry of Fluorescent Bodipy Dyes: Versatility Unsurpassed. *Angewandte Chemie International Edition* **2008**, *47* (7), 1184-1201.
57. Peña-Cabrera, E.; Aguilar-Aguilar, A.; González-Domínguez, M.; Lager, E.; Zamudio-Vázquez, R.; Godoy-Vargas, J.; Villanueva-García, F., Simple, General, and Efficient Synthesis of Meso-Substituted Borondipyrromethenes from a Single Platform. *Organic Letters* **2007**, *9* (20), 3985-3988.
58. Goud, T. V. T., A.; Biellmann, J-F., Synthesis of 8-heteratom-substituted 4,4-difluoro-4-bora-3a,4a-diaza-s-indacene dyes (BODIPY). *Tetrahedron* **2006**, *62*, 5084-5091.
59. Boens, N. W., L.; Leen, V.; Yuan, P.; Verbelen, B.; Dehaen, W.; Van der Auweraer, M.; De Borggraeve, W.D.; Van Meervelt, L.; Jacobs, J.; Beljonne, D.; Tonnele, C.; Lazzaroni, R.; Ruedas-Rama, M.J.; Orte, A.; Crovetto, L.; Talavera, E.M.; Alvarez-Pez, J.M., 8-HaloBODIPYs and Their 8-(C, N, O, S) Substituted Analogues: Solvent Dependent UV-Vis Spectroscopy, Variable Temperature NMR, Crystal Structure Determination, and Quantum Chemical Calculations. *The Journal of Physical Chemistry A* **2014**, *118*, 1576-1594.
60. Balzani, V. C., P.; Juris, A., *Photochemistry and Photophysics: Concepts, Research, Applications*. 1 ed.; Wiley-VCH: Weinheim, Germany, 2014.
61. Ferrari, A. C. B., D.M., Raman spectroscopy as a versatile tool for studying the properties of graphene. *Nature Nanotechnology* **2013**, *8*, 235-246.
62. Pimenta, M. A. D., G.; Dresselhaus, M.S.; Cancado, L.G.; Jorio, A.; Saito, R., Studying disorder in graphite-based systems by Raman spectroscopy. *Physical Chemistry Chemical Physics* **2007**, *9*, 1276-1291.
63. Ferrari, A. C. M., V.; Scardaci, V.; Casiraghi, C.; Lazzeri, M.; Mauri, F.; Piscanec, S.; Jiang, D.; Novoselev, K.S.; Roth, S.; Geim, A.K., Raman Spectrum of Graphene and Graphene Layers. *Physical Review Letters* **2006**, *97*, 187401.

64. Ramasubramaniam, A., Electronic structure of oxygen-terminated zigzag graphene nanoribbons: A hybrid density functional theory study. *Physical Review B* **2010**, *81* (24), 245413.
65. Pimenta, M. A.; del Corro, E.; Carvalho, B. R.; Fantini, C.; Malard, L. M., Comparative Study of Raman Spectroscopy in Graphene and MoS₂-type Transition Metal Dichalcogenides. *Accounts of Chemical Research* **2015**, *48* (1), 41-47.
66. Ni, Z. H.; Yu, T.; Lu, Y. H.; Wang, Y. Y.; Feng, Y. P.; Shen, Z. X., Uniaxial Strain on Graphene: Raman Spectroscopy Study and Band-Gap Opening. *ACS Nano* **2008**, *2* (11), 2301-2305.
67. Tommasini, M.; Castiglioni, C.; Zerbi, G., Raman scattering of molecular graphenes. *Physical Chemistry Chemical Physics* **2009**, *11* (43), 10185-10194.
68. Mapelli, C.; Castiglioni, C.; Meroni, E.; Zerbi, G., Graphite and graphitic compounds: vibrational spectra from oligomers to real materials. *Journal of Molecular Structure* **1999**, *480-481* (0), 615-620.
69. Castiglioni, C.; Mapelli, C.; Negri, F.; Zerbi, G., Origin of the D line in the Raman spectrum of graphite: A study based on Raman frequencies and intensities of polycyclic aromatic hydrocarbon molecules. *The Journal of Chemical Physics* **2001**, *114* (2), 963-974.
70. Negri, F.; di Donato, E.; Tommasini, M.; Castiglioni, C.; Zerbi, G.; Müllen, K., Resonance Raman contribution to the D band of carbon materials: Modeling defects with quantum chemistry. *The Journal of Chemical Physics* **2004**, *120* (24), 11889-11900.
71. Dresselhaus, M. S.; Dresselhaus, G.; Jorio, A.; Souza Filho, A. G.; Saito, R., Raman spectroscopy on isolated single wall carbon nanotubes. *Carbon* **2002**, *40* (12), 2043-2061.
72. Thomsen, C. R., S., Double Resonant Raman Scattering in Graphite. *Physical Review Letters* **2000**, *85* (24), 5214-5217.
73. Farquhar, A. K.; Fitchett, C. M.; Dykstra, H. M.; Waterland, M. R.; Brooksby, P. A.; Downard, A. J., Diels-Alder Reaction of Anthranilic Acids: A Versatile Route to Dense Monolayers on Flat Edge and Basal Plane Graphitic Carbon Substrates. *ACS Applied Materials & Interfaces* **2016**, *8* (35), 23389-23395.
74. Lapointe, F.; Rousseau, B.; Aymong, V.; Nguyen, M.; Biron, M.; Gaufres, E.; Choubak, S.; Han, Z.; Bouchiat, V.; Desjardins, P.; Côté, M.; Martel, R., Antiresonances in the Mid-Infrared Vibrational Spectrum of Functionalized Graphene. *The Journal of Physical Chemistry C* **2017**, *121* (16), 9053-9062.
75. Boukhvalov, D. W., DFT modeling of the covalent functionalization of graphene: from ideal to realistic models. *RSC Advances* **2013**, *3* (20), 7150-7159.
76. Wood, B. C.; Bhide, S. Y.; Dutta, D.; Kandagal, V. S.; Pathak, A. D.; Punnathanam, S. N.; Ayappa, K. G.; Narasimhan, S., Methane and carbon dioxide adsorption on edge-functionalized graphene: A comparative DFT study. *Journal of Chemical Physics* **2012**, *137* (5), 054702.
77. Negri, F.; Castiglioni, C.; Tommasini, M.; Zerbi, G., A Computational Study of the Raman Spectra of Large Polycyclic Aromatic Hydrocarbons: Toward Molecularly Defined Subunits of Graphite†. *The Journal of Physical Chemistry A* **2002**, *106* (14), 3306-3317.
78. Chae, D.-H.; Utikal, T.; Weisenburger, S.; Giessen, H.; Klitzing, K. v.; Lippitz, M.; Smet, J., Excitonic Fano Resonance in Free-Standing Graphene. *Nano Letters* **2011**, *11* (3), 1379-1382.

79. Mak, K. F.; Shan, J.; Heinz, T. F., Seeing Many-Body Effects in Single- and Few-Layer Graphene: Observation of Two-Dimensional Saddle-Point Excitons. *Physical Review Letters* **2011**, *106* (4), 046401.
80. Yoon, D.; Jeong, D.; Lee, H.-J.; Saito, R.; Son, Y.-W.; Lee, H. C.; Cheong, H., Fano resonance in Raman scattering of graphene. *Carbon* **2013**, *61* (0), 373-378.
81. Solà, M., Forty years of Clar's aromatic π -sextet rule. *Frontiers in Chemistry* **2013**, *1*, 22.
82. Clar, E., *The Aromatic Sextet*. John Wiley and Sons Ltd.: London, 1972.
83. Nielsen, T., Reactivity of polycyclic aromatic hydrocarbons towards nitrating species. *Environmental Science & Technology* **1984**, *18* (3), 157-163.
84. Güell, M. L., J.M.; Sola, M.; Swart, M., Importance of the Basis Set for the Spin-State Energetics of Iron Complexes. *The Journal of Physical Chemistry A* **2008**, *112* (28), 6384-6391.
85. Szabo, A. O., N.S., Many-Electron Wave Functions and Operators. In *Modern Quantum Chemistry: Introduction to Advanced Electronic Structure Theory*, Dover Publications, Inc.: Mineola, New York, 1996; p 56.
86. Hehre, H. J. S., R.F.; Pople, J.A., Self-Consistent Molecular-Orbital Methods. I. Use of Gaussian Expansions of Slater-Type Atomic Orbitals. *The Journal of Chemical Physics* **1969**, *51*, 2657-2664.
87. NV, S. C. M., Frequencies. In *SCM: ADF Manual*, Amsterdam, The Netherlands, 2014; p 174.
88. Li, J.; Croiset, E.; Ricardez-Sandoval, L., Methane dissociation on Ni (1 0 0), Ni (1 1 1), and Ni (5 5 3): A comparative density functional theory study. *Journal of Molecular Catalysis A: Chemical* **2012**, *365*, 103-114.
89. Gilli, P.; Pretto, L.; Bertolasi, V.; Gilli, G., Predicting Hydrogen-Bond Strengths from Acid-Base Molecular Properties. The pKa Slide Rule: Toward the Solution of a Long-Lasting Problem. *Accounts of Chemical Research* **2009**, *42* (1), 33-44.
90. Ho, J.; Coote, M. L., A universal approach for continuum solvent pK a calculations: are we there yet? *Theoretical Chemistry Accounts* **2009**, *125* (1), 3.
91. Eckert, F.; Diedenhofen, M.; Klamt, A., Towards a first principles prediction of pK a: COSMO-RS and the cluster-continuum approach. *Molecular Physics* **2010**, *108* (3-4), 229-241.
92. Ru, E. L.; Etchegoin, P., *Principles of Surface-Enhanced Raman Spectroscopy: and Related Plasmonic Effects*. Elsevier Science: 2008.
93. Kasha, M.; Rawls, H. R.; Ashraf El-Bayoumi, M., The exciton model in molecular spectroscopy. In *Pure and Applied Chemistry*, 1965; Vol. 11, p 371.
94. Telfer, S. G.; McLean, T. M.; Waterland, M. R., Exciton coupling in coordination compounds. *Dalton Transactions* **2011**, *40* (13), 3097-3108.
95. McLean, T. M.; Moody, J. L.; Waterland, M. R.; Telfer, S. G., Luminescent Rhenium(I)-Dipyrrinato Complexes. *Inorganic Chemistry* **2011**, *51* (1), 446-455.
96. Nizamov, S.; Willig, K. I.; Sednev, M. V.; Belov, V. N.; Hell, S. W., Phosphorylated 3-Heteroarylcoumarins and Their Use in Fluorescence Microscopy and Nanoscopy. *Chemistry – A European Journal* **2012**, *18* (51), 16339-16348.
97. Caspar, J. V.; Meyer, T. J., Application of the energy gap law to nonradiative, excited-state decay. *The Journal of Physical Chemistry* **1983**, *87* (6), 952-957.
98. Smith, B. C., The Benzene Fingers, Part I: Overtone and Combination Bands. *Spectroscopy* **2016**, *31* (7), 30-34.
99. Smith, B. C., The Benzene Fingers, Part II: Let Your Fingers Do the Walking Through the Benzene Fingers. *Spectroscopy* **2016**, *31* (9), 30-33.

100. Whittaker, E. T., On a New Method of Graduation. *Proceedings of the Edinburgh Mathematical Society* **1922**, *41*, 63-75.
101. H C Eilers, P.; F M Boelens, H., *Baseline Correction with Asymmetric Least Squares Smoothing*. 2005.
102. Vargas Jentzsch, P.; Ciobotă, V.; Salinas, W.; Kampe, B.; Aponte, P. M.; Rösch, P.; Popp, J.; Ramos, L. A., Distinction of Ecuadorian varieties of fermented cocoa beans using Raman spectroscopy. *Food Chemistry* **2016**, *211*, 274-280.
103. Kim, H. M.; Park, H. S.; Cho, Y.; Jin, S. M.; Lee, K. T.; Jung, Y. M.; Suh, Y. D., Noninvasive deep Raman detection with 2D correlation analysis. *Journal of Molecular Structure* **2014**, *1069*, 223-228.
104. Mabbott, S.; Correa, E.; Cowcher, D. P.; Allwood, J. W.; Goodacre, R., Optimization of Parameters for the Quantitative Surface-Enhanced Raman Scattering Detection of Mephedrone Using a Fractional Factorial Design and a Portable Raman Spectrometer. *Analytical Chemistry* **2013**, *85* (2), 923-931.
105. Vardaki, M. Z.; Matousek, P.; Stone, N., Characterisation of signal enhancements achieved when utilizing a photon diode in deep Raman spectroscopy of tissue. *Biomedical Optics Express* **2016**, *7* (6), 2130-2141.

Appendices

Appendix A: NMR Spectra

NMR solvent peaks are indicated with a X. Solvent impurities are indicated with “s”, whilst other impurities are indicated with “*”.

Thioketone dipyrin

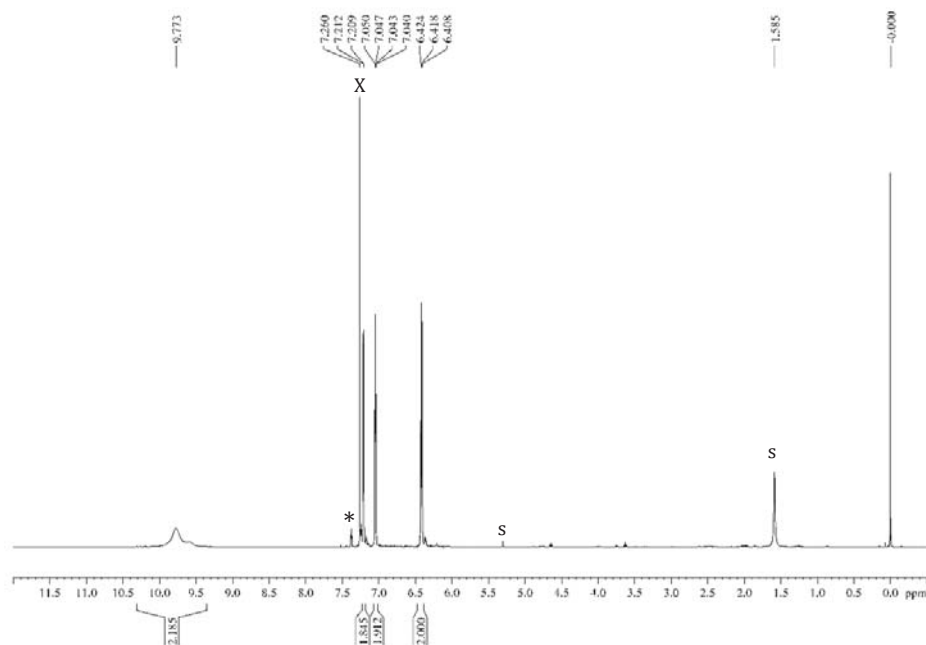


Figure A.1 - ^1H NMR spectrum of thioketone dipyrin in CDCl_3

Ketone dipyrrin

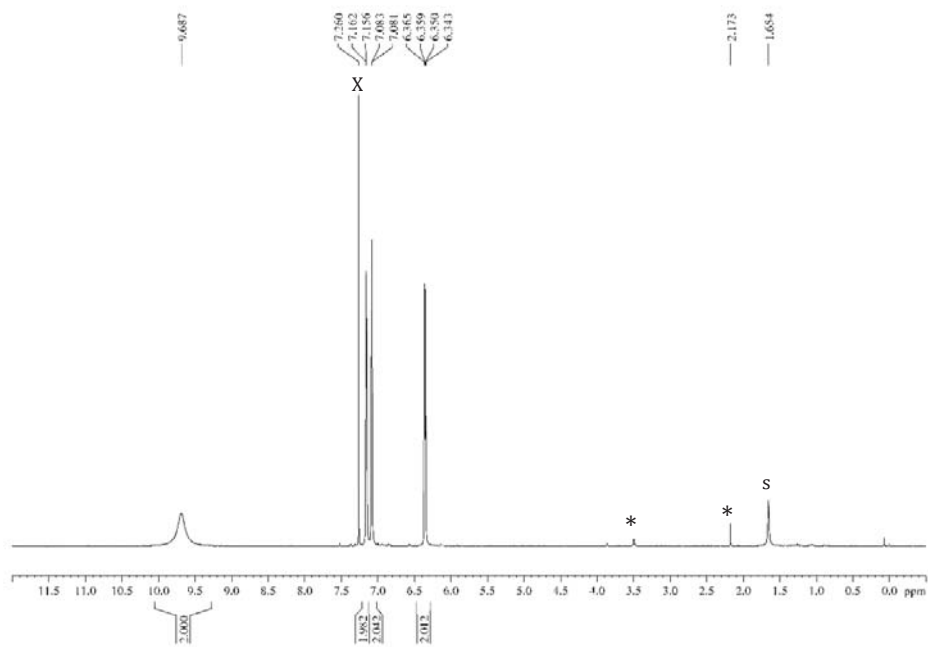


Figure A.2 - ^1H NMR spectrum of ketone dipyrrin in CDCl_3

Phenol/BODIPY

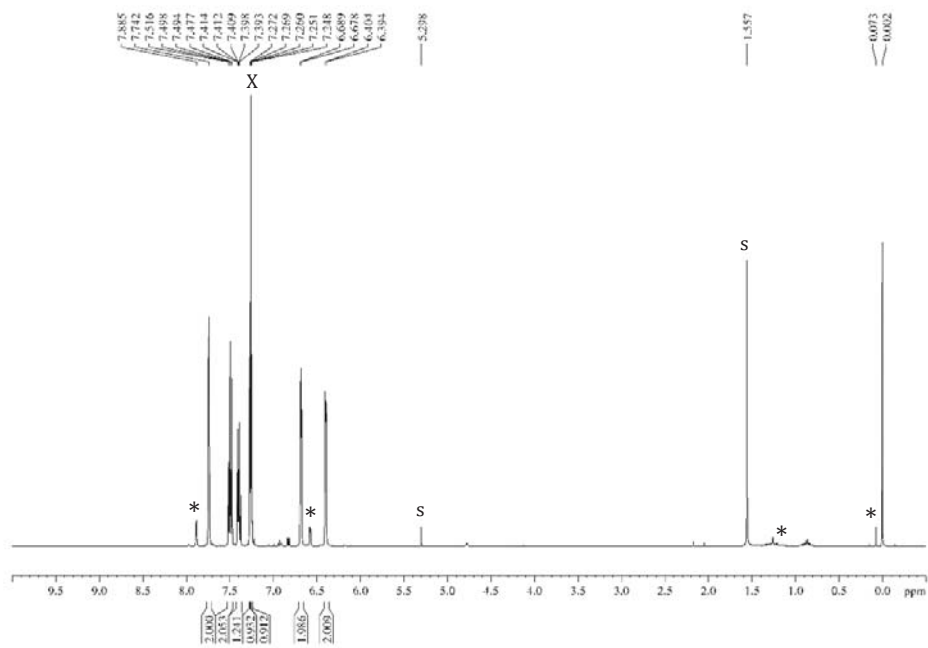


Figure A.3 - ^1H NMR spectrum of phenol/BODIPY in CDCl_3

Cl-BODIPY

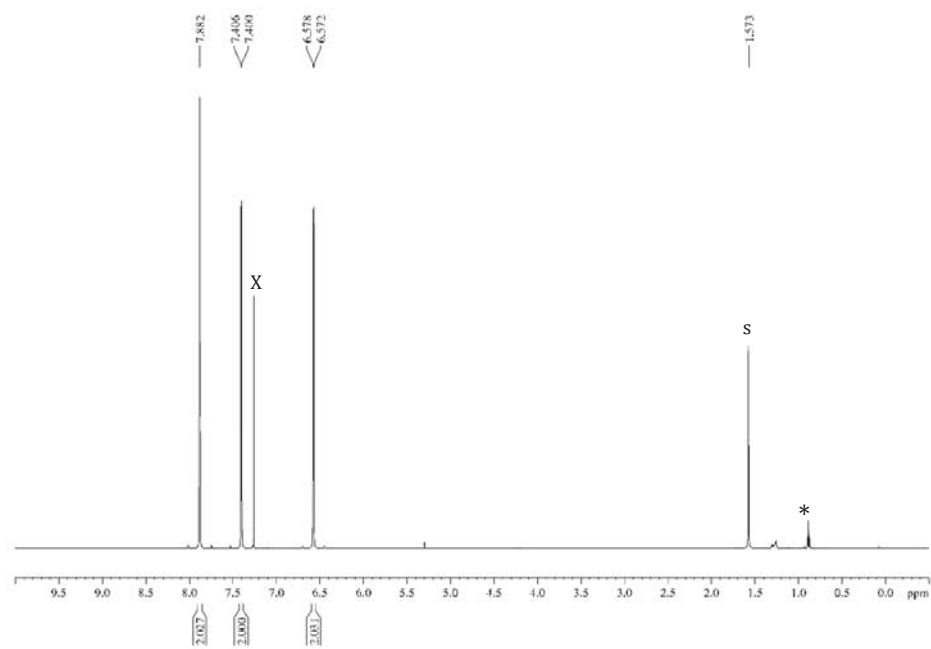


Figure A.4 - ¹H NMR spectrum of Cl-BODIPY in CDCl₃

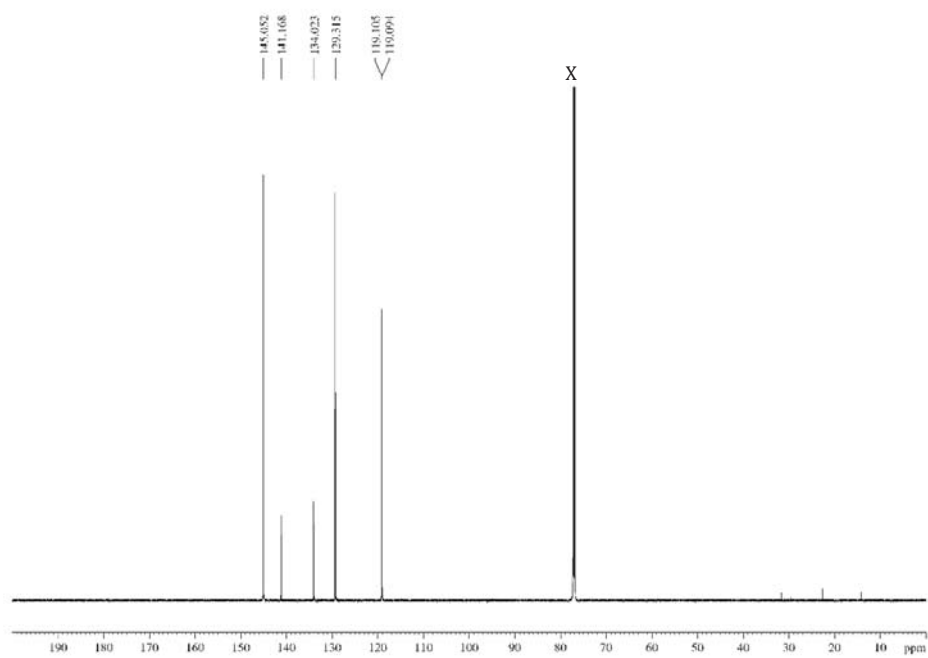


Figure A.5 - ¹³C NMR spectrum of Cl-BODIPY in CDCl₃

MeO/BODIPY

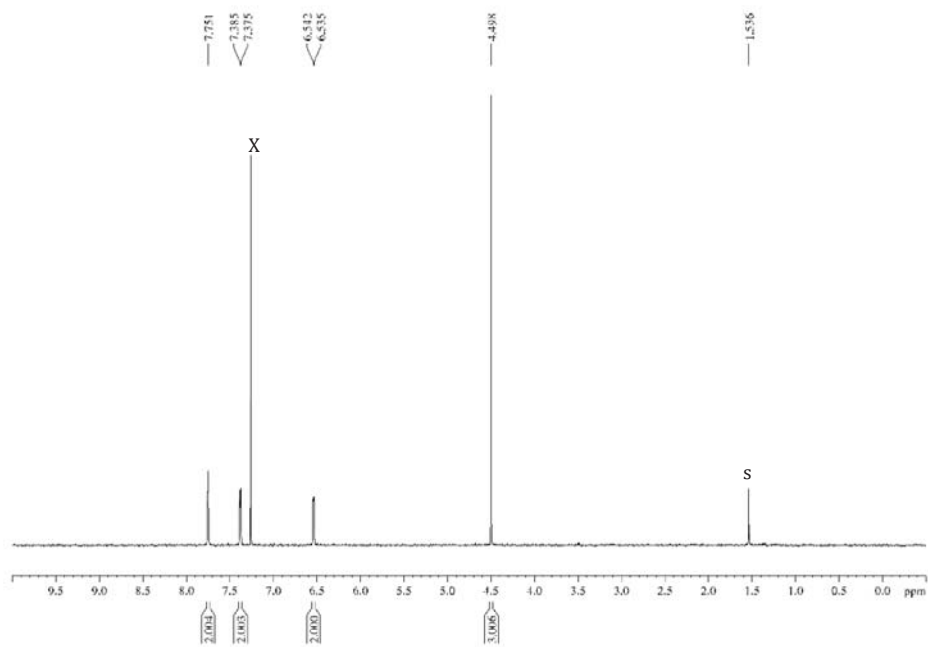


Figure A.6 - ^1H NMR spectrum of MeO/BODIPY in CDCl_3

Aniline/BODIPY

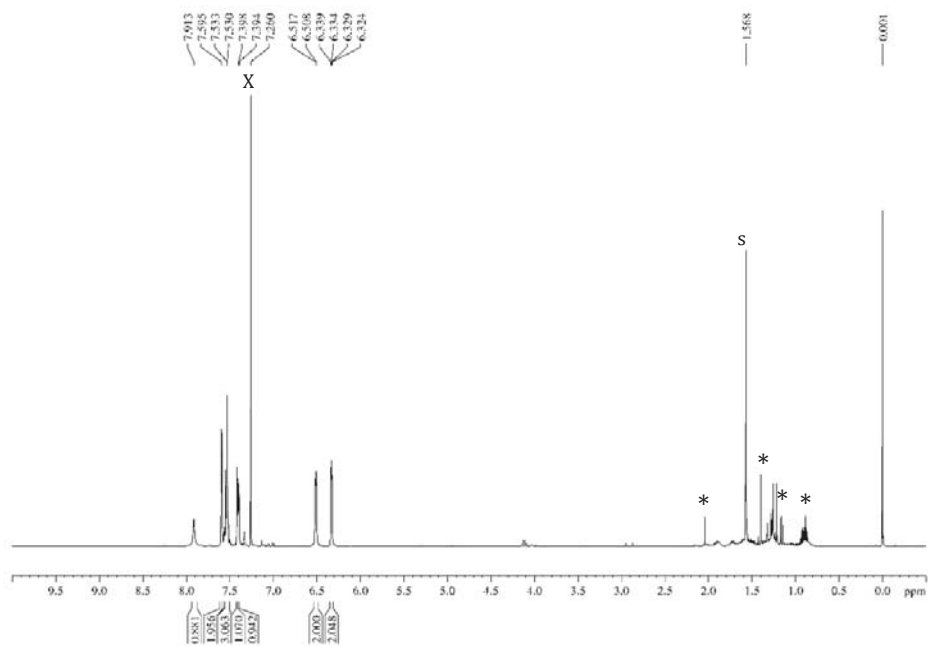


Figure A.7 - ^1H NMR spectrum of aniline/BODIPY in CDCl_3 prepared via literature procedure

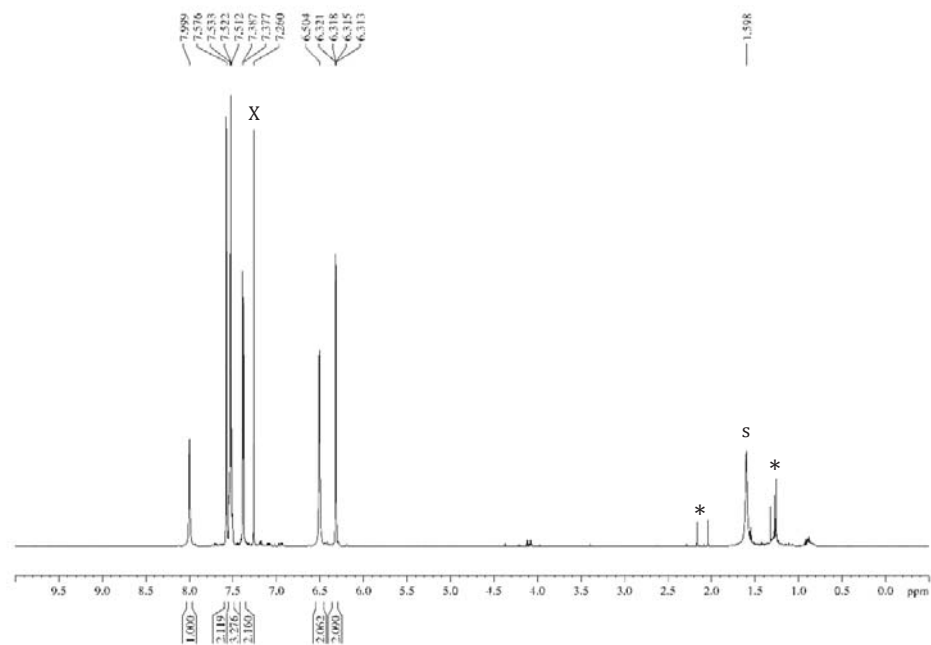


Figure A.8 - ^1H NMR spectrum of aniline/BODIPY in CDCl_3 prepared via modified procedure

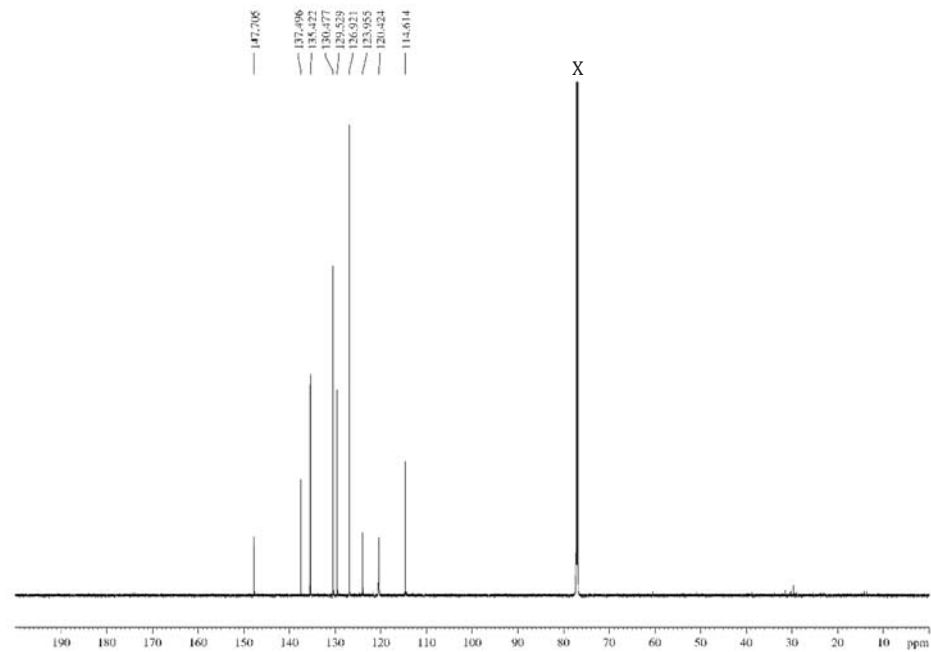


Figure A.9 - ^{13}C NMR spectrum of aniline/BODIPY in CDCl_3 prepared via modified procedure

1-naphthylamine/BODIPY

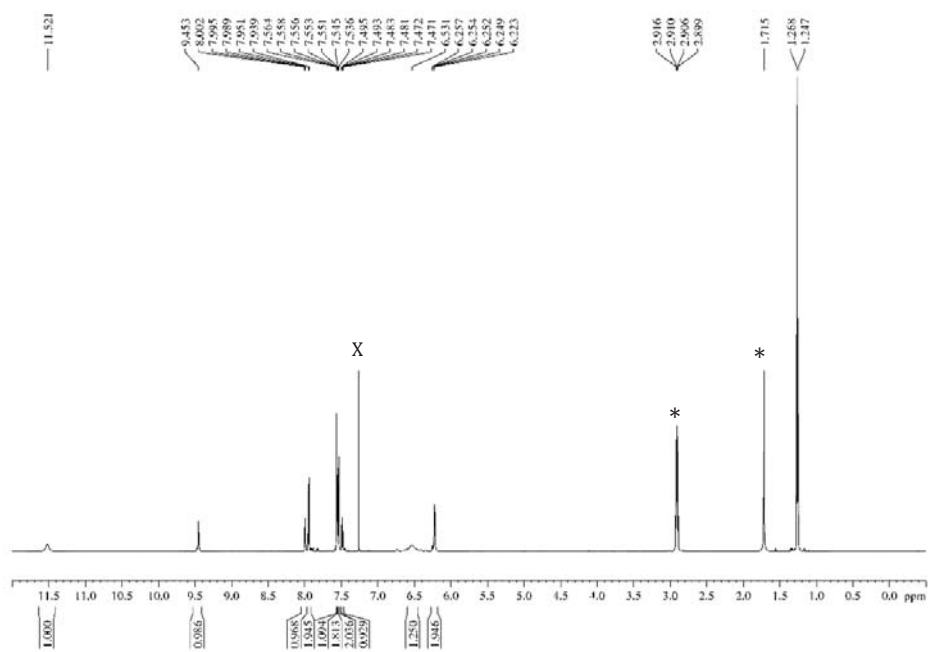


Figure A.10 - ^1H NMR spectrum of 1-naphthylamine/BODIPY in CDCl_3

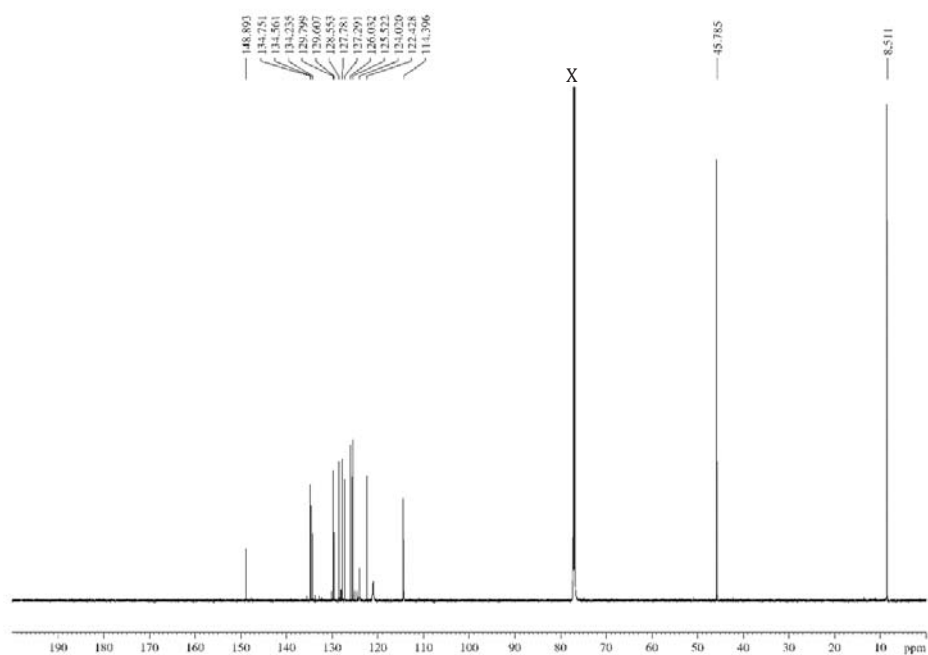


Figure A.11 - ^{13}C NMR spectrum of 1-naphthylamine/BODIPY in CDCl_3

1-naphthol/2xBODIPY

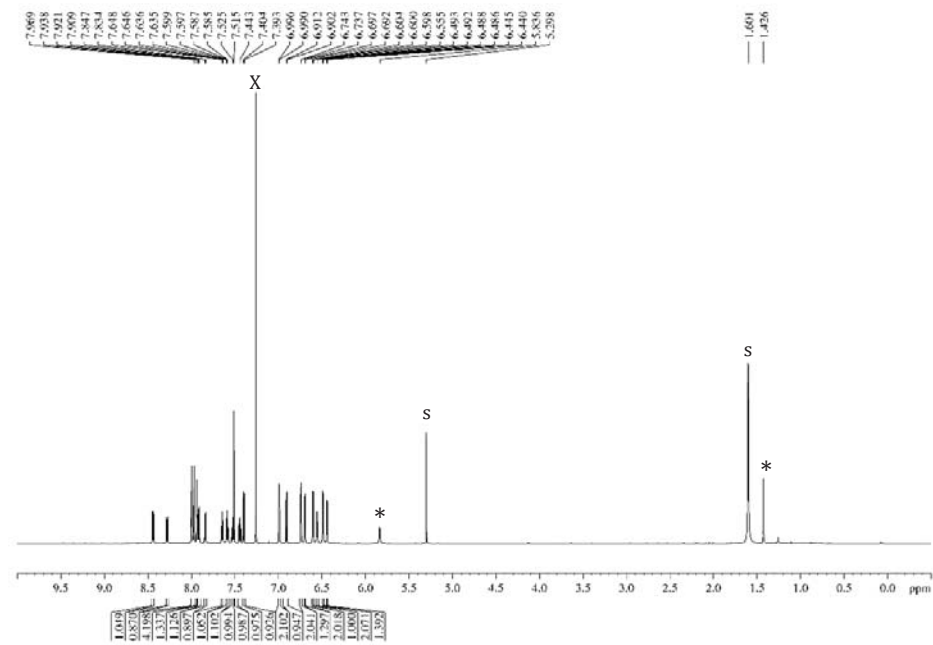


Figure A.14 - ^1H NMR spectrum of 1-naphthol/2xBODIPY in CDCl_3

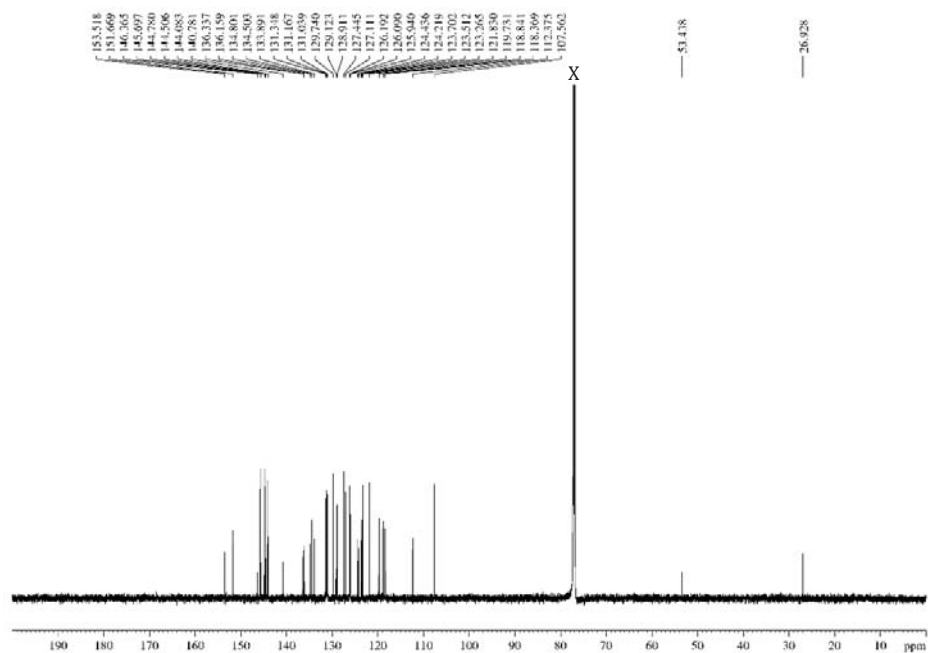


Figure A.15 - ^{13}C NMR spectrum of 1-naphthol/2xBODIPY in CDCl_3

2-naphthol/BODIPY

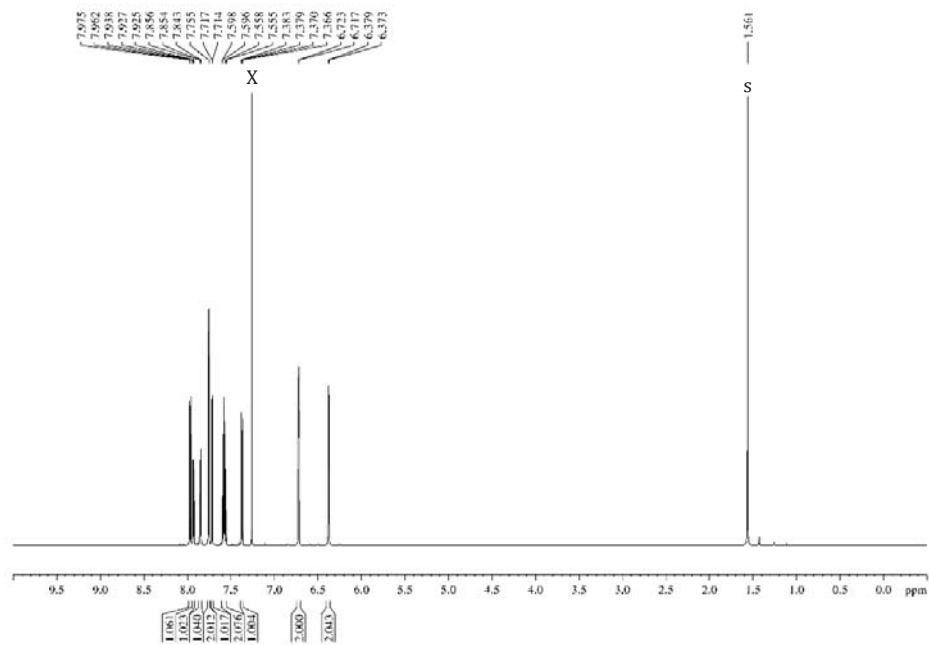


Figure A.16 - ¹H NMR spectrum of 2-naphthol/BODIPY in CDCl₃

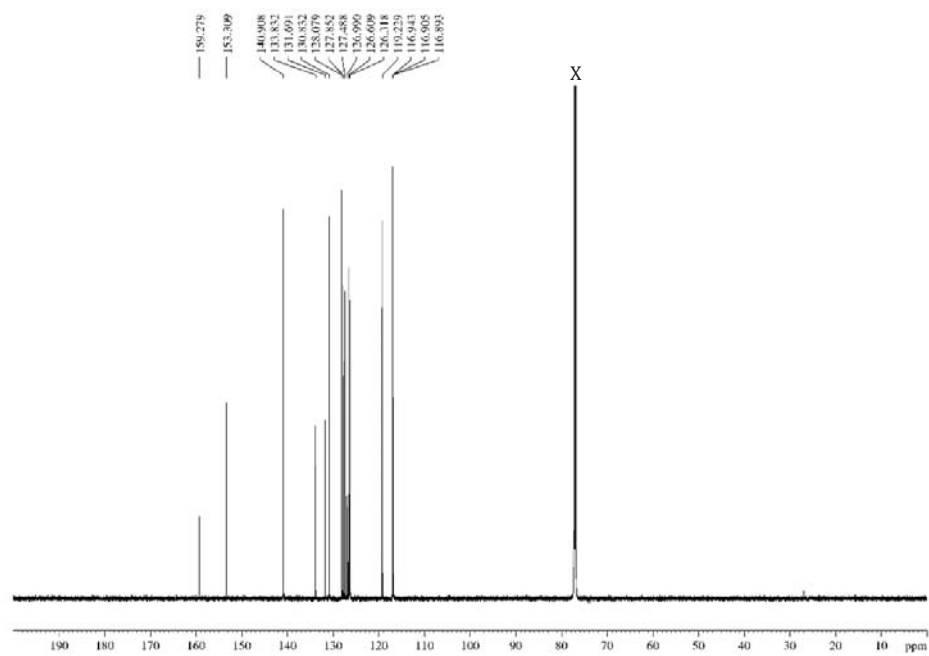


Figure A.17 - ¹³C NMR spectrum of 2-naphthol/BODIPY in CDCl₃

2-naphthol/2xBODIPY

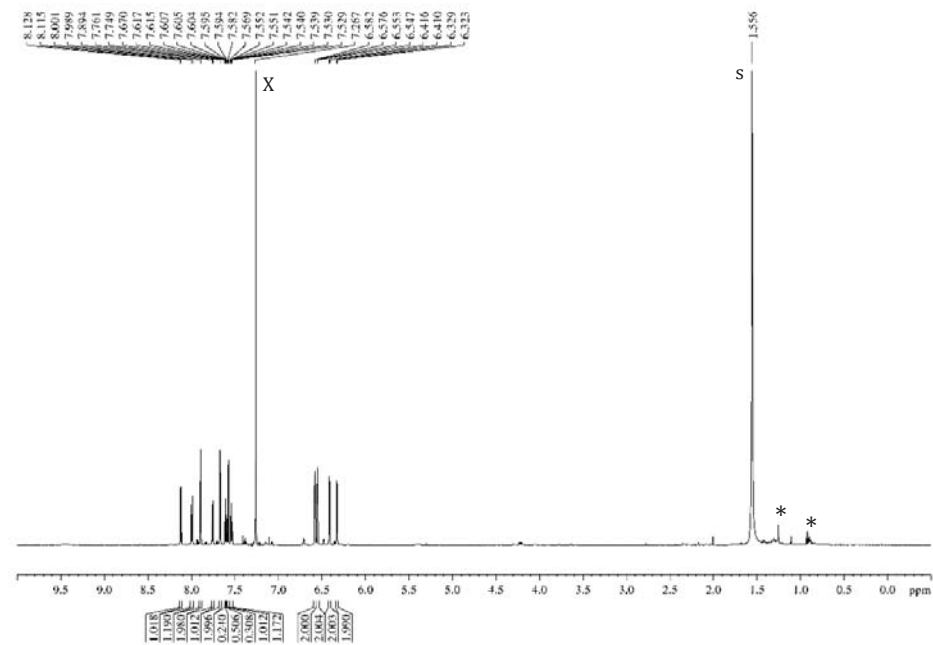


Figure A.18 - ^1H NMR spectrum of 2-naphthol/2xBODIPY in CDCl_3

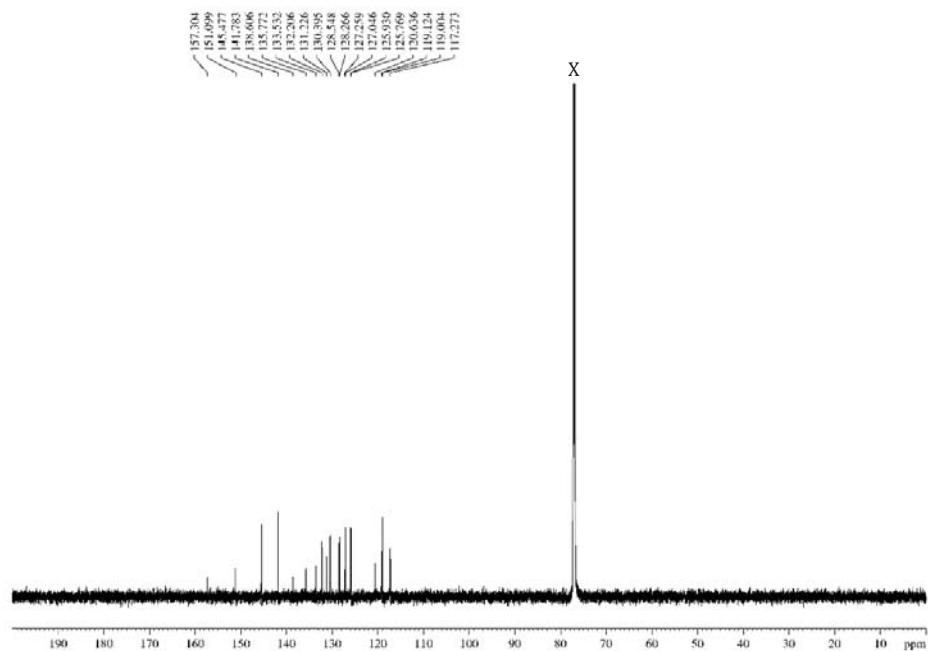


Figure A.19 - ^{13}C NMR spectrum of 2-naphthol/2xBODIPY in CDCl_3

2-aminoanthracene/BODIPY

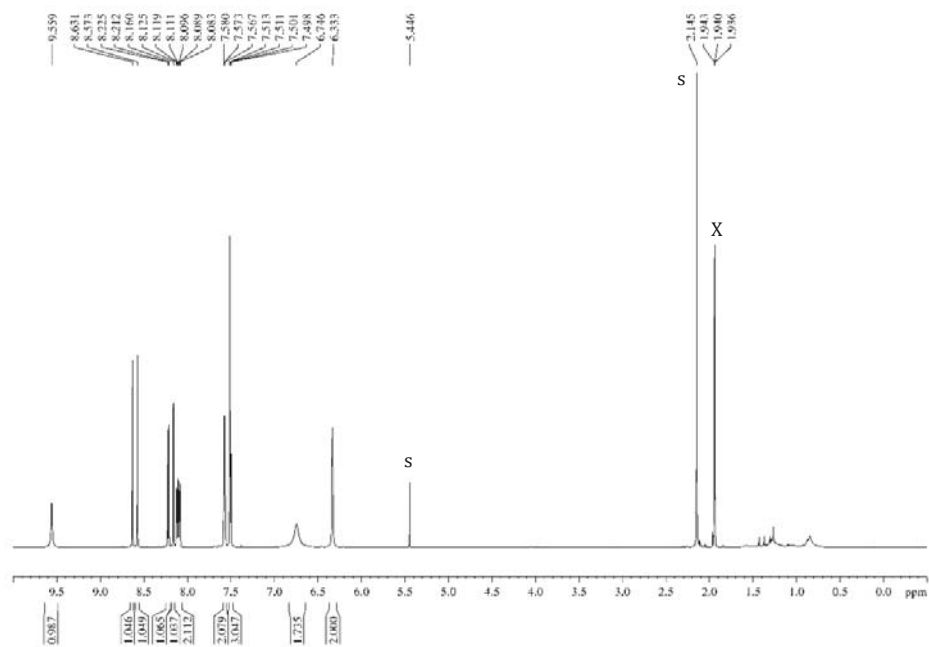


Figure A.20 - ¹H NMR spectrum of 2-aminoanthracene/BODIPY in CD₃CN

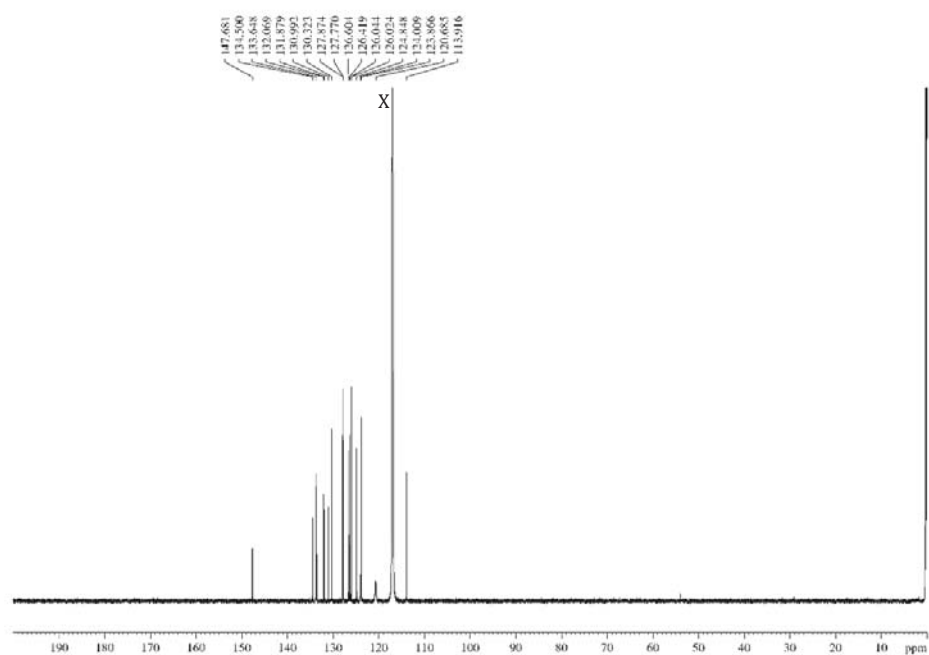


Figure A.21 - ¹³C NMR spectrum of 2-aminoanthracene/BODIPY in CD₃CN

9-hydroxyphenanthrene/BODIPY

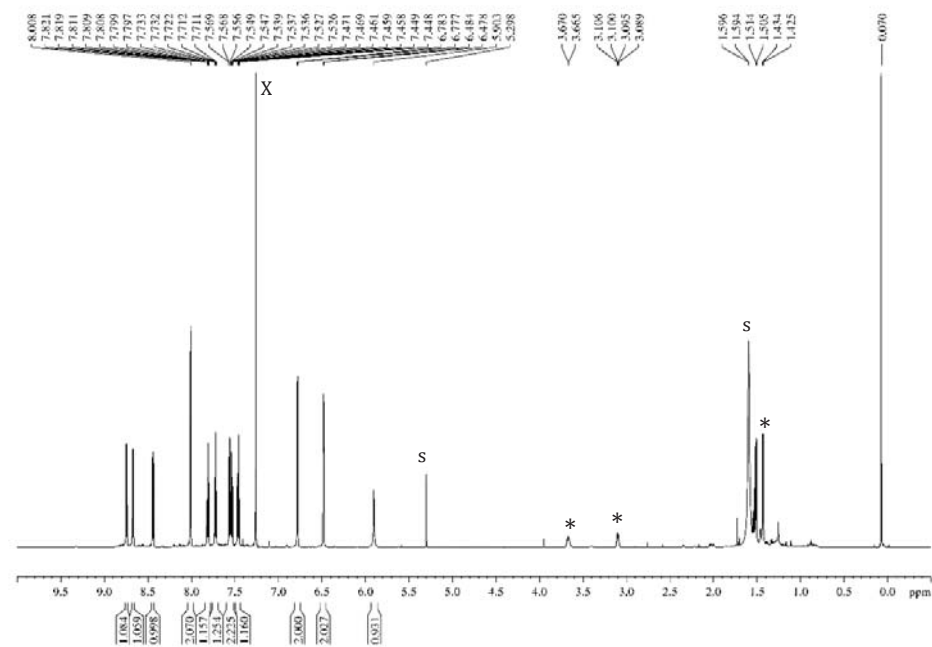


Figure A.22 - ^1H NMR spectrum of 9-hydroxyphenanthrene/BODIPY in CDCl_3

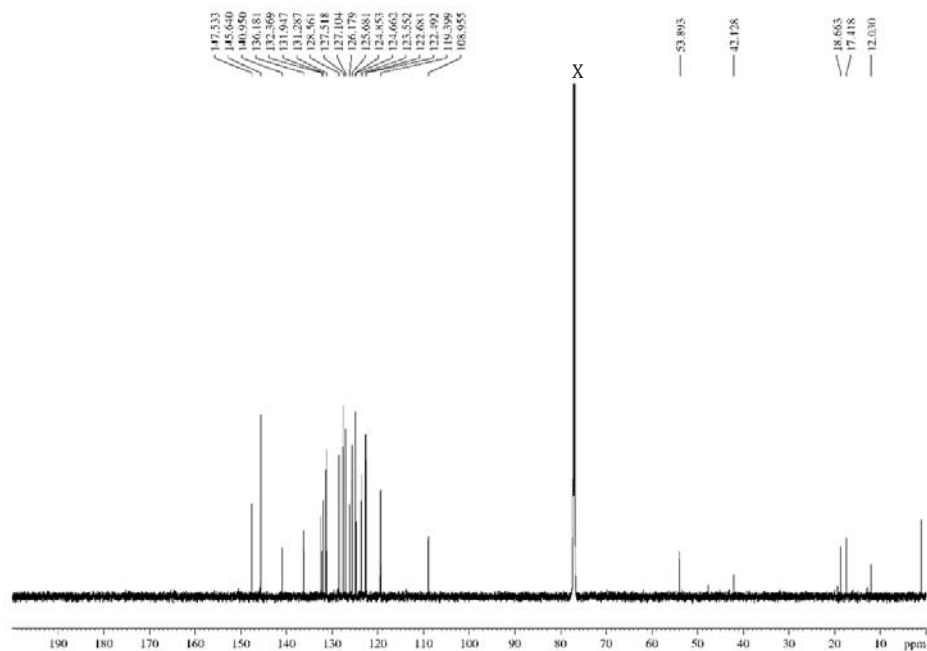


Figure A.23 - ^{13}C NMR spectrum of 9-hydroxyphenanthrene/BODIPY in CDCl_3

2-hydroxytriphenylene/BODIPY

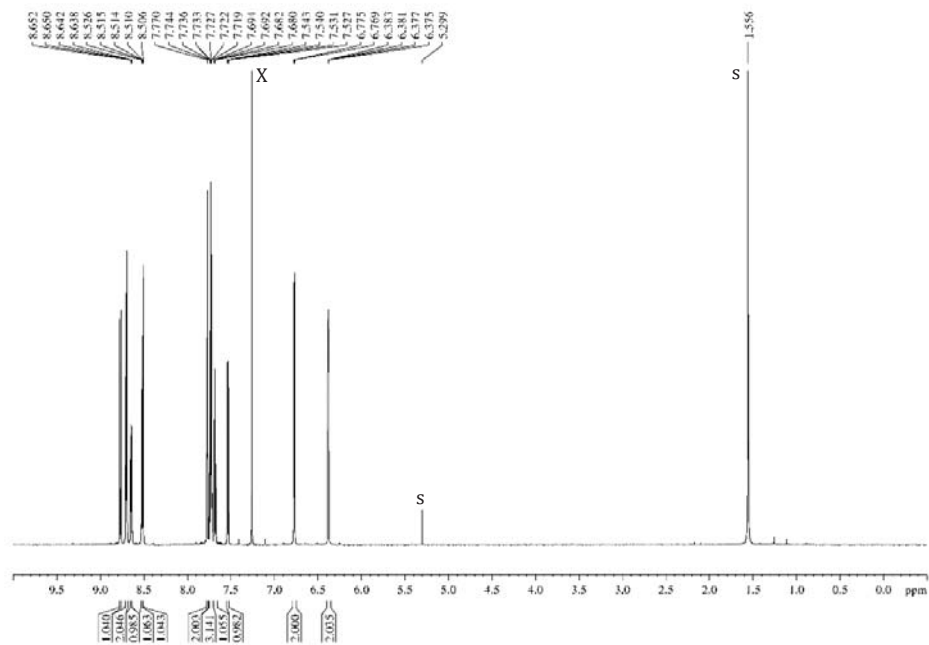


Figure A.24 - ¹H NMR spectrum of 2-hydroxytriphenylene/BODIPY in CDCl₃

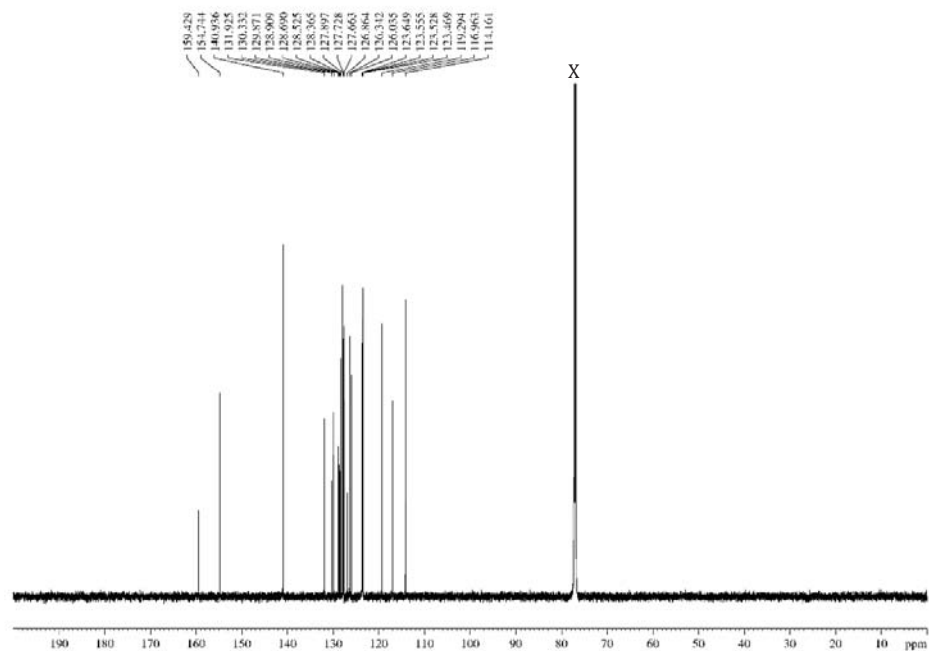


Figure A.25 - ¹³C NMR spectrum of 2-hydroxytriphenylene/BODIPY in CDCl₃

1-hydroxypyrene/BODIPY

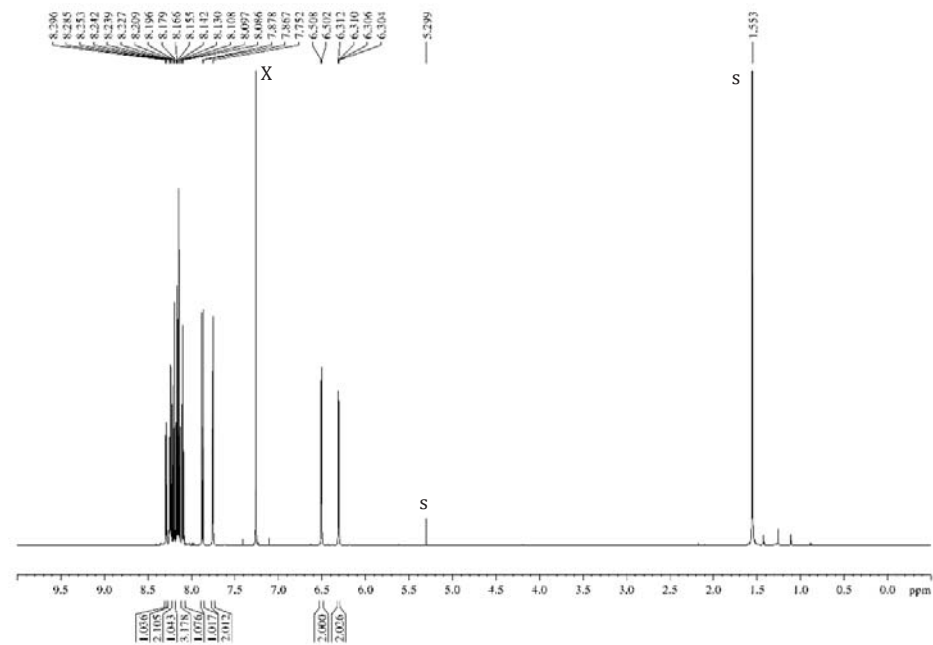


Figure A.26 - ¹H NMR spectrum of 1-hydroxypyrene/BODIPY in CDCl₃

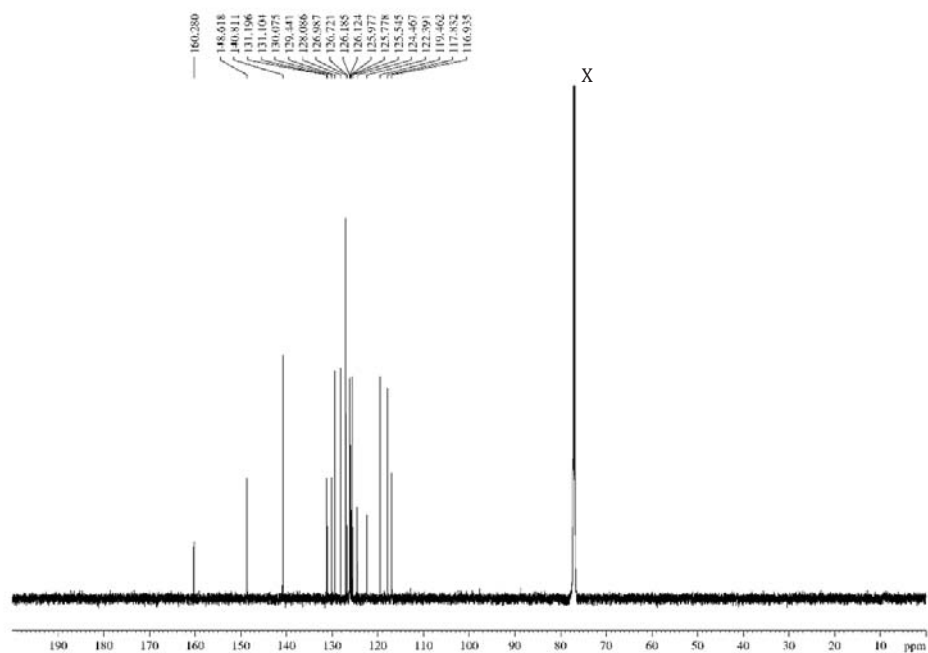


Figure A.27 - ¹³C NMR spectrum of 1-hydroxypyrene/BODIPY in CDCl₃

HBC(*t*-Bu)₅OH/BODIPY

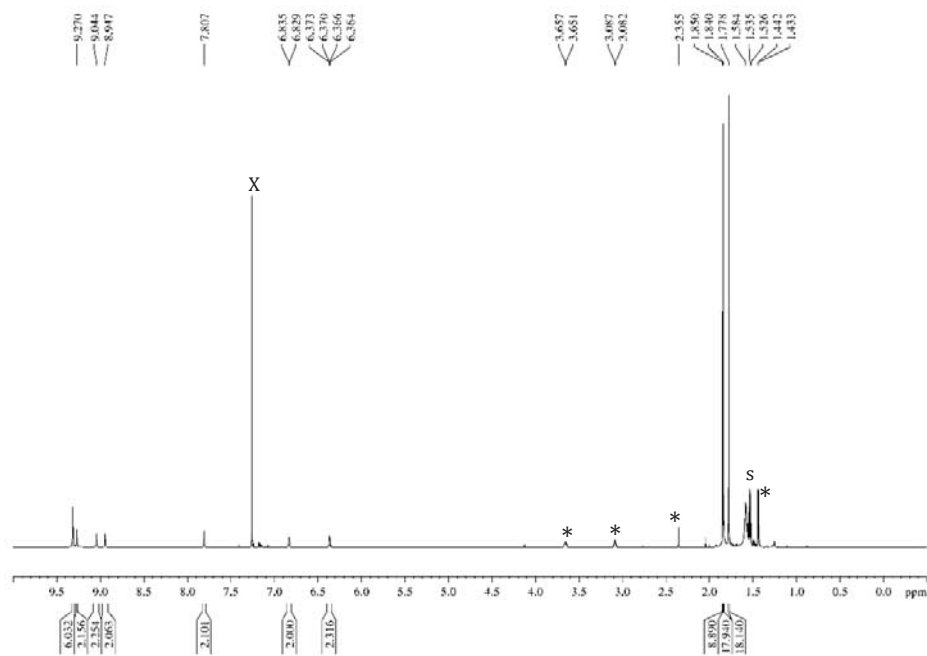


Figure A.28 - ¹H NMR spectrum of HBC(*t*-Bu)₅OH/BODIPY in CDCl₃

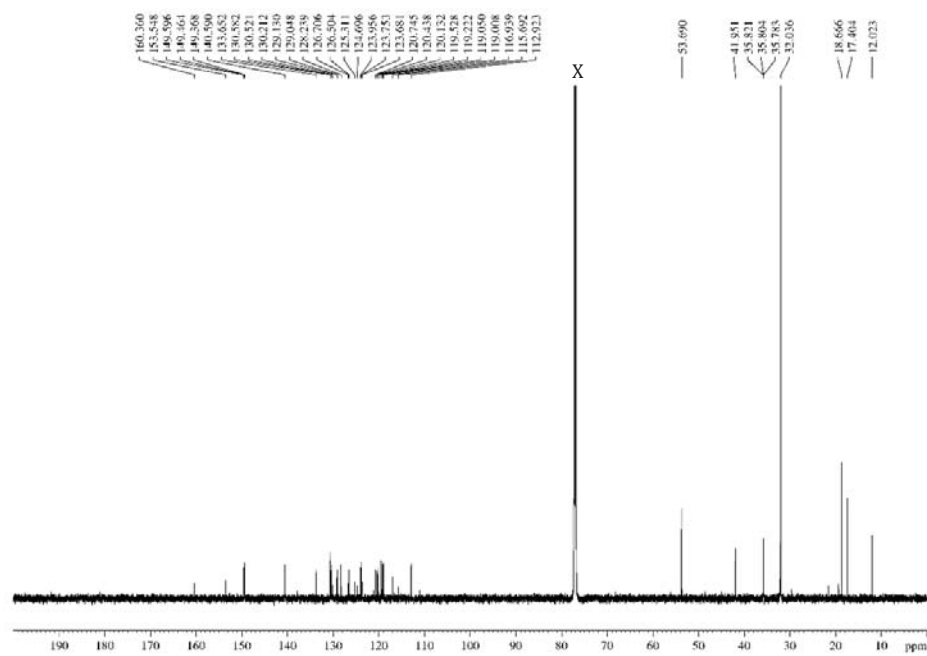


Figure A.29 - ¹³C NMR spectrum of HBC(*t*-Bu)₅OH/BODIPY in CDCl₃

HPB(*t*-Bu)₅OH/BODIPY

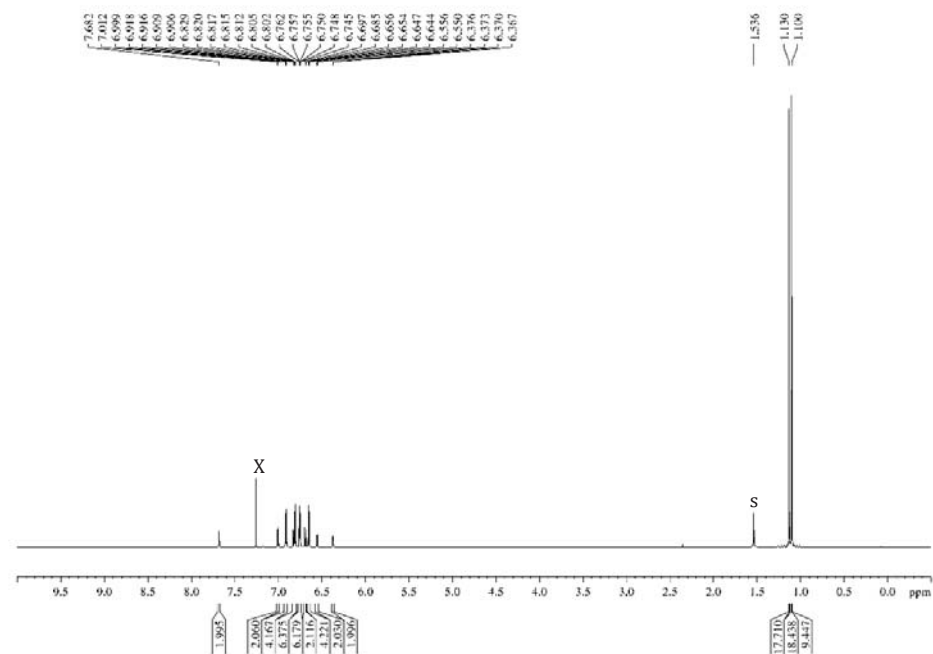


Figure A.30 - ¹H NMR spectrum of HPB(*t*-Bu)₅OH/BODIPY in CDCl₃

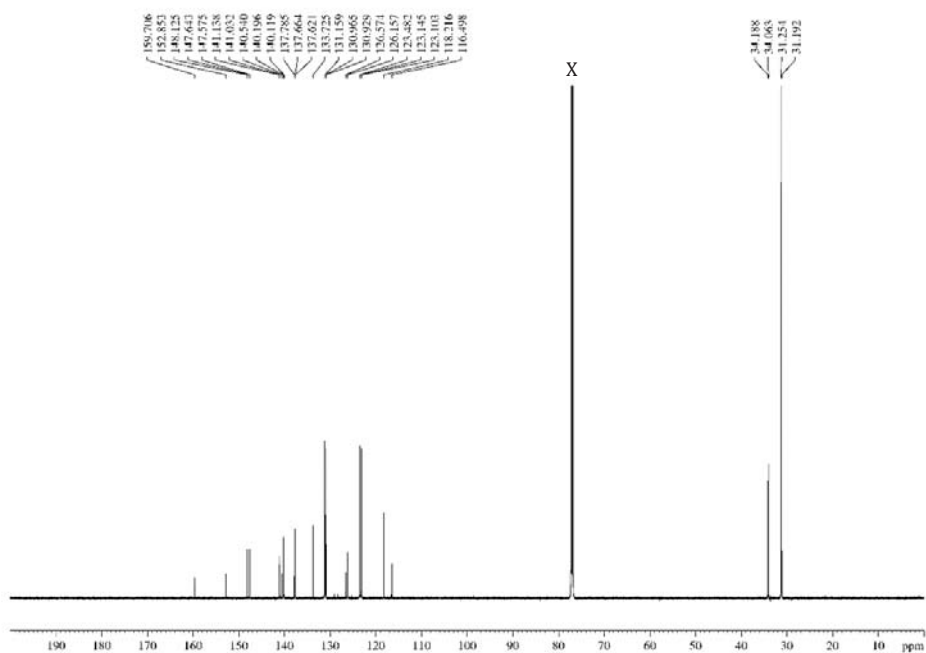


Figure A.31 - ¹³C NMR spectrum of HPB(*t*-Bu)₅OH/BODIPY in CDCl₃

Benzoic acid/BODIPY

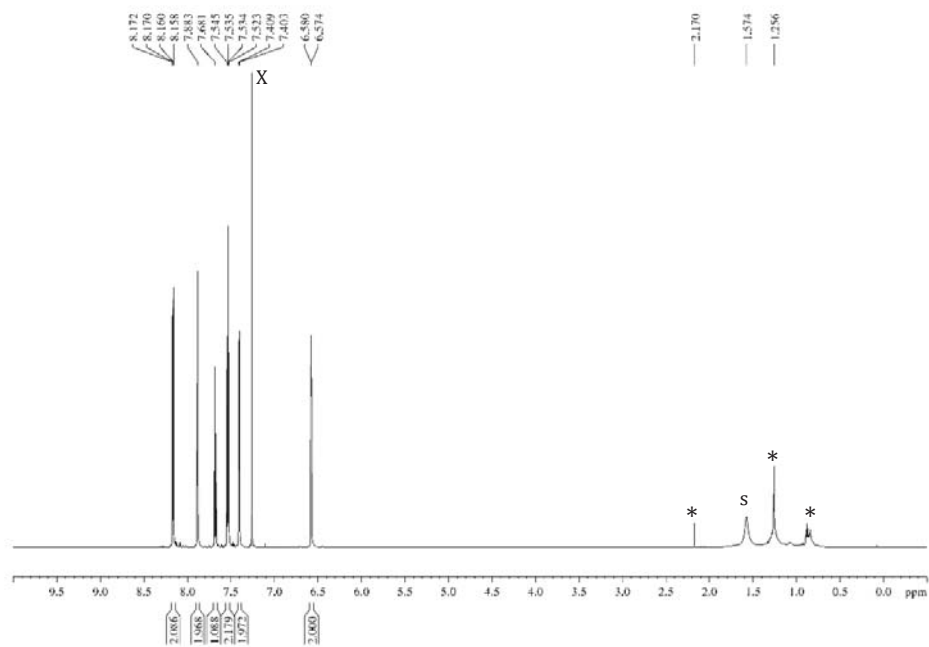


Figure A.32 - ¹H NMR spectrum of benzoic acid/BODIPY in CDCl₃

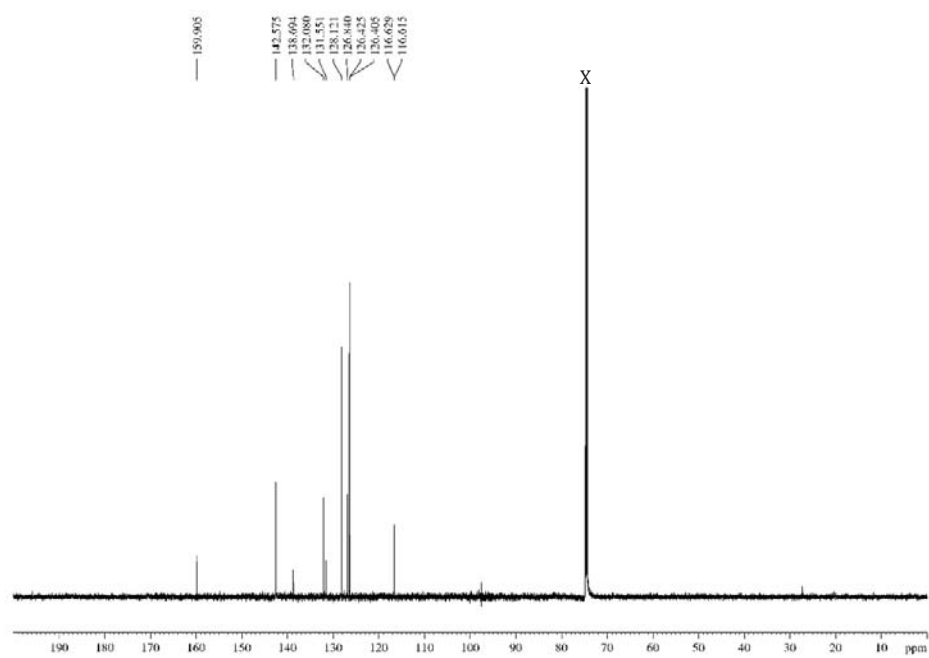


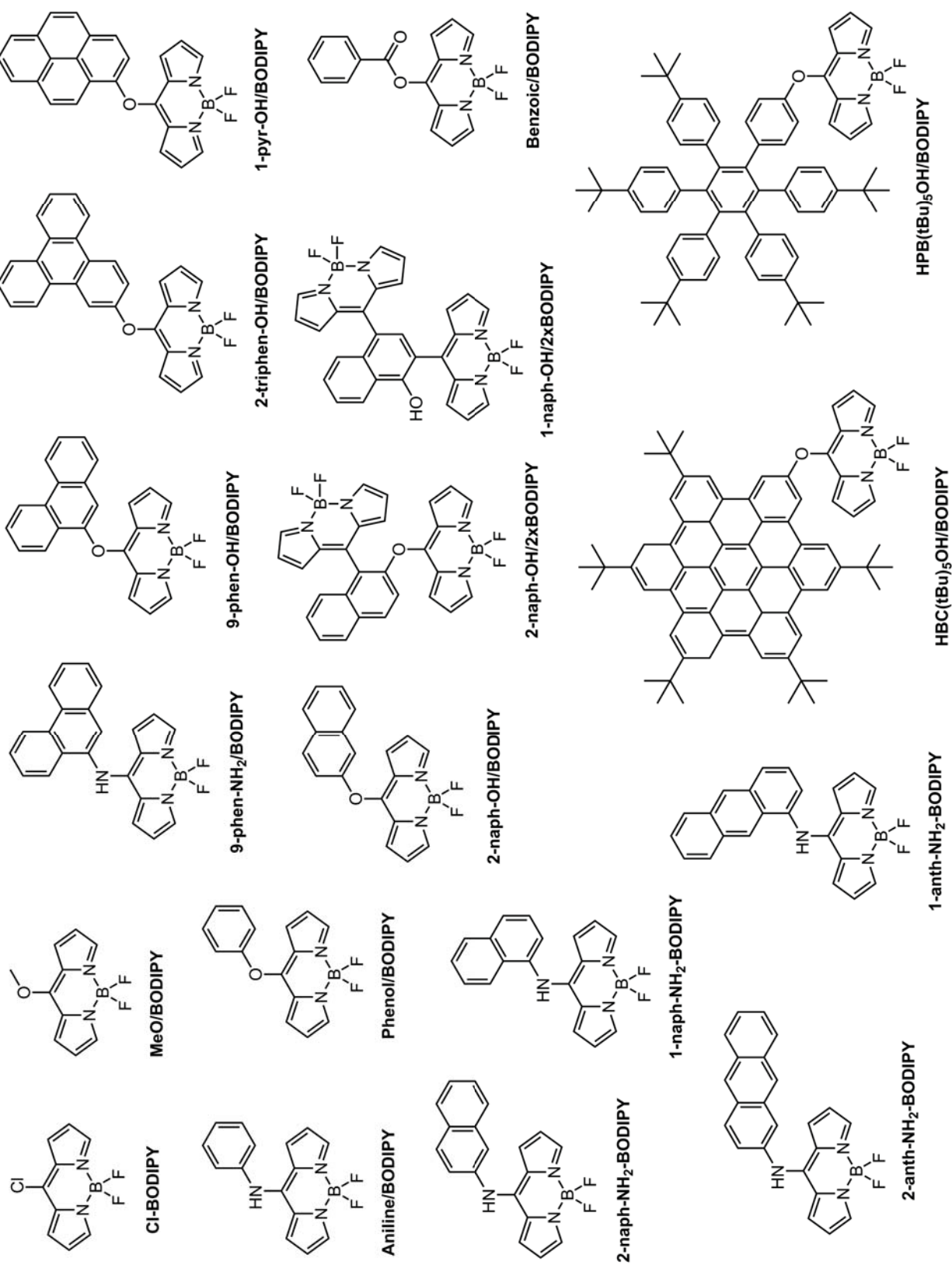
Figure A.33 - ¹³C NMR spectrum of benzoic acid/BODIPY in CDCl₃

Appendix B: Conversion of Raman spectra units

Computational output of predicted Raman spectra gives Raman activities in units of $\text{\AA}^4/\text{amu}$. However, experimental Raman spectra are determined in terms of differential cross sections. As such, these activities need to be converted into differential cross-sections prior to comparison with experimentally obtained spectra. Raman intensities are converted according to Equation B-1³⁷, where s_j is the Raman activity in $\text{\AA}^4/\text{amu}$, ν_0 is the incident laser frequency (in m^{-1}), ν_j is the Raman shift (in m^{-1}), and c, T, h, ε_0 , and k are constants.

$$\frac{d\sigma_j}{d\Omega} = \left(\frac{\pi^2}{45\varepsilon_0^4} \right) \left[\frac{(\nu_0 - \nu_j)^4}{1 - \exp\left[-\frac{hc\nu_j}{kT}\right]} \right] \left(\frac{h}{8\pi^2 c \nu_j} \right) s_j \quad (\text{B-1})$$

This conversion gives differential cross-sections in units of $\text{m}^2 \text{sr}^{-1}$, which is generally then converted to units of $\times 10^{-15} \text{\AA}^2 \text{sr}^{-1}$, or normalised, for comparison with experimental data.



FOLD-OUT REFERENCE SHEET